Forschungsbericht 2024-21

Whirl Flutter Stability Analysis Using Propeller Transfer Matrices

Christopher Koch

Deutsches Zentrum für Luft- und Raumfahrt
Institut für Aeroelastik
Göttingen

DLR Deutsches Zentrum für Luft- und Raumfahrt

Forschungsbericht 2024-21

Whirl Flutter Stability Analysis Using Propeller Transfer Matrices

Christopher Koch

Deutsches Zentrum für Luft- und Raumfahrt
Institut für Aeroelastik
Göttingen

176 Seiten
53 Bilder
5 Tabellen
107 Literaturstellen

DLR Deutsches Zentrum für Luft- und Raumfahrt

Herausgeber:

Deutsches Zentrum
für Luft- und Raumfahrt e. V.
Wissenschaftliche Information
Linder Höhe
D-51147 Köln

ISSN 1434-8454
ISRN DLR-FB-2024-21
Erscheinungsjahr 2024
DOI: 10.57676/bf00-1962

Zugl.: Berlin, Technische Universität, Diss., 2024

Aeroelastik, Whirl-Flattern, Propeller, Frequenzbereich, Simulation
(Veröffentlicht in englischer Sprache)

Christopher Koch
DLR, Institut für Aeroelastik, Göttingen

Whirl-Flatteranalyse mittels Propeller-Transfermatrizen
Dissertation, Technische Universität Berlin

Whirl-Flattern ist eine aeroelastische Instabilität, dessen genaue numerische Vorhersage wichtig für das Design von Propellerflugzeugen ist. Allerdings berücksichtigen bisherige Methoden zur Flatteranalyse im Frequenzbereich die notwendigen Transferfunktionen für den Propeller nur sehr vereinfacht. Diese Arbeit schlägt eine neue Methode basierend auf aus einem Simulationsmodell identifizierten Transfer-Matrizen zwischen Nabenverschiebung und Nabenlasten des Propellers vor.

Hierzu werden mit einem Zeitbereichs-Simulationsmodell durch aufgeprägte Störbewegungen die Antworten auf Verschiebungen an der Propellernabe berechnet und diese anschließend zusammen mit der Anregung in den Frequenzbereich transformiert. Die daraus ableitbaren Transferfunktionen für den isolierten Propeller können anschließend in einer Flatteranalyse im Frequenzbereich zur Repräsentation des Propellers genutzt werden und enthalten alle Simulationsbausteine (z.B. Blattelastizität, Rotor-Aerodynamik) des Zeitbereichsmodells.

Die Methode wird in der Arbeit mittels gekoppelten Zeitbereichssimulationen verifiziert sowie der Einfluss von Blattelastizität und genauerer Rotoraerodynamik auf die Whirlflatter-Stabilität zweier aeroelastischer Systeme untersucht. Blattelastizität erweist sich als stark stabilisierend sowohl auf das vereinfachte Triebwerks-Pylon-Modell als auch für eine generische Propellerflugzeug-Konfiguration. Eine genauere Abbildung der Aerodynamik am Propeller bis hin zu 3D-Potentialverfahren ist ebenfalls stabilisierend, allerdings in geringerem Maße

Aeroelasticity, Whirl flutter, propeller, frequency domain, simulation

Christopher Koch
German Aerospace Center (DLR), Institute of Aeroelasticity, Göttingen

Whirl Flutter Stability Analysis Using Propeller Transfer Matrices

Doctoral Thesis, Technical University of Berlin

Whirl flutter is an aeroelastic instability that requires accurate prediction during propeller aircraft design. However, current flutter analysis methods in the frequency domain only include simplified propeller transfer functions. This work proposes a new method to represent the propeller using identified transfer matrices between hub displacements and loads.

To obtain the transfer matrices, a time-domain simulation model of the isolated propeller is subjected to forced-motion perturbations at the hub, and the time response of the propeller hub loads is measured. After transforming both into the frequency domain, the resulting linear transfer functions for the isolated propeller can be used in a frequency-domain flutter analysis. The transfer matrices include all simulation features of the time-domain model, such as blade elasticity and unsteady propeller aerodynamics.

The new method is verified using coupled time-domain simulations. The influence of blade elasticity and more accurate aerodynamic modeling on the flutter stability of two aeroelastic systems is explored. Blade elasticity is shown to have a strongly stabilizing effect on the whirl flutter stability of the simplified pylon model and a generic propeller aircraft. More sophisticated aerodynamic modeling, including 3D potential theory, also stabilizes the system, though minorly.

Whirl Flutter Stability Analysis Using Propeller Transfer Matrices

vorgelegt von

Christopher Koch, M. Sc.

ORCID: 0000-0001-8014-3041

an der Fakultät V – Verkehrs- und Maschinensysteme
der Technischen Universität Berlin
zur Erlangung des akademischen Grades

Doktor der Ingenieurwissenschaften
- Dr.-Ing. -

genehmigte Dissertation

Promotionsausschuss:

Vorsitzender:	Prof. Dr.-Ing. Andreas Bardenhagen
Gutachter:	Prof. Dr.-Ing. Dieter Peitsch
Gutachter:	Prof. Dr.-Ing. Holger Hennings
Gutachter:	Prof. Dr.-Ing. Lorenz Tichy

Tag der wissenschaftlichen Aussprache: 08. Oktober 2024

Berlin 2025

Abstract

Whirl flutter, as an aeroelastic instability, can inflict significant requirements on the design of a propeller aircraft, especially for the engine suspension. Certification specifications require predicting whirl flutter, e.g., by including the propeller's relevant gyroscopic and aerodynamic forces in frequency-domain flutter analysis. However, descriptions for the isolated propeller compatible with frequency-domain analyses are limited in their modeling capabilities concerning, e.g., blade elasticity and more sophisticated propeller aerodynamics. On the one hand, current methods are primarily based on the method developed by Houbolt and Reed in the 1960s and only include a linearized, quasi-steady strip theory for the rigid propeller blades. On the other hand, modern multi-body simulation and rotorcraft comprehensive codes offer significant improvements regarding propeller modeling. Still, they are mostly restricted to the time domain and incompatible with frequency-domain flutter analysis.

This thesis aims to provide and verify a new method to include these modeling capabilities of modern time-domain propeller simulations in frequency-domain flutter processes. It uses the new method to explore the influence of blade elasticity and propeller aerodynamics on the transfer functions and whirl flutter stability of an example turboprop propeller-airframe system.

The thesis develops and verifies the Transfer-Matrix method (short: TM-method). The method revolves around frequency-domain transfer matrices from propeller hub motion to hub loads. The transfer matrices are identified using time-domain simulations of an isolated propeller model. Finally, they are included in the frequency-domain flutter equations and, therefore, in classical flutter analysis.
The TM-method can accurately predict whirl flutter for rigid and elastic propellers: it recovers the reference results obtained by coupled time-domain simulations. Blade elasticity stabilizes whirl flutter, eliminating the instability in the airspeed range and configurations studied. A comparison of transfer matrices between rigid and flexible propellers reveals that the reason lies in the reduction of the destabilizing coupling moment between pitch and yaw motion. Blade stiffness and eigenfrequency are the driving factors for this stabilization. Including more sophisticated propeller aerodynamics using unsteady blade aerodynamics and azimuthally varying induced velocities improves the correlation of unsteady aerodynamic predictions with mid-fidelity results. Improved modeling reduces the unsteady aerodynamic loads and increases whirl flutter speed by up to 6% compared to the classical analysis for the full aircraft model.

Kurzfassung

Whirl-Flattern ist eine aeroelastische Instabilität, dessen Unterbindung signifikante Anforderungen während des Entwurfsprozesses von Propeller-Flugzeugen erzeugen kann. Insbesondere die Lagerung der Propellertriebwerke ist hiervon betroffen. Laut Zertifizierungsvorschriften müssen deshalb alle relevanten Lasten des Propellers, insbesondere gyroskopische und aerodynamische Lasten, mit in die Flatterbewertung im Frequenzbereich mit einbezogen werden. Allerdings sind bestehende Propeller-Modelle für solche Analysen limitiert in ihrer Fähigkeit, Aspekte wie Blattelastizität oder fortgeschrittene Aerodynamik-Modelle zu berücksichtigen. Aktuelle Propellermodelle für die Flatteranalyse im Frequenzbereich basieren häufig auf der Methode nach Houbolt und Reed und umfassen nur eine linearisierte, quasi-stationäre Streifentheorie für starre Propellerblätter. Zwar gibt es moderne Simulationsverfahren wie die Mehrkörper-Simulation, die auch komplexere Propellermodelle ermöglichen. Diese liegen allerdings im Zeitbereich vor und sind damit nicht direkt kompatibel mit Flatteranalysen im Frequenzbereich.

Diese Arbeit zielt darauf ab, diese methodische Lücke zu schließen und eine neue Methode zu Einbindung moderner Propeller-Modelle in Flatteranalysen im Frequenzbereich zu entwickeln und zu verifizieren. Die Methode wird im Anschluss genutzt, um den Einfluss von Blattaerodynamik und -elastizität auf das Übertragungsverhalten eines Beispielpropellers sowie die Whirl-Flatterstabilität eines Gesamtflugzeuges zu untersuchen.

Die Transfermatrix-Methode (kurz: TM-Methode) als Kernergebnis dieser Arbeit basiert auf instationären Frequenzbereichs-Transfermatrizen, welche das Übertragungsverhalten zwischen Bewegungen und Lasten an der Propellernabe beschreiben. Die Transfermatrizen werden für ein isoliertes Propellermodell mittels Zeitbereichs-Simulationen identifiziert und in die Frequenzbereichs-Flattergleichungen eingesetzt. Damit können alle relevanten Modellierungsaspekte des Zeitbereichs-Modells in die Flatteranalyse einbezogen werden. Die TM-Methode kann die Whirl-Flatterstabilität für starre und elastische Propeller korrekt vorhersagen: sie reproduziert Referenzergebnisse aus gekoppelten Zeitbereichsrechnungen. Blattelastizität ist dabei ein stark stabilisierender Faktor, dessen Berücksichtigung Whirl-Flattern für die betrachteten Konfigurationen komplett eliminiert. Ein Einblick in die Transfermatrizen zeigt, dass der Grund für diese Stabilisierung in der Verringerung des Kopplungsmomentes zwischen Nick- und Gierbewegung des Propellers liegt. Die wichtigsten Einflussfaktoren sind dabei die Blattsteifigkeit und -eigenfrequenz.

Es wird zudem gezeigt, das detailliertere aerodynamische Modelle für den Propeller die Vorhersagegenauigkeit für das Übertragungsverhalten des Propellers verglichen mit einem Mid-Fidelity-Verfahren verbessern. Eine Berücksichtigung von instationärer Blattaerodynamik sowie über den Azimuth variierender induzierter Geschwindigkeiten reduziert dabei die vorhergesagten Lasten und erhöht die vorhergesagte Flattergeschwindigkeit der Gesamtflugzeug-Konfiguration verglichen mit der Referenzmethode um bis zu sechs Prozent.

Acknowledgments

I want to thank several people who helped me while compiling this thesis. They helped me along the way with direct input, discussions, or friendly words. Although I can not mention all of them, I want to thank some explicitly for their contribution.

First, I want to thank my committee for supervising this thesis. Thanks to the head of my committee, Prof. Dr.-Ing. Dieter Peitsch from TU Berlin, who accepted the supervision of this thesis when it was already in an advanced state. Prof. Dr.-Ing. Lorenz Tichy, head of the DLR Institute of Aeroelasticity, gave valuable scientific guidance and supervision. And I want to thank Prof. Dr.-Ing. Holger Hennings for the position in the department of aeroelastic simulation that allowed me to conduct my research, for his strategic guidance and the right contacts at the right time.

From the many colleagues at DLR-AE in Göttingen, I cannot name all those who helped along the way, but I still want to mention a few who strongly impacted my work. Thanks to Jürgen and Jan (alongside Oliver and Stefan) for supervising my master thesis, which brought me to Göttingen and sparked the interest in propeller whirl flutter. Special thanks to Jürgen for his continuous support as my team leader in DLR and the valuable insights and contacts from the helicopter and fixed-wing community. Thanks to Oliver for providing Floquet-methods, discussions about STARS, bikes, and all the topics you can think of. Big thanks to the colleagues from DLR-AE for the scientific discussions in offices, the TSO room, during presentations, and sometimes even on the bike. I am convinced that this thesis was only possible in its current form due to the broad scientific knowledge present at DLR-AE in Göttingen. Thanks to the partners from industry, who showed interest in my work and provided additional motivation to pursue this topic.

I want to thank all my co-authors of the publications that preceded this publication for their direct contribution to my work. And a special thanks to the students I supervised over the years (Alexander, Benedikt, Jan Hendrik, Valentin, Luisa, Julia) for their work in the form of code, models, methods, and results that directly or indirectly influenced this thesis.
From my study period in Aachen, I want to thank the Flugwissenschaftliche Vereinigung Aachen (FVA) for motivating the initial master thesis and the opportunity and motivation for hours on hours of work on CS22 load analysis before that. Special thanks to Wilhelm, who pulled me out of spacecraft design and into aircraft flight physics. Who knows where I would have gone otherwise?

Last but not least, I want to thank my friends and family, who provided me with a supportive and positive environment during my work. Thanks to Hendrik, Dominic, and Martin for the companionship in triathlon and life, to the (large) cycling group at DLR in Göttingen for countless hours spent together on the bike, to Sebastian for the initial pull towards endurance sports, and to Julian for deepening the addiction to cycling.
Thanks to Desa for filling my life with love and joy when I least expected it (Mau!). And, of course, I want to finish with saying thank you to my family, who set me on the path towards this thesis without knowing it, gave me the right mindset to conduct such work and all the support I could ever wish for on my journey.

Thanks to all of you, this would have not been possible without you!

Christopher Koch, Göttingen, June 2024

Contents

List of Figures

List of Tables

Nomenclature

Latin Symbols

Ar	aspect ratio
C	non-dimensional coefficient
E	Young's modulus
F	force
I	second moment of area
J	rotational inertia
K	stiffness
L	lift force
M	moment
N	general number
Ma	Mach number
R	propeller Radius
T	system period
V	airspeed
a	distance between propeller hub and pivot point
c	chord length
f	frequency
g	structural damping
i	imaginary unit
k	reduced frequency
m	mass
p	non-dimensional complex eigenvalue
r	radius variable
s	Laplace variable
t	time
x	displacement in forward direction
y	displacement in lateral direction
z	displacement in vertical direction

Greek Symbols

α	angle of attack
γ	Theordorsen function
ζ	critical damping
η	non-dimensional radius
θ	propeller disc pitch angle (rotation about y-axis)
λ	complex eigenvalue
μ	propeller advance ratio
π	mathematical constant
ρ	air density
σ	damping (real part of the complex eigenvalue)
ϕ	propeller disc rotation angle (rotation about x-axis)
ψ	propeller disc yaw angle (rotation about z-axis)
ω	(natural) angular frequency (imaginary part of the complex eigenvalue)
Γ	Wagner function
Ψ	blade azimuth angle
Ω	rotational speed (in rad/s)

Vectors

$\boldsymbol{a}$	state vector with force element states
$\boldsymbol{f}$	nonlinear function
$\boldsymbol{p}$	state vector with position states
$\boldsymbol{q}$	Vector collecting generalized degree of freedom
$\boldsymbol{u}$	Vector collecting physical degree of freedom
$\boldsymbol{v}$	state vector with velocity states
$\boldsymbol{w}$	vector with external inputs for MBS system
$\boldsymbol{x}$	state vector collecting all states
$\boldsymbol{F}$	Force vector

Matrices

$\underline{A}$	System matrix
$\underline{D}$	Damping matrix
$\underline{G}$	Gyroscopic matrix
$\underline{H}$	Transfer matrix
$\underline{K}$	Stiffness matrix
$\underline{M}$	Mass matrix
$\underline{Q}$	motion-induced aerodynamic force matrix
$\underline{\Phi}$	Modal matrix

Subscripts and Indices

aero	Aerodynamic
D	Dive (speed)
eff	effective
gen	In generalized coordinates
hub	With respect to propeller hub degree of freedom
kin	kinematic
l	lift
m	moment in y-direction in the Houbolt/Reed method
n	moment in z-direction in the Houbolt/Reed method
p	polar
prop	propeller
q	with respect to propeller disc pitch velocity in the Houbolt/Reed method
r	with respect to propeller disc yaw velocity in the Houbolt/Reed method
ref	Reference
system	for the aeroelastic system
TAS	True airspeed
x	with respect to displacement in forward direction
y	with respect to displacement in lateral direction
z	with respect to displacement in vertical direction
ϕ	with respect to propeller disc rotation angle (rotation about x-axis)
θ	with respect to propeller disc pitch angle (rotation about y-axis)
ψ	with respect to propeller disc yaw angle (rotation about z-axis)

Superscripts

T	transpose operator

Symbols

$\mathrm{Re}\,(\,)$	real part of complex number
$\mathrm{Im}\,(\,)$	imaginary part of complex number
$\mathcal{F}\,(\,)$	Fast Fourier Transformation (FFT)
$\lvert\,\rvert$	absolute value
Δ	difference value
$\dot{(\,)}$	temporal derivative $\frac{d}{dt}$
$\ddot{(\,)}$	second temporal derivative $\frac{d}{dt^2}$
$\tilde{(\,)}$	dimensional

Abbreviations

1D	One dimension(al)
2D	Two dimension(al)
3D	Three dimension(al)
AMT	Averaged moment theory
BEM	Blade element momentum theory
CFD	Computational fluid dynamics
DLM	Doublet lattice method
DLR	Deutsches Zentrum für Luft- und Raumfahrt
DOF	Degree of freedom
FEM	Finite element method
GAF	Generalized aerodynamic force
LCO	Limit cycle oscillation
LHS	Left-hand side
MBS	Multi-body simulation
NASA	National Aeronautics and Space Administration
RHS	Right-hand side
RMA	Rational matrix approximation
ROM	Reduced-order model
TM	Transfer-matrix (method)
UPM	Unsteady panel method
UVLM	Unsteady vortex lattice method
VVPM	Viscous vortex particle method

1

Introduction

1.1. Motivation

Recently, propeller engines have gotten more attention from aircraft designers due to their superior propulsive efficiency over turbojet and turbofan engines at low and medium flight speeds. Especially emerging (hybrid-) electric propulsion concepts, in which the propellers are powered by electric motors instead of conventional turboprop engines, offer new configurational opportunities to aircraft designers, e.g., concerning engine number and placement.
Aeroelastic stability, especially of the engine support, can become a significant concern in the design of such aircraft. The following example shows that designing a propeller engine suspension system is a careful trade-off between load-bearing capacity, passenger comfort requirements, and aeroelastic stability.

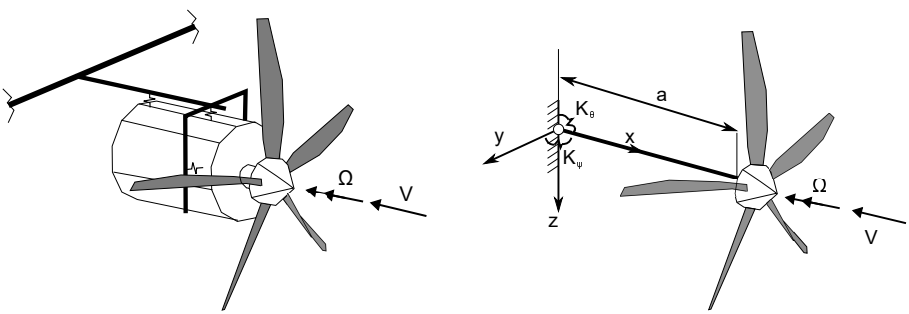

(a) Engine suspension schema **(b)** Simplified dynamic model

Figure 1.1.: Schema of a turboprop engine suspension (a), including a simplified dynamic model (b) used demonstration purposes in this thesis.

Fig. 1.1(a) shows a simplified schematic of a typical turboprop engine suspension structure. The propeller is connected to the engine via the rotating shaft, which is usually supported within the first stage of the gearbox. For global airframe dynamics, the engine itself is considered a rigid body here due to the

high stiffness of the engine and gearbox housing. The engine is supported by a nacelle truss (thick black lines), which connects the engine to the main wing structure. Instead of a rigid connection, the elements connecting the engine and nacelle truss comprise elastomer springs (indicated by the small spring symbols connecting the engine and truss in Fig. 1.1(a)), also called shock mounts [1]. The purpose of these structural elements is to decouple the engine and its vibrations dynamically from the airframe, increasing the fatigue life and passenger comfort [2].
To demonstrate this and motivate the importance of aeroelastic stability considerations, the system shown in Fig. 1.1(a) is reduced to the simplified pylon system shown in Fig. 1.1(b). The simplified system only considers the pitch (θ) and yaw (ψ) motion degree of freedom (DOF) of the engine about a pivot point located in the distance a behind the propeller plane. The pivot point is a simplified representation of the elastic center regarding pitch and yaw of the more complex structure in Fig. 1.1(a). The engine pitch and yaw are considered to be restrained by springs (K_θ and K_ψ), which, together with the engine rotational inertia about the y- and z-axis, yield the system's uncoupled rigid body pitch and yaw modes.

The design goal of the shock mounts is explained in Fig. 1.2. Due to small remaining unbalances in the propeller and engine shafts, due to angle-of-attack or in-homogeneous inflow, the engine experiences harmonic inertial or aerodynamic loads with the frequency equivalent to once-per-revolution (1P) or higher-harmonics of the rotational speed (e.g., 2P, 5P, ...). Fig. 1.2 shows the transmission characteristics from the vertical force at the propeller hub to the generalized moment at the nacelle mounting. In other words, it shows the loads in y- and z-direction transmitted to the airframe over a range of excitation frequencies. For low excitation frequencies (left side of the plot), the transmission ratio is almost 1, meaning steady loads (such as weight) are directly transferred. If the excitation lies in the range of the engine pitch and yaw modes (around 10 Hz), the loads transferred to the airframe are dynamically amplified due to resonance. Above the range of the first engine modes, the transmission factor quickly falls to very small values (right side of the plot), resulting in dynamic isolation. In this frequency range, only small loads are transferred to the airframe. The objective of the engine suspension system is to achieve minimum transmission characteristics during the design. This is done by designing the stiffness of the shock mounts to obtain low rigid-body frequencies of the engine, ideally well below the rotational speed of the propeller, while still meeting strength and stiffness requirements [2].

Aeroelastic stability is a significant factor that creates minimum shock mount stiffness requirements. According to certification requirements [3], large passenger aircraft have to be free of flutter in all nominal configurations up to a speed

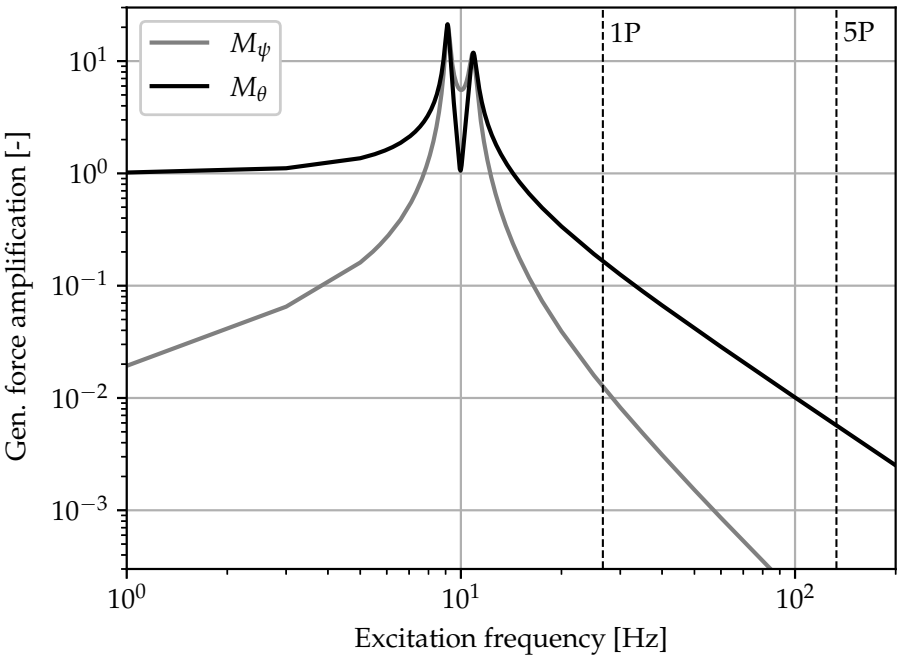

Figure 1.2.: Force transmission characteristics of the simplified pylon model from harmonic hub loading to moment at the pivot point

of 1.15 times the dive speed V_D, and free of flutter in case of failure, e.g., of a shock mount, up to V_D. For a propeller aircraft, whirl flutter is an aeroelastic instability that needs to be kept outside of this envelope [4].

Whirl flutter is a dynamic aeroelastic instability of the whirl modes emerging, e.g., from pylon pitch and yaw modes. If the engine and propeller are rotating, gyroscopic moments couple the pitch and yaw mode into a forward and backward whirl mode. During a cycle of such a mode the propeller hub shows an elliptical path [5] (compare Fig. 1.3). The mode with the higher frequency becomes the forward whirl mode, in which the direction of the whirl is the same as the rotation of the propeller (see Fig. 1.3(a)). The lower frequency mode becomes the backward whirl mode, which shows a reverse whirling direction (depicted in Fig. 1.3(b)). At high airspeeds and due to unsteady aerodynamic loads, the backward whirl mode can become unstable, resulting in a divergent whirling motion and flutter [5].

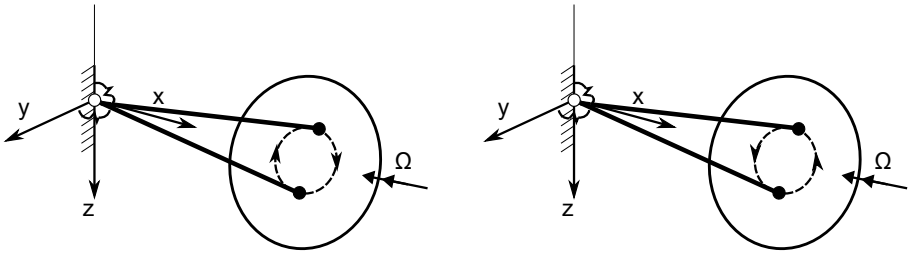

(a) Forward whirl mode **(b)** Backward whirl mode

Figure 1.3.: Whirl modes of the simplified pylon system, emerging due to gyroscopic couplings.

Driving factors influencing the aeroelastic stability of the propeller-engine system are the frequencies of the engine pitch and yaw mode and, therefore, the shock mount stiffness. Fig. 1.4 shows the aeroelastic stability of the simplified pylon system for varying combinations of pitch and yaw springs. Instead of the pitch and yaw stiffness, K_θ and K_ψ, the respective rigid body eigenfrequencies, ω_θ and ω_ψ, are used for the axes. They are computed from the stiffness and inertia of the model as shown in Eq. 1.1, assuming no coupling between the direction (i.e., no gyroscopics and aerodynamics). The top right of the whirl flutter stability map in Fig. 1.4 is the stable area, so a stiff engine suspension yields a stable system. The bell curve in the middle represents the border to the parameter range that shows dynamic whirl flutter. Configurations with equal pitch and yaw stiffness are, therefore, most critical concerning whirl flutter, as are low-frequency values. If only one direction is stiff and the other has very low stiffness, there is the possibility of static divergence [5]. The more sensitive the system becomes to whirl flutter, the larger the extension of the unstable area is, putting more substantial requirements on the minimum shock mount stiffnesses.

$$\omega_\theta = \sqrt{\frac{K_\theta}{J_\theta}} \; ; \; \omega_\psi = \sqrt{\frac{K_\psi}{J_\psi}} \tag{1.1}$$

As seen from Fig. 1.2, shock mount stiffness should be as small as possible from the viewpoint of vibration isolation. Fig. 1.4, on the other hand, demonstrates that aeroelastic stability creates a lower bound for the engine support stiffness. These conflicting requirements must be balanced during the design process of propeller engine suspensions. The ideal goal is a suspension system that keeps the system stable in the aeroelastic envelope while providing minimum vibration

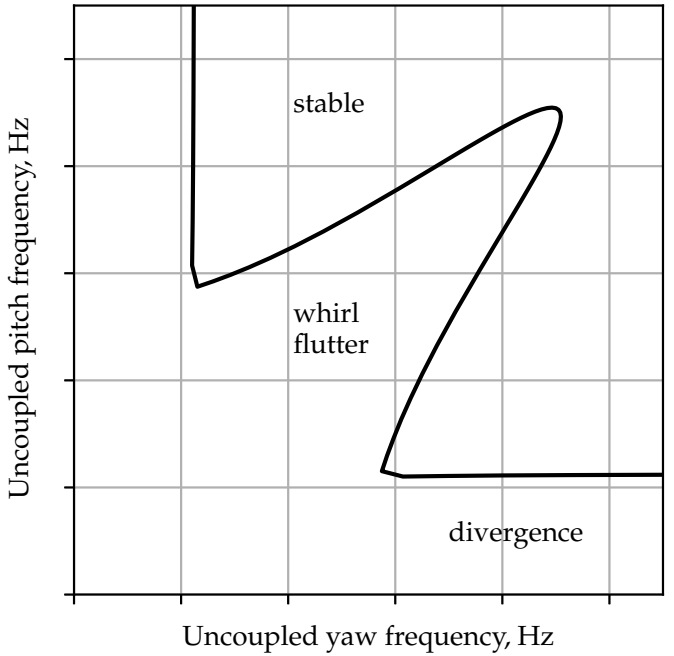

Figure 1.4.: Example whirl flutter stability map

transmission to the airframe. This requires accurate prediction of propeller whirl flutter already during the design process using computational models. The certification specifications for large aircraft [3] contain these requirements for including the propeller and engine suspension system into the aeroelastic stability assessment in the acceptable means of compliance [3, AMC 25.629, 5.1.4.6 (a)]:

> The evaluation of the aeroelastic stability should include investigations of any significant elastic, inertial, and aerodynamic forces, including those associated with rotations and displacements in the plane of any turbofan or propeller, including propeller or fan blade aerodynamics, powerplant flexibilities, powerplant mounting characteristics, and gyroscopic coupling.

The following section gives an overview of the state of the art regarding propeller whirl flutter prediction, from its early stages in the 1960s to modern simulation capabilities.

1.2. State of the Art

Early work

The first mention of the potential instability of propeller engines was in 1937 by Taylor and Browne [6], who studied the vibration isolation of aircraft engines. They noticed that in their theoretical model, "the low-frequency reverse-rotation precession tends to become unstable" [6], but concluded that this was unrealistic for practical applications. The phenomenon was only rediscovered 20 years after causing two accidents with a commercial turboprop airliner; the Lockheed Electra [7]. After initial problems in finding the root cause of those accidents, attention quickly turned to the precession instability of the large turboprop engines. Several investigations were launched [7] to understand the underlying mechanism. The paper by John C. **Houbolt and** Wilmer H. **Reed** III [8] can be considered a big step forward in the prediction of whirl flutter. They provided a comprehensive method for calculating the motion-induced in-plane loads that drive the mechanism of whirl flutter based on a simple strip theory approach. They demonstrated the application of the method for predicting the whirl flutter stability of a simplified propeller and pylon system. The characteristics of propellers to create in-plane forces under angle-of-attack (or yaw angle, respectively) were known before from aircraft flight mechanics, but Houbolt and Reed's method proved simpler than, e.g., Ribner's formulas [9].

To validate the new theoretical findings, wind tunnel **experiments** were conducted. Bland and Bennett [10] studied an isolated propeller in the NASA Langley transonic dynamics tunnel for its static in-plane load derivatives, which they compared to those predicted with Ribner's and Houbolt and Reed's calculation methods over a range of operating conditions. They found similar qualitative trends in all derivatives compared to the experiment but observed quantitative offsets. They also measured the flutter boundaries for a simplified pylon system, comparing them with the predicted boundaries from both computational methods and the predictions made with measured derivatives. While the latter proved accurate, the computations showed a trend of predicting lower (and, therefore, conservative) flutter speeds. In a later study, Bennett and Bland [11] extended this to include a simplified wing model, demonstrating the (in most cases) stabilizing effect of wing bending and torsion due to aerodynamic damping. Wing torsion was reported to have a potentially destabilizing influence by replacing the engine pitch degree of freedom in the whirling motion [4]. In his review paper from 1966, Reed [4] summarizes the findings of many of the early studies.

Applications of the Houbolt/Reed method

One significant effect of these early investigations after the accidents was the addition of requirements regarding whirl flutter prediction into the certification specifications for large propeller aircraft [3]. Due to its simplicity, Houbolt and Reed's method was often used for the design and **analysis of turboprop aircraft structures**. Hyrcko [2] describes the common design problem for turboprop manufacturers: Balancing whirl flutter stability with the vibration isolation characteristics of the engine support. Aircraft designers used more and more complex structural airframe models to study the whirl flutter characteristics of their design (see, for example., Nitzsche [12]), finding more and more complex flutter couplings. Because the back-up structure (e.g., the wing or the tail for rear-mounted engines) can act as a dynamic damper, it was found that these more complex structural models are better suited both for the prediction of the transmission characteristics and aeroelastic stability [13].

Presented at the 1989 MSC World User's Conference, the work of W.P. Rodden and T.L. Rose [14] marks another milestone in predicting propeller whirl flutter. By demonstrating the use of aerodynamic derivatives from the Houbolt/Reed method in conjunction with complex, finite element (FE) based aeroelastic models (in this case in MSC Nastran), they opened the path towards **full integration of whirl flutter prediction into the frequency-domain flutter prediction** process of commercial aircraft. Since then, a small program has been shipped with MSC Nastran, allowing the computation of the required stiffness and damping matrices from the Houbolt/Reed method. Jiří Čečrdle demonstrated this integration into flutter analysis with MSC Nastran in several publications. He developed a procedure using structural optimization [15] to find the critical (minimal) engine support stiffness required for aeroelastic stability at certification speed. Knowledge about this limit allows designers to ensure this minimum stiffness even under fatigue or failure conditions. These studies were extended to a half-span turboprop model [16], also including unsteady wing and nacelle aerodynamics and different mass cases. The study demonstrated the influence of the selected mass case (and connected changes in the flutter mechanism) on the minimum stiffness requirements. Čečrdle demonstrated that also the parameters going into the Houbolt/Reed method, e.g., the blade lift curve slope distribution, can have a significant impact on whirl flutter stability predictions [17]. Finally, he described the details of applying the Houbolt/Reed method for demonstrating compliance with the certification requirements, elaborating on the importance of treating failure cases like propeller overspeed or feathered conditions [18]. The results of his papers, together with an extended literature review, are summarized in his book on turboprop aircraft whirl flutter [5].

Due to its analytical nature, the method of Houbolt and Reed is fast and robust in its application, making it well-suited for **parameter studies**. The author of this thesis used it for comparing different modeling approaches for the airframe structure [19], ranging from only including engine suspension DOF to including pylon and wing structural DOF and, finally, wing aerodynamics. Stability prediction can vary widely over these different modeling approaches, highlighting the importance of integrating whirl flutter prediction into full-aircraft analysis instead of just treating the isolated engine suspension. While this study varied structural parameters while keeping the geometry the same, Böhnisch et al. [20] investigated the influence of the spanwise position of a propeller on the aeroelastic stability of a slender wing, eventually also comparing pusher and tractor configurations [21]. They also elaborate on effects outside of whirl flutter stability, such as the impact of engine mass and gyroscopics on classical wing flutter.

Structural nonlinearities

While the work described above mainly focuses on linear aeroelastic stability, recent work has also investigated the stability behavior of whirl flutter systems with structural nonlinearities. Mair et al. [22] used the linear aerodynamic derivatives of the Houbolt/Reed method coupled with a simplified pylon system with nonlinear pitch and yaw stiffness. They used continuation and bifurcation analysis with nonlinear time integration to find the system's limit-cycle oscillations (LCOs). For some of the investigated nonlinear stiffness characteristics, they found configurations in which the nonlinear system exhibited unstable behavior before the linear flutter point, highlighting the importance of considering potential structural nonlinearities. Quintana et al. [23] studied the influence of free play in the engine support on the stability characteristics of the simplified pylon system. Especially in combination with nonlinear stiffness characteristics, very complex dynamic behavior was observed in the system studied. This type of analysis usually relies on several nonlinear time simulations, which can be computationally expensive but allow for incorporating more effects into analysis models. Gali et al. [24] presented a bifurcation prediction approach that uses only two nonlinear time simulations in the stable regime to predict the flutter onset speed, making nonlinear simulation in reasonable computational time feasible for practical applications.

Unsteady aerodynamics

While fast and robust, the method by Houbolt and Reed makes a few simplifications concerning propeller modeling. Next to the rigid blade assumption, which is treated in a later paragraph, these assumptions mainly concern the unsteady aerodynamics of the propeller.

Because they also affect aircraft aerodynamics and handling qualities, the in-plane loads due to non-axial inflow on the propeller, also called **1P hub loads**, have been more widely studied with different methods in the literature. The steady 1P hub loads are equivalent to the stiffness derivatives in dynamic whirl flutter analysis, so there is some overlap in the aerodynamics used to predict them. Several authors have worked on improving the prediction from Ribner's early work [9]. Recent work includes the thesis of Smith [25], who focused on low-fidelity methods such as blade element momentum theory (BEM). He described a formulation (the weighted momentum theory) better suited for predicting 1P hub forces. Other authors used higher fidelity methods such as panel codes or computational fluid dynamics (CFD). Fei et al. [26] developed an unsteady vortex lattice (UVLM) code to study the loads on propellers under high angles of attack, as they might appear in vertical take-off and landing vehicles. They connected the reasons for the occurring side forces with effects due to the tilted wake. The UVLM predicted these in-plane forces well compared to the CFD reference up to the onset of stall. Transonic speeds also need to be considered for practical application to commercial propeller aircraft. In France, extensive validation campaigns with the APIAN experiments and CFD computations in both isolated [27, 28] and installed [28] conditions have been carried out. These studies state the potentially significant contribution of the spinner to in-plane forces [27] and compare different numerical modeling approaches such as unsteady time simulation and steady actuator disc predictions [28]. Ruiz and Calavera [29] also included blade elasticity in their analysis. They found an offset concerning wind tunnel data in both installed and isolated conditions. They suggest a correction of CFD predictions using data from wind tunnel experiments.

While some literature for steady 1P hub loads can be found, publications on the influence of more complex aerodynamic modeling on **unsteady aerodynamics for whirl flutter applications** are rare. Gennaretti and Greco [30] compared different aerodynamic modeling approaches, including prescribed and free wake boundary element methods, for the stability prediction of a rotor-pylon system. They derived unsteady, finite-state blade transfer functions from their solvers, capturing the frequency-dependent aerodynamics along the blades. In their publication, they highlight the presence of multiple frequencies due to the returning wake and the varying reduced frequency along the blade span, leading to a dependency of the unsteady blade transfer functions on aspect ratio. Comparing the stability boundaries at different forward flight speeds for a two-bladed and three-bladed propeller, they conclude that simplified aerodynamics (such as in the Houbolt/Reed method) are not necessarily conservative. Wang and Chen [31], on the other hand, improved the prediction of aerodynamic derivatives used in the Houbolt/Reed method by identifying them directly from time-domain simulations with a UVLM solver. They use a slow, quasi-steady

harmonic excitation in propeller disc pitch to extract aerodynamic stiffness and damping, which can then be converted into aerodynamic derivatives. Although this method allows the usage of more complex aerodynamic solvers, it still neglects the frequency-dependency of unsteady aerodynamics.
Most of the work regarding whirl flutter described so far either studies isolated pylon-propeller systems or neglects **aerodynamic interaction between propeller and wing**. In their paper, Rodden and Rose [14] offer a first approach to include that interaction into frequency-domain flutter calculations using the Doublet Lattice Method (DLM). They scale the dynamic pressure of the wing panels in the slipstream based on the thrust-dependent steady induced velocity of the propeller. Tangential induction due to propeller torque is neglected. In the other direction, they introduce additional propeller pitch and yaw angle contributions from the velocity components induced at the propeller hub by the oscillating wing panels. Although describing the theory in their paper, they do not show an application. Čečrdle applies the approach [16] and quantifies the effect it has on the stability boundary concerning engine mount stiffness. For the twin-engine model studied, he shows a destabilizing effect of the corrections depending on the modes involved in the flutter mechanism. No concrete flutter mode shapes were given, making generalizing the results to other configurations or modes difficult. To the author's knowledge, at the time of writing, no other publication includes aerodynamic interaction in frequency-domain flutter evaluations.
For tiltrotor applications (see following paragraph), which involve large rotors closely mounted to the tip of the aircraft wing, the influence of aerodynamic interaction was studied using time-domain aerodynamics such as viscous vortex particle methods (VVPM) [32, 33]. Both applications found increased damping of the wing beam mode compared to aerodynamic models that model wing and rotor aerodynamics separately, increasing the flutter speed depending on the configuration studied. Corle et al. [32] attribute this effect to interactional aerodynamics or differences in the induced velocities on the wing when using VVPM.

Blade elasticity

The elasticity of turboprop propeller blades was often neglected in the work described above because blades were considered stiff. While this might apply to turboprop propellers, the aeroelastic stability characteristics of another aircraft category are much more affected by the dynamics of large, flexible rotor blades: **tiltrotor aircraft**. Tiltrotor aircraft usually feature two large, tilting rotors on their wing tips, allowing vertical take-off in helicopter mode and fast forward flight when tilted forwards in propeller configuration [34]. The rotors used in such aircraft differ from classical turboprop propellers in their complexity: rotors feature cyclic blade pitch control, the blades are longer and usually hinged

or gimballed for load reduction [34, 35]. This makes blade structural dynamics a more critical feature for aeroelastic stability. While this work focuses on propeller whirl flutter, a review of the most important literature in the field of tiltrotor whirl flutter is included, as it has essential overlaps with the work presented.

Even **early publications** studying tiltrotor (or sometimes called proprotor) whirl flutter include some model for the blade dynamics. Young and Lytwyn [35] used hinged, flapping blades coupled with a simple pylon model. They found a stabilizing influence of blade flapping on whirl flutter until flap stiffness falls below a particular value, from which the system becomes more unstable again. They made an important observation: For very flexible blades, the flutter mechanism becoming unstable changed from a classical backward whirl flutter to a forward whirling motion involving the cyclic blade modes and at least one pylon mode. Unlike backward whirl flutter, this new flutter mechanism only required one pylon direction to be flexible, as the cyclic blade flapping provided the other motion component for the whirling motion. Johnston [36] extended these studies to include the lead-lag motion of the proprotor blades. By varying the stiffness ratios, he confirmed the stabilizing influence of blade flapping and found a destabilizing tendency of lead-lag modes. His paper reports various instability mechanisms for lower blade stiffnesses (in both flap and lead-lag direction), highlighting the importance of including these DOFs in tiltrotor stability analyses. Kunz [37] later summarized the influence of different parameters of a simplified rotor-pylon system in his review paper. Johnson [34] advanced the state of the art at that time by deriving an analytical model including not only pylon DOF but also a model of the elastic wing coupled with an elastic blade formulation and quasi-steady aerodynamics for both wing and rotor aerodynamics. He compared the results of his computational model with wind tunnel experiments, finding a good correlation. He highlights the importance of frequency placement of the elastic blade modes relative to the airframe modes as a design feature influencing the dynamic characteristics of the whole system. In his conclusion, Johnson points out that the model includes the "fundamental features of the proprotor aeroelastic system" [34, p. 160], but could be extended to include more sophisticated rotor and airframe models.

In the following time, his outlook became a reality with the advent of so-called **rotorcraft comprehensive codes**. These simulation tools for rotorcraft aeromechanics feature a modular architecture to couple dynamic models for the blades, control systems, and airframe with aerodynamic models of different fidelity levels. They have become the backbone of modern rotorcraft analysis [38]. Several publications apply rotorcraft comprehensive codes to the prediction of whirl flutter stability. Yeo et al. [39] compared CAMRAD II and RCAS, two comprehensive codes, and conducted extensive parameter studies on a

generic tiltrotor model, highlighting the most critical design parameters (in their case, parameters influencing the regressive lead-lag frequency). Several publications compared two comprehensive codes against each other and used validation data, e.g., from the WRATS experiment [40]. These comparisons include validation of CAMRAD II and RCAS with WRATS data [41], of RCAS and Dymore [42] and of Dymore and MBDYN [43]. The studies find fair to good agreement with experimental frequency and damping values for a range of operating conditions. The whirl flutter phenomenon investigated is dominated by strong interaction between the rotor and wing dynamics, which occur in the same frequency range. Currently, new experiments for validation of the next generation of comprehensive analysis are in preparation, both in Europe [44, 45] and the United States [46, 47]. The application of rotorcraft comprehensive codes is not restricted to clamped wings as used in experiments. It can also be extended to full, free-flying aircraft like the Bell XV-15 research aircraft [48, 49], a precursor of the first mass-produced tilt-rotor, the V-22 Osprey [50].

An important common feature of all these analyses and simulation codes is their reliance on **time-domain analysis**. This distinguishes them from the common frequency-domain methods in fixed-wing whirl flutter predictions. Frequencies and dampings for tiltrotor models are either obtained by direct linearization of the equations of motions about a (nonlinear) trim point (e.g., in [39]) or using nonlinear time simulation. In the second case, the dominating frequencies and damping ratios are extracted from the time response of the system to a perturbation, e.g., using the log-decrement method [51] or the matrix-pencil-method [44]. This is less robust and computationally more expensive than frequency-domain analysis but allows the use of more complex and even nonlinear models. In his thesis, Cocco [48], for example, used a vortex particle code coupled with multi-body simulation (MBS) for his model of the Bell XV-15, capturing aerodynamic interaction between rotor and airframe. Corle [51] demonstrated using CFD for whirl flutter stability analysis, advancing the aerodynamic fidelity for tiltrotor whirl flutter predictions.

Some attempts have been made to use rotorcraft comprehensive codes for the analysis of **propeller aircraft**. Acree [52] presented a study for a large tilt-wing transport aircraft featuring unusually large propellers. He applied CAMRAD II to analyze the configuration and study blade and whirl flutter stability. For this configuration, blade flutter due to the unconventional propeller design (including cyclic pitch control) was a bigger problem than whirl flutter. A string of recent publications about the X-57 aircraft concept by NASA also applied Dymore and CAMRAD II models for the clamped wing with tip propeller [53] up to the analysis of the free-flying aircraft [54]. The authors demonstrated the influence of aerodynamic modeling (wing aerodynamics, propeller airfoils, quasi-steady and unsteady aerodynamics) and blade elasticity on whirl flutter using Prony

analysis on the perturbation response about a trim state [54]. They found a strong stabilizing effect of considering blade elasticity compared to the rigid blade analysis [55]. This was possible due to their use of multi-body dynamics, coupling the flexible rotating blades with the elastic wing in the time domain. Comparing predictions for the flutter speed of the X-57 with rigid and elastic blades showed a 50% increase in flutter speed with elastic blades [55, Fig. 8]. These results question the validity of the rigid blade assumption in the classical Houbolt/Reed method, as it could give very conservative results. An analysis of stiff tiltrotor models [56] even showed that moderate blade stiffness can completely stabilize whirl flutter [56, Fig. 3/6] while also pointing out that decreasing stiffness further produces other instabilities such as forward whirl flutter [56, Fig. 5]. Donham [57] attributed this stabilization to the dynamic response of the blade dynamics to the harmonic blade loading during the whirl motion. This dynamic response alters the transfer function from propeller disc pitch to in-plane loads in amplitude and phase and, therefore, whirl flutter stability.

Frequency domain methods

Summarizing the work described so far highlights two key points: On one side, as the first part of this section showed, integration of whirl flutter prediction into frequency-domain flutter analysis of propeller aircraft, e.g., using the Houbolt/Reed method, is a well-established. On the other side, as demonstrated by the vast literature in tiltrotor research, more complex rotor modeling in the time domain is available, e.g., through rotorcraft comprehensive codes. The increased modeling depth of these tools could benefit the fidelity of propeller whirl flutter analysis, but their use is impeded by the switch to time-domain analysis.

Some approaches are present in literature to **reduce the complex time-domain rotor models** into forms that are easier to couple. Wang and Chen's identification procedure [31] of unsteady propeller derivatives from time-domain aerodynamic models is one example, allowing to make use of more complex aerodynamic tools while still keeping the rigid blade assumption. Another approach that is particularly important for this work is coming from the field of helicopter dynamics. Although comprehensive codes cover most analysis tasks in this field [38], some require faster models. Bielawa [58, 59] presented a method for rapid coupling between a rotor and several different pylon structures for broad parameter studies. His approach uses analytically derived or measured rotor hub impedance functions (transfer function from hub displacement to hub loads in the frequency domain). While analytically deriving these transfer functions becomes very difficult for complex rotor models, he highlights the application in experimental testing. He suggests that with his method, only the

stable rotor has to be tested and can then be analytically coupled with various pylon models, avoiding expensive and dangerous stability testing of coupled models.
Another area requiring fast models is rotorcraft flight dynamics and control design [60]. To be usable in real-time applications, models must be accurate but fast, promoting Reduced-order models (ROM) usage. Gori et al. [60] presented an analysis procedure to reduce a complex, aeroelastic time-domain rotor model into a finite-state state-space model for perturbational analysis. They show a three-step procedure involving the calculation of the harmonic perturbation response of the rotor about its hub DOF, transferring these into the frequency domain, and finally, a rational matrix approximation to obtain the final time-domain ROM for the rotor, which can then be coupled with a state-space airframe model for analysis. They applied it to recover time response signals of the coupled system and claim its usefulness for real-time applications. While Gennaretti and Muro applied the same procedure to obtain an aerodynamic ROM [61], the **reduction of a complete, aeroelastic rotor into a frequency-domain transfer function**, the first part of the procedure presented in [60], is a valuable concept, which is further developed in this work.

1.3. Objective and Outline

The state of the art summarized above points out two facts regarding propeller whirl flutter prediction:

1. Whirl flutter prediction using the Houbolt/Reed method is well established in conjunction with frequency-domain flutter analysis but lacks a more detailed propeller model.

2. Accurate modeling of complex rotor configurations is possible within MBS or Rotorcraft comprehensive codes but, in most cases, restricted to the time domain.

Therefore, the available modeling toolset (in the time domain) does not fit the preferred analysis type (frequency domain) for propeller aircraft flutter stability. To close the gap and include, for example, blade elasticity and complex rotor aerodynamics in propeller whirl flutter analysis, two options are available:
One possible solution to this mismatch would be switching to time-domain analysis for propeller whirl flutter prediction, modeling the engine support or even full aircraft in time-domain simulation codes (as, e.g., demonstrated for the NASA X-57 [54]). While this does not require any additional methods to be developed because the tools and methods already exist, it has some limitations and problems. First, current fixed-wing flutter prediction workflows are heavily based on frequency-domain flutter analysis, and the procedures and models

(structure, unsteady aircraft aerodynamics) are tuned to this approach. Moving this whole process and the tuned models into time-domain simulation tools while preserving the prediction capability not only for whirl flutter but also for classical fixed-wing flutter mechanisms such as wing or control surface flutter is a difficult task. Second, time-domain analysis is more costly in terms of computational time. Broad parameter studies concerning payload and fuel loading or possible failure cases would take longer than in the frequency domain, prolonging the development process. Third, time-domain methods sometimes struggle to yield the same insight into a system behavior compared to frequency-domain analysis. For example, it is difficult to analyze beyond the first instability or not all system modes can be captured by identification routines.

The second solution to close the gap in the state of the art is to develop a method to bring time-domain rotor modeling capabilities into frequency-domain flutter analysis, enhancing the fidelity of aeroelastic propeller modeling within the existing flutter processes. This would allow aircraft manufacturers to stick to their existing flutter processes while profiting from advancements in rotor modeling made within time-domain tools.

This work provides such a method and covers the following three main objectives:

- To **develop** a method and workflow for propeller whirl flutter analysis in the frequency domain using propeller models derived from time-domain modeling tools.
- To **verify** the new method by comparing stability results to conventional time-domain analysis of the coupled propeller airframe system.
- To **apply** the new method to study the effects of blade elasticity and more detailed propeller aerodynamics on whirl flutter stability of a generic turboprop engine support.

The investigations in this thesis focus on the phenomenon of propeller whirl flutter and applications for propeller aircraft. While they might be used in the context of tiltrotor whirl flutter analysis, this is not within the scope of this work. Configurations with propellers with less than three blades are also not treated, as they become time-periodic due to the propeller inertia and have to be treated in the time domain. This thesis does not aim to provide validation of the stability results with experimental data or high-fidelity numerical simulations. The methodology is carefully verified using existing stability analysis methods and can be applied in future work to design and prepare validation studies. The examples in this thesis, especially regarding aerodynamic modeling, only comprise low- to mid-fidelity methods and do not treat CFD-aerodynamics (and therefore transonic effects) explicitly, as the main focus is on the methodology to enable a future use, e.g., of CFD-aerodynamics. A third limitation of this

work concerns the aerodynamic interaction with the wing. This work focuses on improving isolated propeller modeling, striving to replace the Houbolt/Reed method in frequency-domain flutter analysis. It remains compatible with the approach to interaction described by Rodden and Rose [14], but further investigations into the aspects of unsteady propeller-wing interaction are left for future work. The same applies to the airframe dynamic modeling. While the details of the dynamic representation of the engine support structure influence the whirl flutter predictions, this is considered out of the scope of this work.

To achieve the goals listed above, this thesis is divided into five main chapters to derive, verify, and apply the new method in a structured way:

- **Chapter 1** already presented the **motivation** for this work together with the current state of the art for propeller whirl flutter analysis.
- **Chapter 2** introduces the underlying **theory**, starting with the flutter analysis in the frequency domain, followed by the theory of representing propellers in the flutter analysis. This particular section contains the core methodology and workflow of the Transfer-Matrix or TM-method proposed in this work. Chapter 2 concludes with a brief look into the theory of propeller time-domain modeling and stability analysis.
- **Chapter 3** summarizes the **models** used to obtain the results of this work. They comprise the propeller and simplified engine suspension models used for most of the studies presented. A generic turboprop aircraft model for demonstration of the TM-method on full aircraft level is also described briefly.
- **Chapter 4** presents the **results** of this thesis. First, the verification of the TM-method using time-domain analysis is shown, followed by applications to study the effect of blade elasticity and propeller aerodynamic modeling. The applications mainly comprise results obtained with the simplified pylon model, but chapter 4 finishes with presenting results from applying the TM-method to a full aircraft configuration.
- **Chapter 5** concludes the thesis with a **discussion** of the TM-method and the results presented in the context of the current state of the art, highlighting the advancements made as well as current limitations. The closing outlook gives ideas for addressing those limitations and broadening the scope of the work presented here.

2 Theory

This chapter introduces the underlying theory of this work. The theory for aircraft flutter analysis in the frequency domain is presented first. The next section extends this with different models for the representation of propellers in the frequency-domain flutter equation, including the main theory of the Transfer-Matrix method. Because time-domain propeller models are a main component of the TM-method, their theory is briefly summarized. Finally, this chapter presents the theory for the time-domain stability analysis used as a reference method for verification later.

2.1. Flutter analysis in the frequency domain

The basic equation of motion for a free-flying aircraft in the time domain is written in Eq. 2.1. The left-hand side (LHS) represents the dynamics of the aircraft structure in physical coordinates $\boldsymbol{u}$. It comprises inertial forces ($\underline{M}\ddot{\boldsymbol{u}}$), viscous damping forces ($\underline{D}\dot{\boldsymbol{u}}$) and elastic forces ($\underline{K}\boldsymbol{u}$). These forces are balanced by the aerodynamic forces on the right-hand side (RHS), $\boldsymbol{F}_{aero}$.

$$\underline{M}\ddot{\boldsymbol{u}} + \underline{D}\dot{\boldsymbol{u}} + \underline{K}\boldsymbol{u} = \boldsymbol{F}_{aero}(t) \tag{2.1}$$

For flutter stability analysis, the eigenvalues of the system described by Eq. 2.1 need to be extracted[1]. This becomes unpractical for realistic models with many physical degrees of freedom $\boldsymbol{u}$. For this purpose, the equations of motion are transferred to modal or generalized coordinates $\boldsymbol{q}$ using the mode shapes $\underline{\Phi}$ of

[1] An overview of the theory and details of flutter stability analysis in the frequency domain can be found in standard aeroelasticity textbooks. Schwochow in his thesis [62] summarizes the theory.

the system (see Eq. 2.2). These mode shapes can be truncated for the lowest frequency modes, omitting high-frequency content in the model [62]. This drastically reduces the order of the system and transforms the mass, damping, and stiffness matrices into their generalized formulation (e.g., $\underline{M}_{gen}$).

$$\boldsymbol{u}(t) \;=\; \underline{\Phi}\boldsymbol{q}(t) \tag{2.2}$$

To facilitate the eigenvalue extraction, Eq. 2.1 is transformed in the Laplace domain, and the aerodynamic forces are split into external aerodynamic forces $\boldsymbol{F}_{aero,ext}$, such as the steady loading and perturbations by gusts, and motion-induced aerodynamic forces. The external aerodynamic forces are neglected for stability analysis, and only the motion-induced loads are retained. The motion-induced aerodynamic forces for small perturbations in the Laplace domain are expressed by a frequency-dependent generalized aerodynamic force (GAF) matrix $\underline{Q}_{gen}$, which relates the modal displacements $\boldsymbol{q}$ with the generalized forces. The generalized Laplace-domain equation of motion is written in Eq. 2.3.

$$\left[s^2\underline{M}_{gen} + s\underline{D}_{gen} + \underline{K}_{gen}\right]\boldsymbol{q} = \frac{\rho}{2}V^2\underline{Q}_{gen}(p, Ma)\boldsymbol{q} \;+\; \cancel{\boldsymbol{F}_{aero,ext}} \tag{2.3}$$

The GAFs depend on the non-dimensional Laplace variable p and the flight Mach number. The definition of p and its real part g (damping) and imaginary part k (frequency) using the flight speed V and a reference length c_{ref} are as follows:

$$p = \frac{(\sigma + i\omega)c_{ref}}{V} = \frac{sc_{ref}}{V} \quad , \quad k = \frac{\omega c_{ref}}{V} \quad , \quad g = \frac{\sigma c_{ref}}{V}. \tag{2.4}$$

The eigenvalues $\lambda = \sigma + i\omega$ of Eq. 2.3 determine the eigenbehavior of the aircraft. Due to the (nonlinear) dependency of the GAF matrix $\underline{Q}_{gen}$ on the non-dimensional Laplace variable p, the eigenvalues are not straightforward to find. Several methods to obtain them are described in the literature, and the most commonly used ones are described in the following.

p-method

In the case of an analytic description of $\underline{Q}_{gen}(s)$, e.g., from analytic derivations or rational function approximation, the eigenvalues of Eq. 2.3 can be computed directly [63]. Although these eigenvalues can be calculated precisely in this case, it shifts the problem from the eigenvalue analysis to finding a good approximation $\underline{Q}_{gen}(p)$, which is difficult to achieve for complex configurations in the whole Laplace domain.

p-k-method

Hassig [64] suggested an iterative solution to find the eigenvalues of Eq. 2.3, approximating the aerodynamic forces in the Laplace domain with those for pure harmonic motion, so on the imaginary axis (see Eq. 2.5). These are easier to compute, e.g., with the DLM [65]. The eigenvalues are therefore only exact for harmonic motion ($g = 0$, $p = ik$), although $\underline{Q}_{gen}(ik)$ is a good approximation for $\underline{Q}_{gen}(p)$ also for small damping values.

$$\underline{Q}_{gen}(p, Ma) \approx \underline{Q}_{gen}(ik, Ma) \tag{2.5}$$

For the algorithm, the airspeed V in Eq. 2.3 is fixed, and the reduced frequency k, which is used to compute the value of $\underline{Q}_{gen}$, is changed in iterations until it matches the imaginary part of the calculated eigenvalue p. This is repeated over a range of airspeed and for all system modes to obtain frequency and damping of all aeroelastic modes throughout the airspeed range. Mode tracking [66] inside the iterations is used to ensure convergence for all aeroelastic modes and operating points. Further, instead of recomputing $\underline{Q}_{gen}(ik, Ma)$ in each iteration, a few sampling points are used to compute and then consecutively interpolate $\underline{Q}_{gen}$.

g-method

To improve the damping predictions of the p-k-method, Chen [67] suggested to extrapolate the unsteady aerodynamic forces from the imaginary axis into the Laplace domain using a Taylor series expansion (see Eq. 2.6) and making use of the assumption that $\underline{Q}_{gen}(p)$ is analytic.

$$\underline{Q}_{gen}(p, Ma) \approx \underline{Q}_{gen}(ik, Ma) + g\frac{d\underline{Q}_{gen}(ik, Ma)}{dik} \tag{2.6}$$

This reduces to the p-k assumption in the flutter point at zero damping ($g = 0$) and delivers the same flutter speed as the p-k method. The damping predictions outside the flutter point are improved.

Pole fitting

The eigenvalues of Eq. 2.3 can also be interpreted as the poles of the aeroelastic systems transfer function $\underline{H}_{system}(s)$ between generalized forces and displacements. The equation can be reshaped into Eq. 2.7 for this purpose. For harmonic motion, the frequency response function $\underline{H}_{system}(i\omega)$ can be evaluated exactly for sample points along the imaginary axis.

$$\underline{H}_{system}(s) = \left[s^2 \underline{M}_{gen} + s\underline{D}_{gen} + \underline{K}_{gen} - \frac{\rho}{2} V^2 \underline{Q}_{gen}(ik, Ma) \right]^{-1} \tag{2.7}$$

Pole-fitting routines such as vector fitting [68, 69, 70] can be used to extract the poles from the coupled frequency response function. The frequency and damping of the identified modes can be extracted from the complex poles. Repeating this process for a set of airspeeds V results in similar results as the iteration-based methods (p-k, g-method).

Results of a flutter analysis

After extracting the eigenvalues λ from Eq. 2.3, the circular frequency ω, the associated frequency f and critical damping ζ are extracted from the complex eigenvalues according to Eq. 2.8

$$\omega = \mathrm{Im}(\lambda) \ ; \ f = \frac{\omega}{2\pi} \ ; \ \zeta = \frac{\mathrm{Re}(\lambda)}{|\lambda|} \tag{2.8}$$

A complex eigenvector is also extracted from Eq. 2.3 for each complex eigenvalue. The complex eigenvector contains the participation (amplitude and phase) of each modal DOF of the components in $\boldsymbol{q}$ in the aeroelastic mode associated with the eigenvalue. The eigenvector is also used to track individual aeroelastic modes through the operating range studied.

As a result of the flutter analysis (regardless of the solution algorithm), the frequency and damping results for each aeroelastic mode are known over a range of, e.g., airspeed. Fig. 2.1 shows an example of such a flutter analysis of the simplified pylon system from Fig. 1.1(b). The system has two aeroelastic modes, the forward and backward whirl mode. The frequency and damping of each mode vary with increasing airspeed on the x-axis. Around 127 m/s true airspeed, the damping of the backward whirl mode becomes negative,

indicating instability and, therefore, flutter. From that point on, the system is unstable, and small oscillations increase in amplitude. Predicting the frequency and damping of the aeroelastic modes to find this point of instability and the underlying coupling mechanism described by the associated eigenvector is the goal of the aircraft flutter analysis.

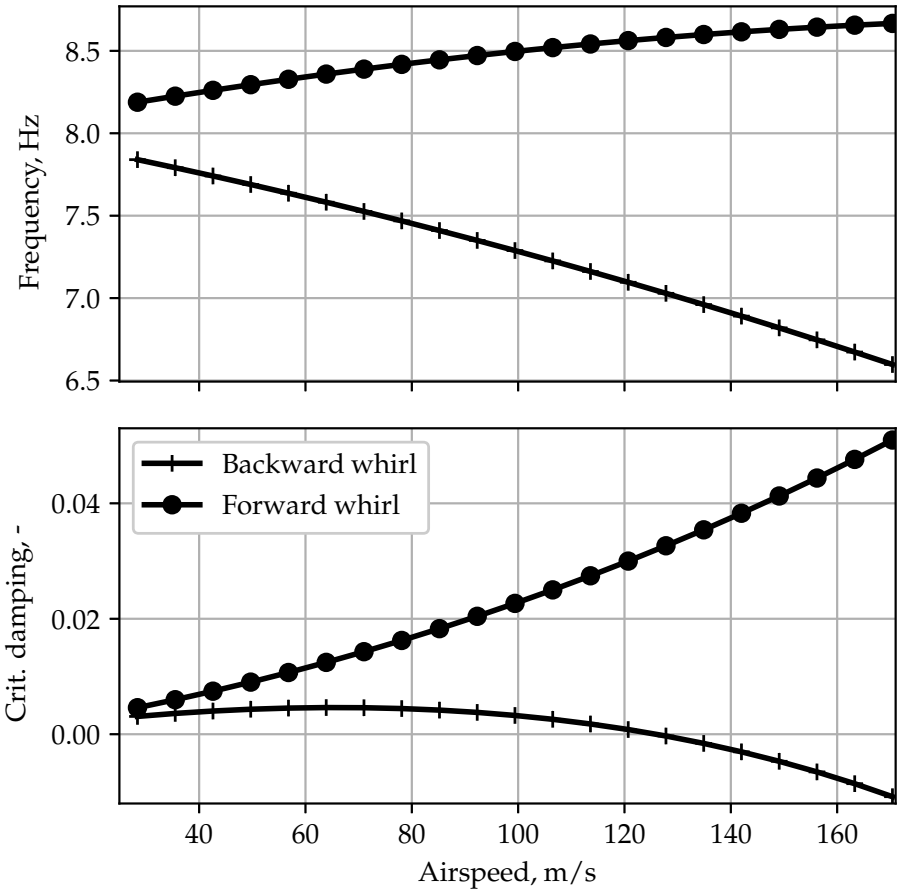

Figure 2.1.: Example flutter results for the simplified pylon system with the frequency (top) and damping (bottom) trends over airspeed.

2.2. Propeller representation in the frequency domain

Section 2.1 described the theory for general flutter analysis of an aircraft in the frequency domain. To capture whirl flutter within this analysis, the flutter equation 2.3 has to be extended to include the motion-induced loads of the propeller. The main theory is described in an earlier publication by the author [71] and reproduced in greater detail here. Eq. 2.9 represents the extended flutter equation with the motion-induced propeller loads $\boldsymbol{F}_{gen,prop}$ in generalized coordinates. They can generally depend on the Laplace variable s and the generalized coordinates $\boldsymbol{q}$. They will vary with the aircraft's and propeller's operating point (airspeed V, Mach number Ma, rotational speed Ω). One assumption in Eq. 2.9 concerns the number of blades. For one- or two-bladed propellers, the unsteady aerodynamic loads on the propeller hub are inherently time-dependent and can not be described purely in the frequency domain (compare, e.g., Johnson [34]). Therefore, Eq. 2.9 is only valid for propellers with three or more blades.

$$\left[s^2\underline{M}_{gen} + s\underline{D}_{gen} + \underline{K}_{gen}\right]\boldsymbol{q} = \frac{\rho}{2}V^2\underline{Q}_{gen}(p, Ma)\boldsymbol{q} + \boldsymbol{F}_{gen,prop}(s, \boldsymbol{q}, V, \Omega, Ma) \tag{2.9}$$

The generalized form of the propeller loads can be derived from the modal transformation of the loads about the propeller hub, using the modal matrix for the propeller hub node, $\underline{\Phi}_{hub}$. The propeller hub node is a single reference point to which the propeller loads can be referenced and transferred to the structural model (see Fig. 2.2). The modal transformation with $\underline{\Phi}_{hub}$ can be used to obtain the physical displacements of the propeller hub $\boldsymbol{x}_{hub}$ (see left side of Fig. 2.2) from the generalized coordinates $\boldsymbol{q}$ as described in Eq. 2.10. In the other direction, it projects the forces at the propeller hub $\boldsymbol{F}_{prop,hub}$ (see right side of Fig. 2.2) back onto the generalized propeller loads $\boldsymbol{F}_{gen,prop}$ that are part of Eq. 2.9. A sufficient number of modes should be used in the modal matrix $\underline{\Phi}_{hub}$ to correctly capture the possible motions of the propeller hub node (translations and rotations).

$$\boldsymbol{x}_{hub} = \underline{\Phi}_{hub}\boldsymbol{q} \quad , \quad \boldsymbol{F}_{gen,prop}(s, V, \Omega, Ma) = \underline{\Phi}_{hub}^T\, \boldsymbol{F}_{prop,hub} \tag{2.10}$$

The propeller hub displacements $\boldsymbol{x}_{hub}$ and hub loads $\boldsymbol{F}_{prop,hub}$ have six components each, comprising three translations (x, y and z) and three corresponding rotations (ϕ, θ and ψ), where x denotes the propeller axis and y and z span the propeller plane:

$$\boldsymbol{x}_{hub} = \begin{bmatrix} x \\ y \\ z \\ \phi \\ \theta \\ \psi \end{bmatrix}_{hub} , \quad \boldsymbol{F}_{prop,hub} = \begin{bmatrix} F_x \\ F_y \\ F_z \\ M_x \\ M_y \\ M_z \end{bmatrix}_{hub} \tag{2.11}$$

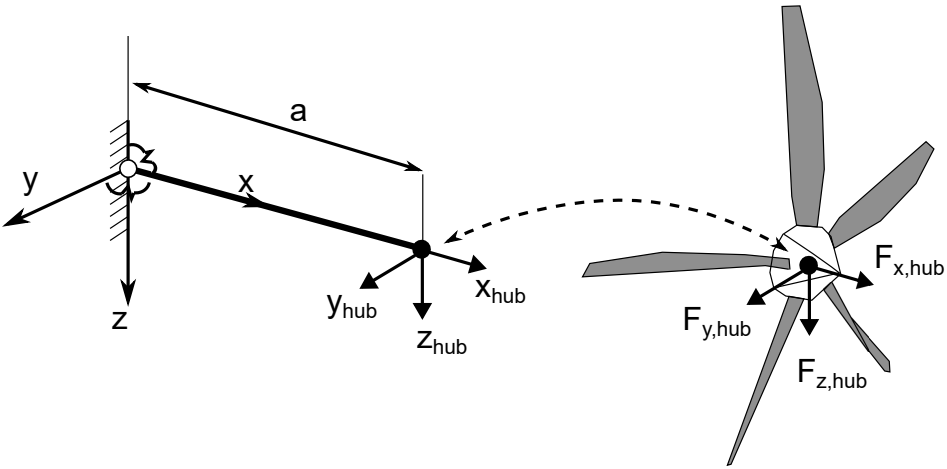

Figure 2.2.: Separation of the simplified pylon system into pylon and propeller, denoting the hub displacements $\boldsymbol{x}_{hub}$ and the hub loads $\boldsymbol{F}_{prop,hub}$.

The benefit of this coordinate transformation back into physical hub coordinates is that it is easier to find a relation between motion-induced loads and displacement. For stability analysis, small perturbations $\Delta\boldsymbol{x}_{hub}$ can be assumed, and a linear relationship between loads and displacements is written as in Eq. 2.12.

$$\boldsymbol{F}_{prop,hub} = \underline{H}_{prop}(s, V, \Omega, Ma)\ \Delta\boldsymbol{x}_{hub} \tag{2.12}$$

$\underline{H}_{prop}$ represents the linear, frequency-dependent transfer function from propeller hub displacements to propeller hub loads (also called transmittance in the literature [59]). Because $\Delta\boldsymbol{x}_{hub}$ and $\boldsymbol{F}_{prop,hub}$ are both vectors with six entries, $\underline{H}_{prop}$ is a square six-by-six matrix, the so called **transfer matrix**, as shown in Eq. 2.13. Each entry is a frequency-dependent transfer function projecting one hub displacement (e.g., rotation about the y-axis θ) with one hub load component (e.g., the moment about z, M_z). The resulting transfer function (in this example, $M_{z\theta}$) is a scalar, frequency-dependent transfer function.

Similar to $\boldsymbol{F}_{gen,prop}$ in Eq. 2.9, the transfer matrices are not only frequency-dependent but also vary with the operating point (e.g., V, Ma and Ω).

$$\underline{H}_{prop}(s, V, \Omega, Ma) = \begin{bmatrix} F_{xx} & F_{xy} & F_{xz} & F_{x\phi} & F_{x\theta} & F_{x\psi} \\ F_{yx} & F_{yy} & F_{yz} & F_{y\phi} & F_{y\theta} & F_{y\psi} \\ F_{zx} & F_{zy} & F_{zz} & F_{z\phi} & F_{z\theta} & F_{z\psi} \\ M_{xx} & M_{xy} & M_{xz} & M_{x\phi} & M_{x\theta} & M_{x\psi} \\ M_{yx} & M_{yy} & M_{yz} & M_{y\phi} & M_{y\theta} & M_{y\psi} \\ M_{zx} & M_{zy} & M_{zz} & M_{z\phi} & M_{z\theta} & M_{z\psi} \end{bmatrix} \tag{2.13}$$

Inserting Eq. 2.12 together with the modal transformation in Eq. 2.10 into the flutter equation with propeller loads 2.9 yields the final, frequency-domain flutter equation including propeller transfer matrices in Eq. 2.14. Solving for the eigenvalues of Eq. 2.14 yields the eigenfrequencies and dampings of the airframe modes, including those of the propeller whirl modes.

$$\begin{aligned} \left[s^2\underline{M}_{gen} + s\underline{D}_{gen} + \underline{K}_{gen}\right]\boldsymbol{q} &= \frac{\rho}{2}V^2\underline{Q}_{gen}(p, Ma)\boldsymbol{q} \\ &+ \underline{\Phi}_{hub}^T\underline{H}_{prop}(s, V, \Omega, Ma)\underline{\Phi}_{hub}\boldsymbol{q} \end{aligned} \tag{2.14}$$

Different formulations exist for $\underline{H}_{prop}$, including the propeller gyroscopics, the formulation derived by Houbolt and Reed, and the identified transfer matrices of the TM-method, the core concept of this work. The different formulations will be explored in the following subsections.

2.2.1. Gyroscopics

One major influence of the rotating propeller (and engine) is the gyroscopic coupling between pitch and yaw motion. This dynamic coupling due to the rotational inertia leads to the whirling motion in the first place, which can then become unstable under the influence of motion-induced aerodynamics. For the coordinate system depicted in Fig. 2.2, the gyroscopic coupling matrix becomes a skew-symmetric viscous damping matrix as in Eq. 2.15 [5, Chap. 2.1]. J_p represents the polar inertia of the propeller (second mass moment of inertia about the propeller axis) and Ω the rotational speed. Rotating components of the engine, such as the gearbox and the turbine, can be included via separate gyroscopic matrices or by reducing their polar inertia with the ratio of the rotational speeds to the propeller shaft. It is important, however, to keep the direction of the rotational speed in mind. Eq. 2.15 assumes a positive rotation

about the x-axis (counter-clockwise looking from the front). For any component (including the propeller itself) with an opposite direction of rotation, Ω has to be inserted with a negative sign into Eq. 2.15.

$$\underline{H}_{prop}(s,\Omega) \;=\; s\underline{G}(\Omega) \;=\; s\begin{bmatrix} 0 & 0 & 0 & 0 & 0 & 0 \\ 0 & 0 & 0 & 0 & 0 & 0 \\ 0 & 0 & 0 & 0 & 0 & 0 \\ 0 & 0 & 0 & 0 & 0 & 0 \\ 0 & 0 & 0 & 0 & 0 & -J_p\Omega \\ 0 & 0 & 0 & 0 & J_p\Omega & 0 \end{bmatrix} \tag{2.15}$$

The effect of engine gyroscopics on classical aircraft flutter is small and mostly stabilizing due to the coupling of symmetric and anti-symmetric modes [72]. For whirl flutter, however, it plays a significant role in the instability mechanism. Hence, the gyroscopic matrix should always be included in Eq. 2.14.

2.2.2. Houbolt/Reed method

The method of Houbolt and Reed [8] was presented in 1962 and describes the motion-induced aerodynamic forces on a propeller. Rodden and Rose [14] presented a few additions to the method. The equations in the following are taken from their formulation.

The key concept of the Houbolt/Reed method is the description of the motion-induced aerodynamic hub loads by non-dimensional stiffness and damping derivatives, which are analytically derived from strip theory. For the detailed derivation, the reader can refer to the original paper [8] or the book of Čečrdle [5, Chap. 5.4ff]. The equations for the hub loads based on the propeller derivatives can be rewritten in matrix form to comply with the form of Eq.2.12. Eq. 2.16-2.18 present the formulation of $\underline{H}_{prop}$ using the aerodynamic stiffness ($\underline{K}_{prop}$) and damping matrix ($\underline{D}_{prop}$) [19]. Only motion and load components in the propeller plane are considered in the theory, and DOF x and ϕ are neglected (see the zero rows and columns in Eq. 2.18).

$$\underline{H}_{prop}(s,V,\Omega,Ma) \;=\; \pi R^3\rho V^2(\underline{K}_{prop} + s\underline{D}_{prop}) \tag{2.16}$$

$$\underline{K}_{prop} = \begin{bmatrix} 0 & 0 & 0 & 0 & 0 & 0 \\ 0 & 0 & 0 & 0 & \frac{C_{y\theta}}{2R} & \frac{C_{y\psi}}{2R} \\ 0 & 0 & 0 & 0 & \frac{C_{z\theta}}{2R} & \frac{C_{z\psi}}{2R} \\ 0 & 0 & 0 & 0 & 0 & 0 \\ 0 & 0 & 0 & 0 & C_{m\theta} & C_{m\psi} \\ 0 & 0 & 0 & 0 & C_{n\theta} & C_{n\psi} \end{bmatrix} \tag{2.17}$$

$$\underline{D}_{prop} = \begin{bmatrix} 0 & 0 & 0 & 0 & 0 & 0 \\ 0 & -\frac{C_{y\psi}}{2RV} & \frac{C_{y\theta}}{2RV} & 0 & \frac{C_{yq}}{2V} & \frac{C_{yr}}{2V} \\ 0 & -\frac{C_{z\psi}}{2RV} & \frac{C_{z\theta}}{2RV} & 0 & \frac{C_{zq}}{2V} & \frac{C_{zr}}{2V} \\ 0 & 0 & 0 & 0 & 0 & 0 \\ 0 & -\frac{C_{m\psi}}{V} & \frac{C_{m\theta}}{V} & 0 & \frac{C_{mq}R}{V} & \frac{C_{mr}R}{V} \\ 0 & -\frac{C_{n\psi}}{V} & \frac{C_{n\theta}}{V} & 0 & \frac{C_{nq}R}{V} & \frac{C_{nr}R}{V} \end{bmatrix} \tag{2.18}$$

In Eq. 2.17 and 2.18, C_{ab} denotes the non-dimensional derivatives, describing the load component a due to the motion component b [2]. For example, $C_{n\theta}$ describes the non-dimensional moment M_z due to a steady propeller disc inclination (pitch) angle θ. The derivatives and $\underline{H}_{prop}$ depend on the propeller geometry and operating point. Eq. 2.19 shows one example for the analytical equation, in this case for the derivative $C_{n\theta}$, using the definitions in Eq. 2.20.

$$C_{n\theta} = -\left(\frac{N_b}{4}\right)\left(\frac{1}{\pi R}\right)\int_{\eta_{hub}}^{1} \frac{\eta^2}{\sqrt{\mu^2+\eta^2}}\, C_{Ar}\; c(\eta)\; C_{l\alpha}(\eta)\; \mathrm{Re}(\gamma(k))d\eta \tag{2.19}$$

with

$$\mu = \frac{V}{\Omega R}\ ,\ \eta = r/R\ ,\ k = \frac{c}{2R\sqrt{\mu^2+\eta^2}} \tag{2.20}$$

The derivates mainly consist of an integral along the non-dimensional propeller radius η, starting at the spinner η_{hub}. The integral comprises a factor for the velocity triangle at the blade section (using the propeller advance ratio μ), the blade chord distribution $c(\eta)$, the local blade lift curve slope $C_{l\alpha}(\eta)$ and several correction factors. The first factor accounts for the unsteady lift lag effect using Theodorsen's function $\gamma(k)$ with the local reduced frequency k, in this case, only accounting for the rotational frequency Ω instead of the oscillation frequency ω. The factor is omitted for the quasi-steady approximation of the Houbolt/Reed method ($\gamma(k) = 1$). The second factor, C_{Ar}, accounts for the finite blade span

[2] Note that in the Houbolt/Reed method, the moment M_y is denoted as m and the moment M_z as n. The rotational velocity about the y-axis is denoted as p, and r denotes the rotational velocity about the z-axis.

(similar to a tip loss factor) and the compressibility using a Mach-correction (see Eq. 2.21). The third correction factor, $N_B/4$, accounts for the number of blades because the method by Houbolt and Reed was initially developed for a four-bladed propeller. The definitions for all other coefficients are given in App. A.1, where some derive from axial symmetry.

$$C_{Ar} = \frac{Ar}{2 + Ar\sqrt{1 - Ma^2(1 + (\frac{\eta}{\mu})^2)}} \ , \ Ar \ = \ \frac{R(1 - \eta_0^2)}{\int_{\eta_{hub}}^{1} c(\eta) d\eta} \tag{2.21}$$

Due to its analytical nature, the Houbolt/Reed method is fast and robust. The derivatives and therefore $\underline{H}_{prop}$ can be calculated for every flight point and inserted into the flutter equation 2.14. However, some assumptions in its derivation limit the modeling capabilities of the method. The main assumptions are:

1. The propeller blades are assumed to be completely rigid; no blade elasticity is considered.
2. The steady angle of attack at the local blade section is assumed to be zero. The formulation is, therefore, only valid for zero thrust and torque (windmilling case).
3. No induced velocity (due to circulatory lift on the blades) is considered.
4. Due to the use of strip theory, the radial blade sections are considered independent of each other. A correction derived for finite wings using the aspect ratio is used to consider tip-loss effects.
5. No unsteady aerodynamics are considered. The formulation with stiffness and damping is quasi-steady. The correction using Theodorsen's function for the local blade lift lag effect assumes the rotational speed to be much higher than the oscillation frequency ($\Omega >> \omega$).
6. The method only applies to propellers with three or more blades.

Before describing the Transfer-Matrix method, developed to overcome all but the last limitations, some fundamental relations of unsteady propeller aerodynamics and whirl flutter stability are presented using the Houbolt/Reed method.

Basic relations of unsteady propeller aerodynamics and whirl flutter

Tab. 2.1 lists the eight unique derivatives (and their corresponding axial-symmetric counterparts) for an example propeller for the regular Houbolt/Reed theory as well as for the quasi-steady formulation, omitting the unsteady correction with the Theodorsen-function in Eq. 2.19. The first four derivatives

are aerodynamic stiffness terms, representing steady loads resulting from a steady deflection of the propeller (introduced in chapter 1 as 1P hub loads). The last four rows contain damping derivatives resulting from a rotational velocity of the propeller disc.
By comparing the regular and the quasi-steady derivatives, two main effects of unsteady aerodynamics become apparent: first, for the quasi-steady formulation, half of the derivatives are zero, and second, those that are not zero are predicted higher than for the regular theory with unsteady correction. The first effect, the missing derivatives, can be explained by the omitted unsteady phase lag. Because the induced angle-of-attack distribution by a disc pitch angle is anti-symmetric about the z-axis, so is the resulting quasi-steady lift distribution. The phase lag due to the Theodorsen function results in a phase lag in the azimuth direction, creating force and moments about the y-axis (for the stiffness terms). The second effect, the smaller amplitudes, stems from the lift deficiency in the Theodorsen function, resulting in a reduction in the amplitude of the unsteady lift and, therefore, in the derivatives.

Table 2.1.: Houbolt/Reed derivatives using regular and quasi-steady formulation

Derivative	Axial-Symmetric Derivative	Regular Houbolt/Reed	Quasi-steady Houbolt/Reed
$C_{y\theta}$	$C_{z\psi}$	-0.047	0
$C_{z\theta}$	$-C_{y\psi}$	-0.268	-0.308
$C_{m\theta}$	$C_{n\psi}$	0.011	0
$C_{n\theta}$	$-C_{m\psi}$	0.066	0.074
C_{yq}	C_{zr}	0.131	0.148
C_{zq}	$-C_{yr}$	-0.021	0
C_{mq}	C_{nr}	-0.051	-0.056
C_{nq}	$-C_{mr}$	-0.008	0

Fig. 2.3 shows the fifth column of the resulting unsteady transfer matrix $\underline{H}_{prop}$ for a frequency range up to 30 Hz for the regular Houbolt/Reed theory. It is seen that the z-force and moment (two plots on the right) are mainly stiffness-dominated, as they show almost no dependency on the frequency. The y-terms (two plots on the left) have some stiffness associated (amplitude at a frequency equal to zero) but are mainly damping terms due to their linear slope in the transfer function.

Due to the explicit dependency of the Houbolt-Reed transfer matrices $\underline{H}_{prop}$ on the Laplace-variable s, the equations of motion 2.9 for the simplified pylon system from Fig. 1.1(b) can be solved directly using the p-method (a simple eigenvalue analysis in this case). Repeating the analysis for different combinations of

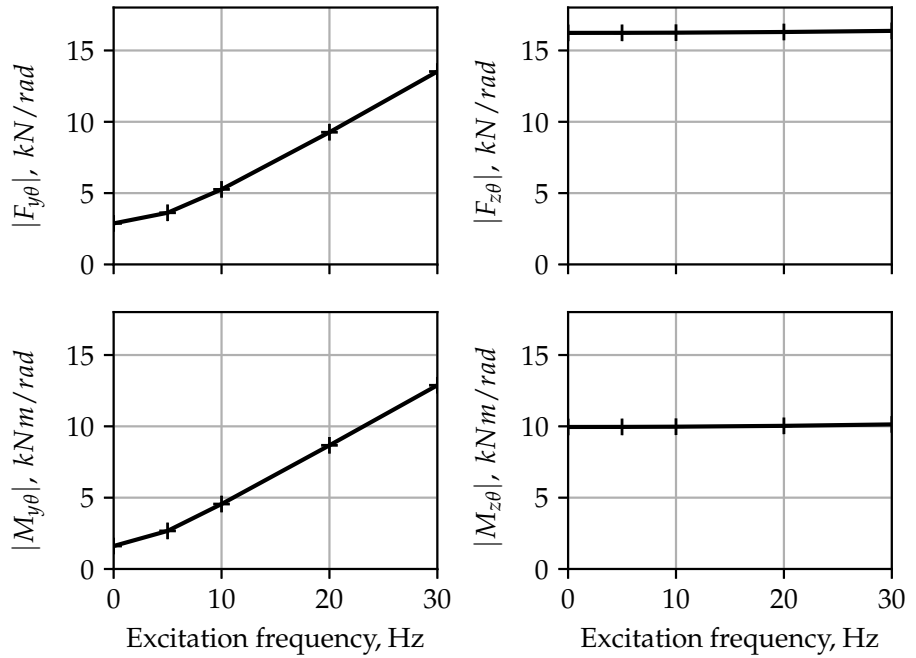

Figure 2.3.: Fifth column of $|\underline{\underline{H}}_{prop}|$ for Houbolt/Reed method, evaluated for an example propeller for harmonic excitation $s = i\omega$ up to 30 Hz.

pitch and yaw spring stiffness (K_θ and K_ψ) allows us to derive the stability map of the system in Fig. 2.4 and, respectively, the required stiffness (or uncoupled frequency as shown in the plot) for stability. The most critical stiffness combination is equal pitch and yaw frequency, so on the bisecting line in Fig. 2.4. The required pitch (or yaw) frequency is used as a stability measure, and the relative change of this required frequency measures any change in stability due to parameter variations. Eq. 2.22 defines $\Delta\omega_{stab}$ for a variation in parameter i relative to the reference stability map $\omega_{stab,ref}$.

$$\Delta\omega_{stab} = \frac{\omega_{stab,i} - \omega_{stab,ref}}{\omega_{stab,ref}} \tag{2.22}$$

A positive $\Delta\omega_{stab}$ represents a shift of the stability towards higher frequencies and, therefore, a more unstable system (as indicated in Fig. 2.4) This relative measure concerning a reference configuration is used throughout this thesis to

quantify the impact of parameter variation on the whirl stability of a simplified pylon system.

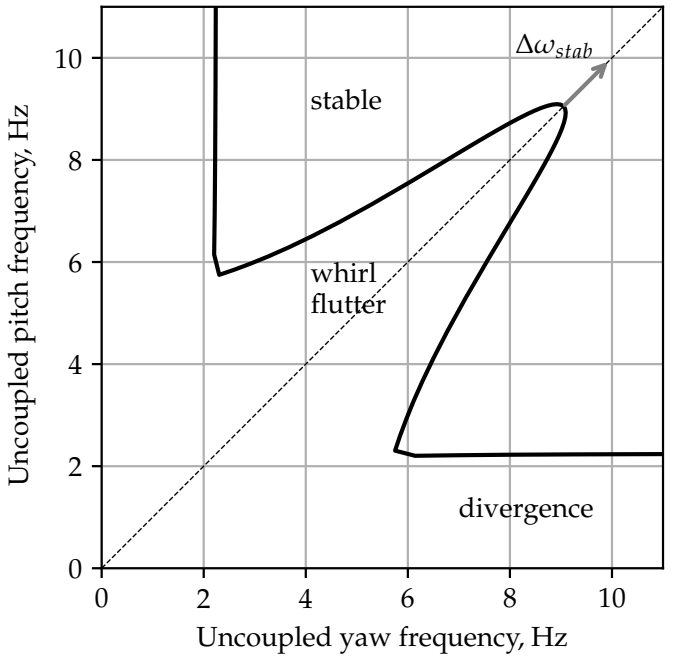

Figure 2.4.: Baseline whirl flutter stability map with measure $\Delta\omega_{stab}$ for quantifying changes in stability.

The simplified pylon system from Fig. 1.1(b) can experience a second kind of instability, which is also indicated in the stability map in Fig. 2.4: static divergence. The vertical force due to pitch angle, $C_{z\theta}$, increases the pitch angle further and has to be counteracted by elastic forces in the structure [5]. If the stiffness in one direction becomes too small, the aerodynamic force drives the system into static divergence. The two straight lines parallel to the x- and y-axis in Fig. 2.4 mark the area of static divergence. This phenomenon is irrelevant for turboprop structures due to the relatively high stiffness [5].

The derivatives in Tab. 2.1 influence whirl flutter stability by either stabilizing or destabilizing whirl flutter. The driving term behind the instability of the backward whirl mode is the cross-coupling moment derivative $C_{n\theta}$ (and the corresponding $C_{m\psi}$ [3]), as it couples pitch and yaw motion and acts in the

[3] In the following, for conciseness the axial symmetry will only be mentioned in special cases.

direction of the backward whirl mode [5]. The vertical force component $C_{z\theta}$ was already described to cause static divergence but also dampens the whirling motion. The moment due to pitch velocity C_{mq} also dampens the backward whirl motion (see [5, Fig. 2.5-2.7]).

These stabilizing and destabilizing effects are explored in more detail in Fig. 2.5. The eight plots present the sensitivity of whirl flutter (i.e., the extent of the stability boundary measured using $\Delta\omega_{stab}$) when the respective derivative (and the axial-symmetric counterpart) are scaled relative to the reference configuration from Tab. 2.1 and Fig. 2.4. Each derivative is modified with a scale factor between -20 % and +20 %. A positive slope of the line in the plot indicates a destabilizing contribution, as an increase in the derivative leads to an extension of the whirl flutter area. Fig. 2.5 identifies $C_{n\theta}$ as the primary destabilizing term, while the force stiffness derivatives $C_{y\theta}$ and $C_{z\theta}$ as well as the moment damping term C_{mq} are the main stabilizing contributors. The remaining derivatives have only a minor impact on the stability.

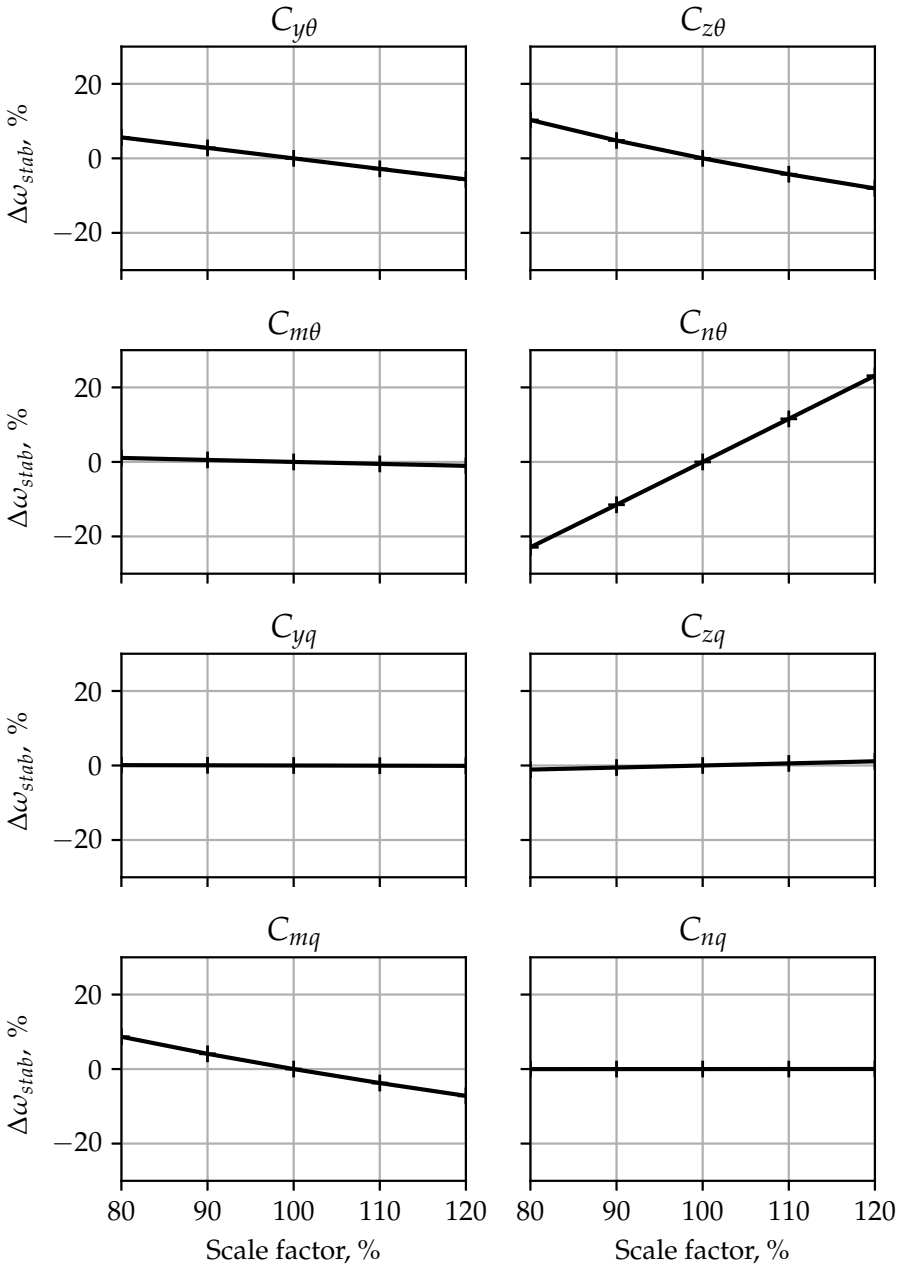

Figure 2.5.: Sensitivity of whirl flutter stability concerning the propeller derivatives

2.2.3. Transfer-Matrix method

The method by Houbolt and Reed explained before formulates analytical relations between propeller hub motion and loads, compare, for example, Eq. 2.19. The assumptions inherent to this theory are also listed in section 2.2.2, and overcoming them with analytical derivations becomes increasingly involved. The Transfer-Matrix (TM-)method instead relies on an aeroelastic time-domain simulation model for the propeller (see section 2.3) and identifies the transfer matrices $\underline{\underline{H}}_{prop}$ using time simulations. This allows identifying the complete six-by-six transfer matrix, as shown in Eq. 2.23, including the DOF in x and ϕ.

$$\underline{\underline{H}}_{prop}(s, V, \Omega, Ma) = \begin{bmatrix} F_{xx} & F_{xy} & F_{xz} & F_{x\phi} & F_{x\theta} & F_{x\psi} \\ F_{yx} & F_{yy} & F_{yz} & F_{y\phi} & F_{y\theta} & F_{y\psi} \\ F_{zx} & F_{zy} & F_{zz} & F_{z\phi} & F_{z\theta} & F_{z\psi} \\ M_{xx} & M_{xy} & M_{xz} & M_{x\phi} & M_{x\theta} & M_{x\psi} \\ M_{yx} & M_{yy} & M_{yz} & M_{y\phi} & M_{y\theta} & M_{y\psi} \\ M_{zx} & M_{zy} & M_{zz} & M_{z\phi} & M_{z\theta} & M_{z\psi} \end{bmatrix} \tag{2.23}$$

The origin of this method was developed by Gori et al. [60] to obtain a ROM for a helicopter rotor for flight mechanics applications. The initial method includes a three-step process to obtain a time-domain ROM using a rational matrix approximation of $\underline{\underline{H}}_{prop}$. The original method is explained briefly in the next paragraph, followed by the version adapted in this thesis for frequency-domain whirl flutter analysis. Required for the application of both versions of the TM-method are:

- A time-domain aeroelastic simulation model for the isolated propeller or rotor.
- The isolated rotor model has to be stable.
- The solver used for integrating the time-domain model needs restart capabilities, as several time integrations starting from the same (trimmed) operating point are necessary.
- The total hub loads $F_{prop,hub}$ for a simulation with prescribed hub motion Δx_{hub} have to be recovered.

ROM-procedure according to Gori et al.

The main goal of the method by Gori et al. [60] is to obtain a time-domain, finite state ROM for a helicopter rotor in steady flight. This ROM represents a linearized but computationally more efficient version of the complex simulation

model used to identify it. After identification, the ROM can be coupled with an airframe model, e.g., for flight mechanics and controller design.

The main steps for reducing an aeroelastic rotor model into a ROM can be separated into identifying the frequency-domain transfer function for the rotor hub and converting it into a time-domain ROM. For the first step, identifying frequency domain transfer functions, the rotor hub motion[4] Δx_{Hub} is perturbed by a harmonic motion of small amplitude. The response of the rotor hub forces $F_{Prop,Hub}$ is recorded until the transient response is decayed. The response of the rotor hub forces is recorded in the time domain and transformed into the frequency domain using a Discrete Fourier Transform. Only the first harmonic of the perturbation frequency is retained, as the goal is to achieve a linear, time-invariant aeroelastic transfer function (single harmonic input yields single harmonic output). Eventual higher harmonic content, e.g., resulting from periodicity in forward flight, is neglected. To obtain a clean frequency-domain transfer function, an integer multiplier of the perturbation period is used for the integration time while ensuring it is long enough to avoid spectral leakage [60]. The aeroelastic transfer function for the rotor $\underline{H}_{prop}$ is identified by repeating this process for all hub motion components and several perturbation frequencies.

Because the main goal is to obtain a time-domain ROM, a rational matrix approximation (RMA) for $\underline{H}_{prop}$ is found [60] and afterwards transformed into a state-space model. The RMA takes the frequency-domain samples for $\underline{H}_{prop}$ on the imaginary axis as an input and fits a rational matrix model as shown in Eq. 2.24 to the data. For a description of the RMA procedure, compare Gori et al. [60, Appendix 2]. The resulting matrices are an optimal approximation for the given frequency-domain data while expanding into the Laplace domain.

$$\underline{H}_{prop}(s) \approx s^2\underline{A}_2 + s\underline{A}_1 + \underline{A}_0 + \underline{C}[s\underline{I} - \underline{A}]^{-1}\underline{B} \tag{2.24}$$

Eq. 2.24 can be rewritten in the time-domain as a state-space model for the propeller hub forces $\boldsymbol{F}_{prop}(t)$, shown in Eq. 2.25. The poles of the RMA in matrix $\underline{A}$ in Eq. 2.24 become the states of the system, which takes the hub motion $\boldsymbol{x}_{hub}$ and its derivatives as an input.

$$\begin{aligned} \boldsymbol{F}_{prop}(t) &= \underline{A}_2\ddot{\boldsymbol{x}}_{hub} + \underline{A}_1\dot{\boldsymbol{x}}_{hub} + \underline{A}_0\boldsymbol{x}_{hub} + \underline{C}\boldsymbol{r} \\ \dot{\boldsymbol{r}} &= \underline{A}\boldsymbol{r} + \underline{B}\boldsymbol{x}_{hub} \end{aligned} \tag{2.25}$$

In the final step, the resulting state-space ROM can be coupled with a state-space airframe model (e.g., using compatibility conditions at the hub interface

[4] The original method from Gori et al. also includes control DOF, e.g., considering swashplate inputs. These are irrelevant to the propeller case and are omitted here.

for displacements and loads). The coupled model can be used for fast time integration in flight mechanics analysis, control design, or even real-time applications [60]. The coupled system can also be evaluated for aeroelastic stability (e.g., by eigenanalysis of the coupled system matrix). The poles of the RMA also appear in the eigenvalues of the coupled system, representing, e.g., elastic rotor DOF or aerodynamic states from unsteady aerodynamics (for more detailed insights into the RMA states, compare Gori et al. [60, Appendix 1]).

The method, as summarized here, was initially developed for helicopter rotors in hover and forward flight[5]. Complex time-domain simulation models, including elastic blade formulations and unsteady aerodynamics, can be used. The method was verified using indicial response simulations with the full model and recovered the hub load time histories [60].

Although the resulting ROM is fast to evaluate, the necessity to perform multiple harmonic perturbations makes the initial creation costly in terms of computational time. From a methodological perspective, the return to a time-domain state-space model and the rational matrix approximation connected to this step is required for, e.g., controller design. A representation in the frequency domain is sufficient for aeroelastic (whirl) flutter stability analysis, avoiding the complicated RMA steps.

Frequency-domain Transfer-Matrix method

From the perspective of propeller whirl flutter, the method of Gori et al. [60] offers promising advantages by allowing the reduction of an arbitrary time-domain rotor model into a ROM, which can afterwards be coupled to a support structure, e.g., an airframe. The disadvantages of high computational time and complex rational matrix approximation have to be overcome to allow compatibility with current aircraft flutter analysis processes.
For this purpose, the main idea of the first part of the method developed by Gori et al. [60], the identification of a frequency-domain transfer function from rotor hub motion to hub loads using time-domain perturbations, is kept and embedded into a new framework, the so-called **Transfer-Matrix method** (or short TM-method). The TM-method is tailored to frequency-domain whirl flutter analysis, and the main goal is to obtain a frequency-domain representation of the propeller efficiently. The theory was first described by the author in [71] and further developed in later publications [73, 74, 75, 76, 77].

For the special case of turboprop whirl flutter analysis, some simplifications can be applied:

[5] for the latter as an approximation due to the lack of higher harmonic response terms

- Due to the fast-forward flight, aircraft propellers usually operate in (nearly) axial flight conditions. This means the inflow velocity is parallel to the rotational axis, and the system becomes time-invariant. Small angles of attack are neglected.
- The propeller pitch control system dynamics are neglected, and the only interface for motion and loads is the propeller hub node, equivalent to Fig. 2.2. Gori et al. [60] also include the possibility of rotor control inputs, e.g., via swashplate motion, but this is usually not applicable for propellers.

These simplifications are applied to make the process faster and more efficient but do not limit the application of the TM-method in general. The required measures to overcome them are discussed in chapter 5.

The workflow for the TM-method is shown in Fig. 2.6 and described in the following paragraphs. It is split into three main steps: The identification of the transfer matrices $\underline{\underline{H}}_{prop}$ from the time-domain aeroelastic model; Some optional post-processing steps to make the transfer matrices compatible with the airframe model; And finally, the flutter solution in the frequency domain. The steps are independent and require different tools (e.g., a time-domain rotor code for the first step). Identified transfer matrices for one propeller model (from step **1.**) can be reused in several flutter analyses even with different airframe models.

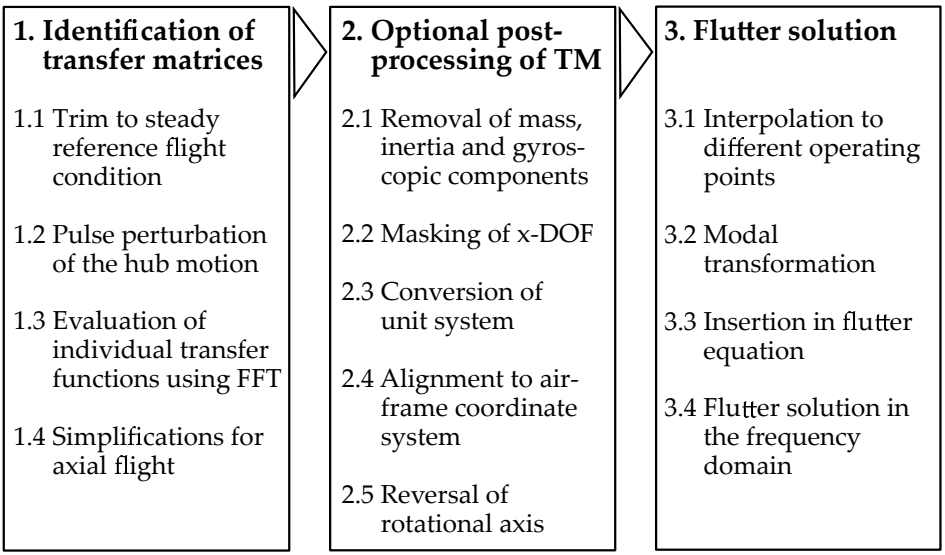

Figure 2.6.: Basic workflow of the TM-method.

The individual steps from Fig. 2.6 are explained in detail in the following workflow description:

1. **Identification of transfer matrices**
   The first major step is the identification of the frequency-domain transfer matrices $\underline{H}_{prop}(i\omega)$ from a time-domain propeller model [71]. The required steps include trim, perturbation about the trim point, derivation of the transfer functions, and assembly of the transfer matrices, including the simplifications for axial flight. The result is a set of transfer matrices $\underline{H}_{prop}(i\omega_k)$ at discrete frequencies ω_k for each operating condition.

   1.1 Trim to steady reference flight condition
   Starting with an aeroelastic time-domain propeller model, a steady reference flight condition has to be chosen, and the model must be trimmed accordingly. This requires choosing the operating conditions, usually comprising airspeed, shaft speed, and air density, at which the transfer matrices shall be identified. For these operating conditions, the time-domain propeller model has to be brought into an equilibrium state for the hub loads, e.g., using time integration or Newton iteration. Additionally, the propeller blades' collective pitch setting must be determined for variable-pitch propellers. This is usually done by pursuing a trim goal and iteratively adjusting the blade pitch to minimize the difference to the required trim goal. The trim for smaller aircraft with fixed-pitch propellers is usually carried out by adjusting the rotational speed at a fixed airspeed to meet the trim goal. Common trim goals could be a given thrust force, shaft torque, or power. It must be kept in mind that the identified transfer matrices are generally only valid for the operating conditions and trim settings chosen.

   1.2 Pulse perturbation of the hub motion
   The hub motion is perturbed in the time domain to identify the frequency response of the propeller for small perturbations about the equilibrium point found in 1.1. While Gori et al. [60] used harmonic perturbation to obtain the perturbation response for one single frequency, this method uses a broad-band excitation perturbing a whole frequency range at once. This is applicable due to the assumption of axial inflow, which makes the system time-invariant. Hence, a perturbation at a particular frequency only yields a frequency response at that frequency. Broadband excitation requires only one time integration (per hub-DOF), replacing several consecutive harmonic perturbations and saving much computational time. Eq. 2.26 defines the broad-band pulse used in this work.

$$p(t)/p_{max} =$$

$$\begin{cases} 0, & if\ \frac{t}{t_w} < 0 \\ -4(2\frac{t}{t_w}-1)^5 - 15(2\frac{t}{t_w}-1)^4 & \\ \quad -20(2\frac{t}{t_w}-1)^3 - 10(2\frac{t}{t_w}-1)^2 + 1, & if\ 0 \leq \frac{t}{t_w} < 0.5 \\ +4(2\frac{t}{t_w}-1)^5 - 15(2\frac{t}{t_w}-1)^4 & \\ \quad +20(2\frac{t}{t_w}-1)^3 - 10(2\frac{t}{t_w}-1)^2 + 1, & if\ 0.5 \leq \frac{t}{t_w} \leq 1.0 \\ 0, & if\ \frac{t}{t_w} > 1 \end{cases} \tag{2.26}$$

The top plot in Fig. 2.7 shows the resulting time history.

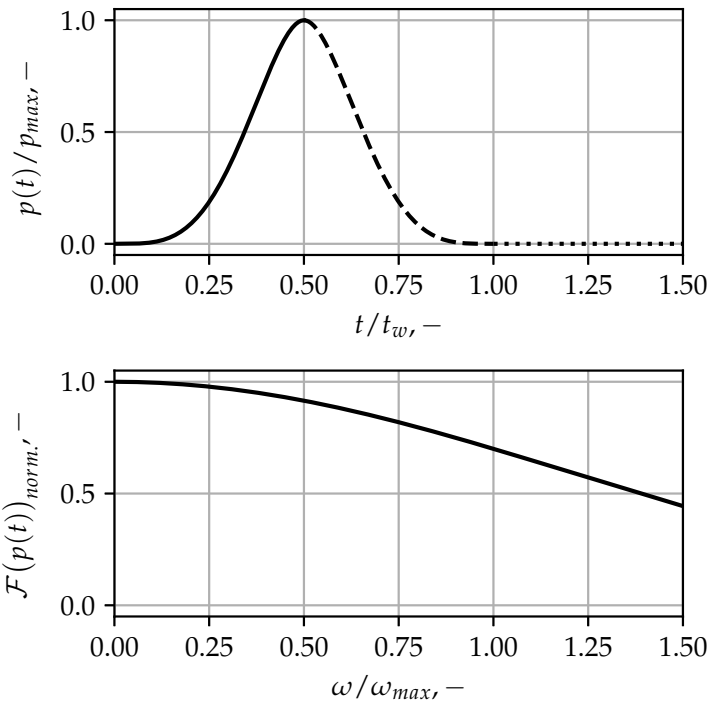

Figure 2.7.: Shape of pulse perturbation (top) and the corresponding normalized frequency spectrum (bottom).

A symmetric, fifth-order polynomial up- and down-stroke are defined using the pulse width t_w. The pulse width can be determined using the maximum frequency to be excited ($t_w = 2\pi/\omega_{max}$), although the Fourier transformation of the pulse shape in the bottom plot of Fig. 2.7 indicates that also higher frequencies are excited, but with less energy. Most importantly, Fig. 2.7 shows that all frequencies up to ω_{max} are excited, and the spectrum contains no zeros. The pulse perturbation is applied to one of the hub DOF $\boldsymbol{x}_{hub}$ (compare Eq. 2.11), e.g., the propeller disc pitch θ. The time response of the aeroelastic propeller model to the pulse itself and the following decay is obtained using time integration. The time history of the six hub load components $\boldsymbol{F}_{prop,hub}(t)$ is recorded in the non-rotating, fixed reference system[6]. The process is repeated for each DOF.

Identification using broad-band excitation only works correctly for a linear system. Generally, the time-domain propeller model can be non-linear (e.g., concerning amplitude due to geometric nonlinearities) but is assumed to show a linear behavior for small perturbations. The amplitude of the pulse perturbation has to be chosen small enough to stay within the linear regime of the model but high enough to excite the system dynamics and produce a signal significantly stronger than the numerical noise (e.g., due to integrator tolerances). To verify the usage of broad-band excitation, transfer functions obtained using the pulse shape defined in Eq. 2.26 are compared later in this thesis to transfer functions computed using harmonic perturbation. When recording the response of the hub loads in the time domain, a sufficient number of steps have to be chosen. The step size Δt is usually governed by resolving high-frequency dynamics with f_{max} in the model to avoid aliasing when transforming into the frequency domain in the next step ($\Delta t \leq \frac{1}{2f_{max}}$). The number of time steps n_{steps} determines the frequency-domain resolution Δf; a more extended time signal leads to a higher frequency resolution ($n_{steps} = \frac{1}{\Delta t \Delta f}$). Especially when distinct resonance peaks, e.g., due to elastic blade modes, are expected in the transfer functions, frequency resolution should be high enough to capture those peaks adequately.

[6] The coordinate system does not move or tilt with the propeller disc but stays fixed to the nacelle.

1.3 Evaluation of individual transfer functions using Fast Fourier Transformation

The time response of the hub loads obtained for each pulse perturbation is used to extract the frequency-domain transfer functions. First, the perturbation response is isolated by subtracting the steady-state hub loads (thrust and torque for axial flight) from the time series. Second, the time-domain data for hub motion and loads is transformed into the frequency domain using Fast Fourier Transformation. The transfer function between motion and loads is found by division, as outlined in Eq. 2.27.

$$H_{ij,prop}(i\omega) \;=\; \frac{\mathcal{F}\big(F_{i,hub}(t) - F_{i,steady}\big)}{\mathcal{F}\big(f_j(t)\big)} \tag{2.27}$$

Applying Eq. 2.27 for each DOF that was perturbed (index j) and each load component (index i) of the hub load vector $\boldsymbol{F}_{prop,hub}$ yields elements of the transfer matrices $\underline{H}_{prop}(i\omega_k)$ at distinct sampling frequencies ω_k. The transfer functions are cut at the maximum frequency ω_{max} chosen when defining the pulse shape to cut off the part of the spectrum that has not been excited with enough energy.

1.4 Simplification for axial flight

For the special case of axial flight, some assumptions can be used to reduce computational effort further. The propeller in axial flight is axially symmetric (about the global x-axis). Hence, the transfer functions to perturbations about the global z-axis can be derived from the ones about the global y-axis (or the other way round). The signs of the coupling terms between y- and z-direction are flipped according to Eq. 2.28.

$$\begin{bmatrix} F_{xz} \\ F_{yz} \\ F_{zz} \\ M_{xz} \\ M_{yz} \\ M_{zz} \end{bmatrix} = \begin{bmatrix} F_{xy} \\ -F_{zy} \\ F_{yy} \\ M_{xy} \\ -M_{zy} \\ M_{yy} \end{bmatrix} \quad , \quad \begin{bmatrix} F_{x\psi} \\ F_{y\psi} \\ F_{z\psi} \\ M_{x\psi} \\ M_{y\psi} \\ M_{z\psi} \end{bmatrix} = \begin{bmatrix} F_{x\theta} \\ -F_{z\theta} \\ F_{y\theta} \\ M_{x\theta} \\ -M_{z\theta} \\ M_{y\theta} \end{bmatrix} \tag{2.28}$$

Additionally, for the propeller in axial flight, the x-direction is uncoupled from the in-plane loads and has only a minor impact on whirl flutter stability[7].

[7] In the Houbolt/Reed theory, the terms in the x-direction are also neglected.

Especially for structural models without significant DOF in the x-direction (such as the simplified model from Fig. 1.1(b)), the x-direction can therefore be neglected by not perturbing x and ϕ, saving two additional perturbations. Considering both simplifications, the number of time-domain response simulations is cut down from six to two.

2. Optional post-processing of transfer matrices

After step **1.**, a list of transfer matrices $\underline{H}_{prop}(i\omega_k)$ and the corresponding sampling frequencies ω_k are available. These represent the linear, frequency-domain transfer behavior of the aeroelastic propeller model about the trim point. In the following step **2.**, optional post-processing steps are described to ensure compatibility with the airframe model and make the coupling process easier [76].

2.1 Removal of mass, inertia, and gyroscopic components

In case the aeroelastic propeller model contains masses (e.g., to model propeller blade dynamics), the total inertia of the model is also present in the transfer matrices $\underline{H}_{prop}(i\omega_k)$. Assuming a six-by-six mass matrix $\underline{M}_{prop}$ about the propeller hub, the influence of the inertia on the transfer matrices can be derived from Eq. 2.29[8]

$$-s^2\underline{M}_{prop} \;=\; -(i\omega)^2\underline{M}_{prop} \;=\; \omega^2\underline{M}_{prop} \tag{2.29}$$

A simplified mass matrix for the propeller with mass m_{prop} and rotational inertias J_p, J_θ and J_ψ is shown in Eq. 2.30, neglecting any mass coupling terms that could arise, e.g., from offsets between the center of gravity and the hub coordinate system.

$$\underline{M}_{prop} = \begin{bmatrix} m_{prop} & 0 & 0 & 0 & 0 & 0 \\ 0 & m_{prop} & 0 & 0 & 0 & 0 \\ 0 & 0 & m_{prop} & 0 & 0 & 0 \\ 0 & 0 & 0 & J_p & 0 & 0 \\ 0 & 0 & 0 & 0 & J_\theta & 0 \\ 0 & 0 & 0 & 0 & 0 & J_\psi \end{bmatrix} \tag{2.30}$$

In most cases, the dynamic model of the airframe already contains the mass and inertia of the propeller (e.g., to obtain correct mode shapes) in the generalized mass matrix $\underline{M}_{gen}$ (see Eq. 2.14). The mass influence on the transfer matrices is eliminated to avoid double accounting for the propeller mass. In case the aeroelastic propeller model contains a polar inertia J_p, also a gyroscopic component

[8] The mass influence is already written for the right-hand side of the flutter equation 2.14, hence the negative sign.

$\underline{G}(\Omega)$ is included in the transfer matrices (compare subsection 2.2.1). These components are also eliminated from the transfer matrices in favor of a representation as an explicit gyroscopic matrix according to section 2.2.1. The elimination is conducted by subtracting the influences from the transfer matrix samples; see Eq. 2.31.

$$\underline{\underline{H}}_{prop,mod}(i\omega_k) = \underline{\underline{H}}_{prop}(i\omega_k) - i\omega_k \underline{G}(\Omega) - \omega_k^2 \underline{\underline{M}}_{prop} \tag{2.31}$$

2.2 Masking of x-DOF

Even in case the axial DOF (x and ϕ) have been identified during the transfer matrix identification procedure using explicit perturbation, for the analysis, some or all of the transfer functions in this direction can be dropped. For example, the transfer components regarding the rotation about the global x-axis, ϕ, might not correctly represent the whole dynamics of the system if the gearbox and shafts are not modeled. Instead of including these incomplete transfer functions, they can be dropped entirely by blanking the corresponding rows and columns.

2.3 Conversion to different unit systems

The transfer matrices $\underline{\underline{H}}_{prop}(i\omega_k)$ are kept in dimensional form and are not non-dimensionalized. This prevents the impression that they can be scaled or transferred to other operating points, which is impossible due to the explicit dependency on airspeed, shaft speed, and air density. The unit systems must be kept consistent in Eq. 2.14 to ensure compatibility with the airframe model, though. The transfer matrix samples from step **1.** are in the unit system of the time-domain propeller model. The top left three-by-three sub-matrix has force per length as units, while the bottom three-by-three sub-matrix has force times length and the rest force units. Converting the unit system requires one to convert each element according to its units. A common conversion is displayed in Eq. 2.32, converting the transfer matrices from *kg-m-s* unit system into *t-mm-s* using element-wise multiplication with a unit transformation matrix:

$$\underline{H}_{prop/t,mm,s}(i\omega_k) = \underline{H}_{prop/kg,m,s}(i\omega_k) \circ \begin{bmatrix} 0.001 & 0.001 & 0.001 & 1 & 1 & 1 \\ 0.001 & 0.001 & 0.001 & 1 & 1 & 1 \\ 0.001 & 0.001 & 0.001 & 1 & 1 & 1 \\ 1 & 1 & 1 & 1000 & 1000 & 1000 \\ 1 & 1 & 1 & 1000 & 1000 & 1000 \\ 1 & 1 & 1 & 1000 & 1000 & 1000 \end{bmatrix} \tag{2.32}$$

2.4 Alignment to airframe coordinate system

Interface compatibility at the propeller hub node requires the coordinate system for the hub node in the airframe model to be aligned with the coordinate system used to identify the transfer matrices. Fig. 2.2 shows the ideal case for which both coordinate systems coincide. This might not be the case in some situations, for example, when coupling the transfer matrices obtained from one propeller model with different airframe models and coordinate systems. In this case, the reference coordinate system of the transfer matrices can be rotated afterwards to align it with the hub coordinate system. Eq. 2.33 shows the simple case of a 180° rotation about the global z-axis, in case the global x-axis in the airframe model is pointing backward instead of forward.

$$\underline{H}_{prop,mod}(i\omega_k) = \underline{H}_{prop}(i\omega_k) \circ \begin{bmatrix} 1 & 1 & -1 & 1 & 1 & -1 \\ 1 & 1 & -1 & 1 & 1 & -1 \\ -1 & -1 & 1 & -1 & -1 & 1 \\ 1 & 1 & -1 & 1 & 1 & -1 \\ 1 & 1 & -1 & 1 & 1 & -1 \\ -1 & -1 & 1 & -1 & -1 & 1 \end{bmatrix} \tag{2.33}$$

2.5 Reversal of rotational axis

In the case of modeling a propeller aircraft with several propellers, it can occur that transfer matrices for the same propeller geometry, reference coordinate system, and operating point, but reversed direction of rotation are required (e.g., if the engines on the left and right wing are counter-rotating). In this case, the transfer matrices for one direction of rotation can be derived from the other direc-

tion by switching certain signs in the transfer matrices according to Eq. 2.34[9].

$$\underline{H}_{prop,mod}(i\omega_k) = \underline{H}_{prop}(i\omega_k) \circ \begin{bmatrix} 1 & 1 & 1 & 1 & 1 & 1 \\ 1 & 1 & -1 & 1 & -1 & 1 \\ 1 & -1 & 1 & 1 & 1 & -1 \\ 1 & -1 & -1 & 1 & -1 & -1 \\ 1 & -1 & 1 & 1 & 1 & -1 \\ 1 & 1 & -1 & 1 & -1 & 1 \end{bmatrix} \tag{2.34}$$

3. Flutter solution

After the identification of the transfer matrices from the isolated propeller model in step **1.** and optional post-processing in step **2.**, the transfer matrices can be inserted into the flutter equation, and the system solved for (whirl) flutter stability [71]. While the main theory and equations are already presented in section 2.1, the process is briefly summarized in step **3.** of the process, and some details concerning the treatment of transfer matrices during flutter solution are given. The basis of step **3.** is a collection of sets of transfer matrices $\underline{H}_{prop}(i\omega_k)$ compatible with the airframe model, sampled at different operating points over the envelope (called V_m in the following).

3.1 Interpolation to different operating points

The eigenvalues of the flutter equation 2.14 are evaluated at a set of operating points V_n. A set of transfer matrices must be available at each operating point. Either the matrices are identified at each operating point ($V_n = V_m$), or the transfer matrices are identified on a smaller set of operating points V_m to save computational time and then interpolated on the larger set of operating points V_n. This is feasible for transfer matrices that gradually change with operating points and frequency. In this case, (linear) interpolation can be used between different operating points [76, 77]. In case of nonlinearities in the transfer matrices, e.g., due to propeller eigenmodes inside the frequency range of interest, care has to be taken to choose an applicable interpolation scheme.

3.2 Modal transformation

Before adding the transfer matrices to the equations of motion, which are usually in generalized form, they are transformed to modal coordinates using the relations in Eq. 2.10. The modal matrix for the

[9] This transformation has been derived from comparing transfer matrices obtained from two identical propeller models but with a reversed sense of rotation.

propeller hub node, $\underline{\Phi}_{hub}$, is obtained by partitioning the airframe modal matrix and only retaining the propeller hub node DOF.

3.3 Insertion into the flutter equation
The generalized transfer matrices can then be inserted into the flutter equation by adding them to the right-hand side (see Eq. 2.14). This is done for each operating point individually. In case the gyroscopic components of the transfer matrices have been subtracted during step **2.** or additional gyroscopic components are present, e.g., due to rotating engine parts, an additional gyroscopic matrix is added to the equations of motions according to section 2.2.1.

3.4 Flutter solution in the frequency domain
The flutter equation 2.14 is solved for the eigenvalues using one of the techniques described in section 2.1. Most of these require the transfer matrices at frequency sampling points ω_l different from those at which they have been identified (ω_k). In this case, interpolation along the frequency axis can be used to obtain the transfer matrices for the required frequency sampling points. To aid the mode tracking algorithms inside the flutter solution, it can be beneficial to avoid discontinuities in the operating conditions of the propeller. This is especially true for including gyroscopic components in the first velocity step, as their inclusion can lead to jumps in the eigenfrequencies and mode shapes, which are hard to track. Ramping the gyroscopic components up gradually via intermediate operating points to aid the mode tracking has proven to be a potential solution.

Example results from the intermediate steps described above are shown later in the result section, referring to the workflow nomenclature introduced above.

Linearization of transfer matrices

In general, the transfer matrices $\underline{H}_{prop}(i\omega)$ are nonlinear concerning frequency, e.g., due to unsteady aerodynamics or blade dynamics. In some cases, e.g., for the comparison with the Houbolt/Reed method or for compatibility with legacy, derivative-based whirl flutter workflows, it can be beneficial to describe the transfer matrices in a linear fashion similar to Eq. 2.16. For this purpose, the transfer matrices are linearized with respect to frequencies using two samples $\underline{H}_{prop}(i\omega_k)$ [75, 77]. One sample is chosen at zero frequency to capture the correct quasi-steady transfer function ($\omega_0 = 0$). The second sample is chosen close to the expected whirl flutter frequency (ω_1). Eq. 2.35 shows the linearization into a stiffness and damping matrix using the two transfer matrix samples. The resulting matrices $\tilde{\underline{K}}_{prop}$ and $\tilde{\underline{D}}_{prop}$ are still dimensional and have to be non-dimensionalized according to Eq. 2.16 to obtain their non-dimensional

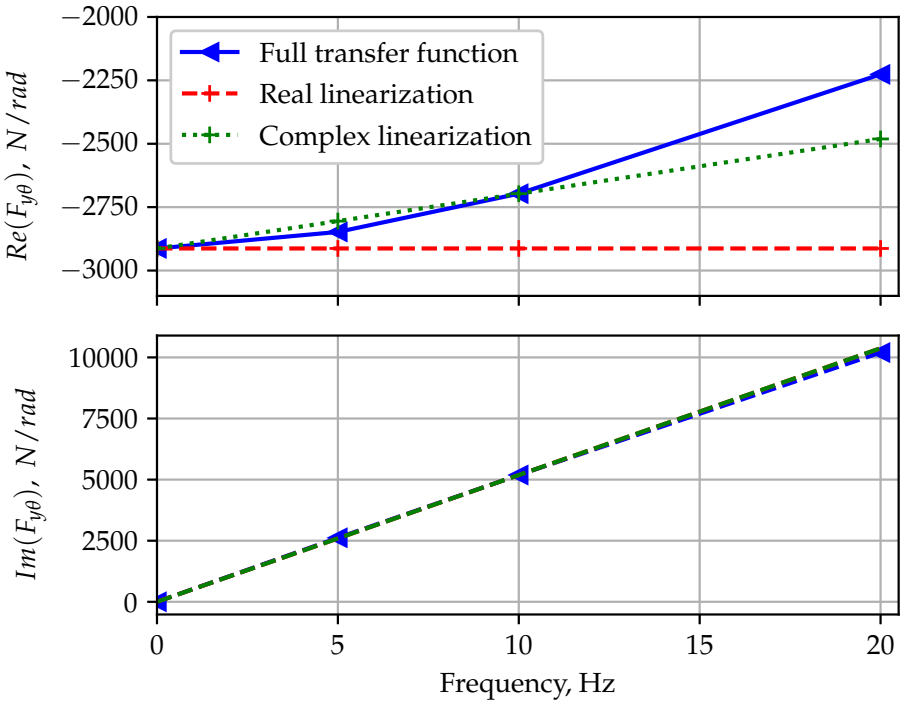

Figure 2.8.: Comparison of full, frequency-dependent transfer function with real and complex linearization.

counterparts. From the non-dimensionalized matrices, derivatives compatible with the Houbolt/Reed method can be obtained.

$$\underline{H}_{prop,lin}(i\omega) = \underbrace{\underline{H}_{prop}(0)}_{\tilde{\underline{K}}_{prop}} + \underbrace{\frac{\underline{H}_{prop}(i\omega_1) - \underline{H}_{prop}(0)}{i\omega_1}}_{\tilde{\underline{D}}_{prop}} i\omega \tag{2.35}$$

Because, in most cases, $\underline{H}_{prop}(i\omega_1)$ is complex with both a non-zero real and imaginary part, the resulting damping matrix, $\tilde{\underline{D}}_{prop}$, is complex-valued. This is technically incompatible with the Houbolt/Reed method, which provides a real-valued damping matrix. To ensure compatibility, the imaginary part of the damping matrix can be dropped, or it is retained to obtain a better representation of the transfer matrices. Fig. 2.8 compares the real and complex linearization of an example transfer function for $F_{y\theta}$, split into real and imaginary

parts of the resulting transfer function. The slope of the imaginary part (damping) fits for all three descriptions, as this part of the transfer function is linear in this case. The nonlinearity of the total, frequency-dependent transfer function is mainly in the real part, where the complex linearization gives a better approximation than the real linearization. The latter only captures the zero-frequency component correctly. From the real part, it can be seen that the approximation by linearization becomes worse if the actual transfer function is more nonlinear.

2.3. Propeller modeling

Section 2.1 and 2.2 describe the theory for (whirl) flutter analysis in the frequency domain. In subsection 2.2.3, a new method is described to obtain a frequency-domain ROM from a time-domain propeller model. This section briefly overviews some methodological aspects of these time-domain propeller models, mainly covering the methods used within this thesis. First, the low- to mid-fidelity aerodynamic methods applied in this thesis are described and compared. Second, the structural modeling of elastic propeller blades within MBS is covered. It is acknowledged that the full extent of available theory in the field of rotor or propeller modeling is not encompassed. Nevertheless, the chosen scope is deemed sufficient for this thesis.

2.3.1. Aerodynamic methods

The motion-induced aerodynamics of the propeller are the driving factor for propeller whirl flutter, so an aerodynamic method is required for whirl flutter analysis. While the classical Houbolt/Reed method introduced earlier directly derives the motion-induced load components in the frequency-domain [5, sec. 5.4], the TM-method uses the time history of the propeller loads in response to a perturbation in hub motion. Therefore, the aerodynamic method used for this purpose should be able to compute the aerodynamic loads due to unsteady hub motion in the time domain. Three classes of methods are standard in literature:

- **Low-fidelity methods:** analytical methods usually based on strip theory with local airfoil polars for the blade aerodynamics
- **Mid-fidelity methods:** potential flow solvers modeling blade and wake aerodynamics and hence explicitly modeling the interaction
- **High-fidelity methods:** Navier-Stokes based CFD with explicit modeling of the whole flow field, including turbulence and compressibility

Only low- to mid-fidelity methods are considered in this thesis, which focuses on the TM-method. The specific methods used within these categories are explained below. They represent a subset of the methods used in an earlier publication [75].

Low-fidelity methods

The low-fidelity methods used in this thesis discretize the propeller blade into several radially independent airfoil sections with constant properties. The flow field and, therefore, aerodynamic loads are evaluated at each strip individually. Each strip has an associated chord length c, a radial position r, and an extension in radial direction dr as shown in Fig. 2.9. The flow characteristics are evaluated at the aerodynamic collocation point at the three-quarter chord line ($3/4c$) by forming the (vector) sum of all relevant velocity components. These comprise the kinematic relations of the rotating propeller blade (airspeed V and rotation Ωr), velocities due to hub or elastic blade motion (in-plane $\dot{y}$ and out-of-plane $\dot{x}$), and induced velocities V_{ind} from the wake. From the vector sum, the kinematic angle of attack α_{kin} and total velocity V_{eff} are found according to Fig. 2.9.

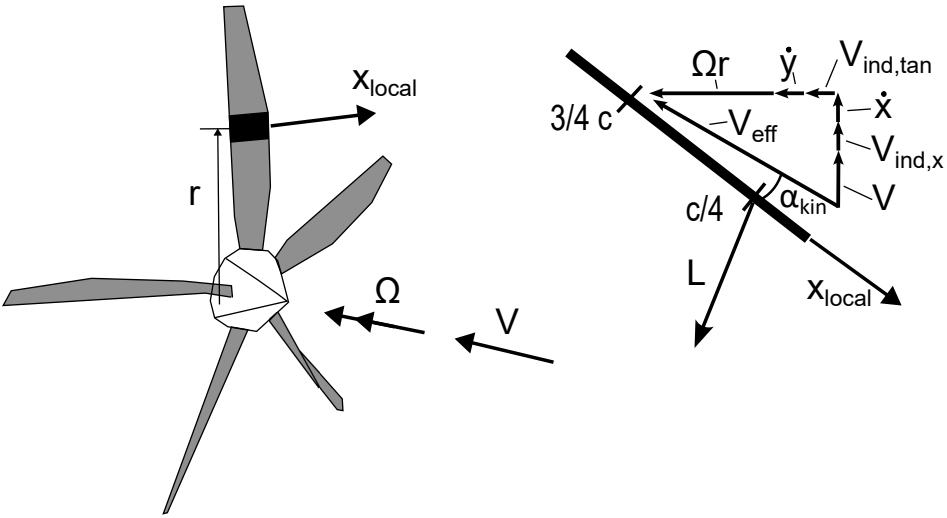

Figure 2.9.: Velocity triangle (right) for a strip of the propeller blade (left).

The local lift L can be calculated from these quantities using the strip area $c\ dr$ and the airfoil lift polar $C_l(\alpha)$ as shown in Eq. 2.36. Drag and moment are obtained similarly.

$$L = \frac{\rho}{2} V_{eff}^2\ c\ dr\ C_l(\alpha_{kin}\ \Gamma(t)) \tag{2.36}$$

When evaluating the airfoil polar with the kinematic angle of attack, time-constants $\Gamma(t)$ modeling the unsteady lift-lag effect can be applied to obtain the aerodynamic angle of attack. Wagner developed one formulation for the lift-lag effect [78], and it was approximated by R.T. Jones [78] into two time-constants (see Γ_{Wagner} in Eq. 2.37). Neglecting these time-constants (see $\Gamma_{QS} = 1$ in Eq. 2.37) yields the quasi-steady formulation of the strip theory and lift follows the instantaneous angle of attack. Wagner's airloads model includes more (non-circulatory) unsteady lift components [79], which are neglected here.

$$\begin{aligned} \Gamma_{QS}(t) &= 1 \\ \Gamma_{Wagner}(t) &= 1 \; - \; 0.165e^{-0.0455\frac{2tV_{eff}}{c}} \; - \; 0.335e^{-0.300\frac{2tV_{eff}}{c}} \end{aligned} \tag{2.37}$$

The loads are applied to the local quarter chord point $c/4$. Repeating this process for all blades and strips in each time step yields the blade load distribution and, by integration at the hub point, the hub load time history.

Circulatory lift on the blade leads to a shedding of vorticity into the wake behind the propeller. The combined wake sheets from all blades induce a velocity field back on the propeller disc (see V_{ind} in Eq. 2.36), affecting the lift distribution via the local angle of attack. These induced velocities[10] can either be neglected (yielding the quasi-steady or unsteady strip theory described above) or modeled on the equation level. Many analytical models for computing the induced-velocity distribution on the propeller disc are available in the literature, ranging from steady uniform inflow models over quasi-steady blade element momentum (BEM) theory to unsteady dynamic inflow models [80]. This thesis applies the quasi-steady BEM based on a momentum equilibrium between lift and induced velocity at radially independent stream tubes (or strips) [81]. Thrust is balanced by an increase in axial-induced velocity and moment (or, better, tangential force) by the rise in tangential-induced velocity. Because the induced velocities change the force distribution which cause them, an equilibrium between the two has to be found in each time step by iteration[11]. The usual formulation of the BEM obtains the equilibrium for all strips on a radial ring by averaging the azimuthal lift distribution. According to Smith [25], this does not represent the reality for situations with a varying lift distribution along the azimuth, such as a propeller operating under an angle of attack (or disc pitch). He suggests a formulation that blends the original ring-wise formulation with an element-wise

[10] The term "induced velocities" is used in this thesis do describe the velocities induced on the propeller disc due to the combined wake sheets behind the rotor. The term "inflow" in the same context describes the sum of external velocity and induced velocity [25, Chapter 1.1.1].

[11] Contributions to the induced velocities by the near-wake are included in the Wagner-function and not considered in the BEM, which only covers the combined effect of the propeller wake.

BEM, for which the equilibrium is found at each blade and strip individually. At the blade root, his averaged momentum theory (AMT) applies the ring-wise solution, and at the blade tip, the element-wise formulation is applied. The two solutions are blended linearly at intermediate radii based on the radius. Because the lift and inflow are computed for radially independent strips, no tip-loss effects are contained in the theory from the first principle. The loss of lift at the blade tip due to the impact of the tip vortex [80] is modeled with an empirical tip-loss factor instead. In the case of the implementation used in this thesis, a Prandtl-Glauert tip-loss factor is used [81].

Mid-fidelity methods

While in the low-fidelity methods, the blade and wake aerodynamics are handled by separate analytical models, the mid-fidelity methods lift the assumptions connected to this separation. Usually, based on the potential equation, the interaction of blade and wake aerodynamics is modeled explicitly. In this paper, the unsteady panel method (or UPM) [82, 83, 84] developed by the DLR Institute of Aerodynamics and Flow Technology, is employed. UPM is a velocity-based potential flow solver. Lifting surfaces such as propeller blades are discretized into a vortex lattice grid on the mid-surface and a source-sink panel distribution on the outer airfoil shape to capture thickness effects. The chordwise distribution of circulation is prescribed[12] and its total value is determined by fulfilling the (unsteady) Kutta-condition on the trailing-edge Kutta-panel by iteration in each time step. A full-span free wake is shed from the Kutta panel at the trailing edge, and the induced velocities between the blade and wake elements are considered when solving for the pressure distribution on the blade surface and the wake velocities. UPM computes the section loads internally for each radial strip from the pressure distribution, which can then be integrated into hub loads for usage in the TM-method. While in the scope of this thesis, UPM is only used standalone with prescribed hub motion, it could also be coupled to an elastic blade model, e.g., in MBS.

Comparison

The aerodynamic methods described above and used within this thesis are compared in Tab. 2.2. Each row gives information about the specific method of blade lift, the wake and tip-loss model used, and an order of magnitude for the expected computational times. The methods are ordered by descending computational time and fidelity. UPM, as a mid-fidelity method, features a 3D blade lift model, while the other methods all use a strip-theory approach for the blade lift, which in the case of the Houbolt/Reed methods is even linearized and only uses the blade lift curve slope.

[12] In case of this thesis, proportional to the airfoil thickness.

Table 2.2.: Comparison of aerodynamic methods used in this thesis (reproduced from [75]).

Method	Blade Lift	Wake	Tip Loss	Comp. time
UPM [82, 83, 84]	2D vortex lattice on camber surface + 3D source/sink panels on blade surface	Free panel wake	Included in free wake	hours
BEM+Wagner	Strip theory using airfoil polars + Wagner's function for unsteady lift lag [79]	Weighted blade element momentum theory [81, 25]	Prandtl–Glauert	minutes
Wagner	Strip theory using airfoil polars + Wagner's function for unsteady lift lag [79]	No induced velocity model	No tip loss model	seconds
Quasi-steady	Strip theory using airfoil polars	No induced velocity model	No tip loss model	seconds
Houbolt/Reed	Linearized strip theory ($C_{l\alpha}$ only) + Theodorsen's function for unsteady lift lag	No induced velocity model	Aspect ratio correction	seconds
Houbolt/Reed quasi-steady	Linearized strip theory ($C_{l\alpha}$ only)	No induced velocity model	Aspect ratio correction	seconds

Only UPM and BEM+Wagner include an induced-velocity model, with the first employing a free-wake model and the latter the quasi-steady weighted momentum theory. Regarding tip loss models, only UPM included this from the first principle due to the free wake and 3D lift model; all other methods either include it empirically or not. The different models and their effect on unsteady propeller aerodynamics and whirl flutter predictions are compared later in section 4.3.

2.3.2. Structural modeling with MBS

For modeling the propeller structure and kinematics of the rotating system, multi-body simulation (MBS) is used in this thesis. A MBS system consists of an arbitrary number of individual bodies connected by joints that allow for nonlinear motion between the body. For the example of the rotating propeller, each blade could be modeled as a separate body. Each blade is connected with a fixed joint to the rotating propeller hub body, which in turn is connected to the non-rotating nacelle via a joint with forced rotation about the shaft axis. Eq. 2.38 shows the equations of motion for such a nonlinear system [85], split into the kinematic equations (first row), the momentum equations (second row), and the dynamic state equations (third row)[85]. Constraints and algebraic states are neglected as they are irrelevant to this paper.

$$\begin{aligned} \dot{\boldsymbol{p}} &= \underline{T}(\boldsymbol{p})\boldsymbol{v} \\ \underline{M}(\boldsymbol{p})\dot{\boldsymbol{v}} &= \boldsymbol{f}(\boldsymbol{p}, \boldsymbol{v}, \boldsymbol{a}, t, \boldsymbol{w}) \\ \dot{\boldsymbol{a}} &= \boldsymbol{f}_c(\boldsymbol{p}, \boldsymbol{v}, \boldsymbol{a}, t, \boldsymbol{w}) \end{aligned} \tag{2.38}$$

The differential equations are written in terms of position states $\boldsymbol{p}$, their derivatives in the form of the velocity states $\boldsymbol{v}$ and additional force element states, e.g., for unsteady aerodynamics, $\boldsymbol{a}$. The first set of equations relates the position and velocity states with a transformation matrix for the angles, $\underline{T}$. The second set contains the momentum equilibrium and is written in terms of forces and moments, with the inertial contributions from the system mass matrix $\underline{M}$ on the left side and the balancing internal loads, e.g., from elastic contributions, as a nonlinear set of equations $\boldsymbol{f}(\boldsymbol{...})$ on the right-hand side. The third set of equations contains the internal dynamics of the force elements, for example, the dynamic equations from the Wagner equations for the aerodynamic lift-lag effect, compare Eq. 2.37. All equations are time-dependent on the system time t and can contain external inputs $\boldsymbol{w}$, for example, from forced motion.

From these equations, the state vector $\boldsymbol{x}$ can be assembled from the position, force, and velocity states as shown in Eq. 2.39.

$$\boldsymbol{x} = \begin{bmatrix} \boldsymbol{p} \\ \boldsymbol{a} \\ \boldsymbol{v} \end{bmatrix} \tag{2.39}$$

The position states $\boldsymbol{p}$ (and therefore also the respective velocity states) comprise the states connected to the position of the joints connecting the bodies $\boldsymbol{p}_{joint}$, in case they have any DOF associated. One example is the flapping hinge of a helicopter blade, which could be modeled with a rotational hinge with one position state (the angular position). Further position states stem from the flexible deformation of the elastic bodies, $\boldsymbol{p}_{flex}$.

$$\boldsymbol{p} = \begin{bmatrix} \boldsymbol{p}_{joints} \\ \boldsymbol{p}_{flex} \end{bmatrix} \tag{2.40}$$

The flexible deformation of, e.g., an elastic blade, is described in Simpack as a relative deformation with respect to the body reference marker, e.g., at the blade root. The rigid body motion of the body reference marker is described using the nonlinear joints. Additional flexible deformation $\boldsymbol{z}(\boldsymbol{r}, t)$ is written in modal coordinates with the mode shapes of the body $\boldsymbol{\Phi}_i$ for the spatial dependency and the flexible position states $p_{flex,i}$ for the temporal dependency. The mode shapes are given for positions along the body coordinates $\boldsymbol{r}$ and are either imported or computed internally. For more details about the formalism of including flexible bodies into the Simpack MBS, the reader is referred to Wallrapp [86, 87, 88].

$$\boldsymbol{z}(\boldsymbol{r}, t) = \sum_{i=0}^{n_{modes}} \boldsymbol{\Phi}_i(\boldsymbol{r}) p_{flex,i}(t) \tag{2.41}$$

The nonlinear equations of motions from 2.38 are integrated in time using nonlinear time integration. The integrator chosen in Simpack for this task is called SODASRT2 [85] and is a backward-differentiation-formula (BDF) integrator based on the DASRT solver [89]. In the first simulation part, the solution for the system states $\boldsymbol{x}(t)$ is obtained by time integration. All intermediate results, such as applied loads from aerodynamics, joint loads, or flexible body deformations, are obtained in a second postprocessing part by re-inserting the solution for the states into the respective equations (compare, e.g., Eq. 2.36 and 2.37). The hub forces used for the TM-method are extracted from the final solution using the joint forces for the non-rotating hub marker.

2.4. Time-domain stability analysis

Besides the frequency-domain approach to whirl flutter analysis described in section 2.1 and 2.2, other approaches exist in literature to evaluate the coupled aeroelastic stability of a rotor-airframe system. One, used in this thesis as a reference method for verifying the frequency-domain approach, is based on perturbations of the coupled system in the time domain. This stability analysis requires a simulation model of the complete aeroelastic system in the time domain. For example, the rotating propeller and the simplified pylon are modeled together in one MBS model to evaluate the coupled aeroelastic system response to perturbations. The specific method used in this thesis to extract frequency and damping information from the response of a coupled, aeroelastic time-domain model is the Floquet analysis [90]. The theory is outlined here based on the existing literature to highlight the assumptions associated with it before the results are used as a reference for the verification of the TM-method.

Assume a linear, time-periodic system with period T as written in Eq. 2.42. In the cases studied in this thesis, T describes one rotation of the rotor or propeller. Only the homogeneous part of the system is shown, and the system matrix $\underline{A}$ is periodic. $\boldsymbol{x}$ is the state vector consisting of the n states of the system.

$$\dot{\boldsymbol{x}} = \underline{A}(t)\boldsymbol{x}(t) \quad ; \quad \underline{A}(t+T) = \underline{A}(t) \tag{2.42}$$

We call $\boldsymbol{\phi}_i$ fundamental solutions of the system (with i from $[1, n]$) if they consist of its response to a small initial perturbation integrated over one period. The collection of n fundamental solutions with linear independent initial conditions is called fundamental matrices $\underline{\phi}$, compare Eq. 2.43.

$$\dot{\boldsymbol{\phi}}_n(t) = \underline{A}(t)\boldsymbol{\phi}_n(t) \; ; \; \underline{\phi}(t) = [\boldsymbol{\phi}_1(t)...\boldsymbol{\phi}_n(t)] \tag{2.43}$$

The matrix that projects the fundamental matrix at the beginning of the period $\underline{\phi}(0)$ to the fundamental matrix at the end of the period $\underline{\phi}(T)$ is called monodromy matrix, compare $\underline{C}$ in Eq. 2.44

$$\underline{\phi}(T) = \underline{\phi}(0)\underline{C} \tag{2.44}$$

According to Floquet theory [91], fundamental matrices of linear time-periodic systems can be decomposed in a time-periodic part $\underline{P}$ and a matrix exponential $e^{\underline{R}t}$:

$$\underline{\phi}(t) = \underline{P}(t)e^{\underline{R}t} \; , \; \underline{P}(t+T) = \underline{P}(t) \tag{2.45}$$

This yields [91] the relation between the monodromy matrix and the matrix exponential $\underline{R}$

$$\underline{C} = e^{\underline{R}T} \tag{2.46}$$

The eigenvalues of the monodromy matrix are called characteristic multipliers ρ_k. For stability, all ρ_k must fall inside the unit circle in the complex plane ($|\rho_k| < 1$) to prevent any perturbations from increasing (compare Eq. 2.44). The eigenvalues of $\underline{R}$, on the other hand, are called characteristic exponents λ_k and contain the frequency (imaginary part) and damping (real part) of the system eigenvalues, compare Eq. 2.47.

$$\omega_{nk} = |\lambda_k| \; ; \; \zeta_k = -\frac{\mathrm{Re}(\lambda_k)}{\omega_{nk}} \tag{2.47}$$

The characteristic exponents are related to the characteristic multipliers by an exponential $\rho_k = e^{\lambda_k T}$. An essential consequence of this relation is that the imaginary part of the characteristic exponents and hence the frequencies are not uniquely determined, as adding an integer multiplier j_k of the rotation frequency $2\pi/T$ is also a valid solution, compare Eq. 2.48

$$\lambda_k = \frac{1}{T}\ln(\rho_k) + i\frac{1}{T}(arg(\rho_k) + j_k 2\pi) = \sigma_k + i\omega_k \tag{2.48}$$

As Peters and Lieb [92] pointed out, there is no correct choice of the integer multiplier and, therefore, frequency. Specific choices are more helpful for comparison with other methods and a more straightforward interpretation. In the case of this thesis, an approach based on the periodic eigenvectors of the systems is chosen [93] to pick a suitable j_k and to fix the main frequency value[13]

The periodic eigenvectors are computed from the fundamental matrices and the eigenvectors of $\underline{R}$. The eigenvectors $\underline{V}$ of $\underline{R}$ can be used to diagonalize $\underline{R}$, as shown in Eq. 2.49.

$$\boldsymbol{R} = \boldsymbol{V} diag(\lambda_k) \boldsymbol{V}^{-1} \tag{2.49}$$

The periodic eigenvectors $\boldsymbol{u}_k$ associated with a characteristic exponent λ_k are computed as shown in Eq. 2.50 (with $\boldsymbol{v}_k$ being the columns of $\boldsymbol{V}$). Note that through the dependency of λ_k on the integer multiplier, the periodic eigenvectors

[13] Periodic systems have multi-harmonic eigenvalues and therefore not only one single frequency.

also depend on the choice of j_k. As Peters and Lieb [92] note, the combination of the periodic eigenvector and the characteristic multiplier is always unique.

$$\boldsymbol{u}_k(t) = \underline{\phi}(t)\boldsymbol{v}_k e^{-\lambda_k t} \tag{2.50}$$

By analyzing the frequency contribution to the periodic eigenvectors (e.g., by applying an FFT to $\boldsymbol{u}_k$), the harmonics (and therefore integer multiplier j_k) with the highest participation in the system response can be identified, giving a good choice for the integer multiplier.

In practical applications, e.g., when handling MBS models, the system is usually not linear time-periodic as in Eq. 2.42. In the case of Simpack models, for example, the system equations are inherently non-linear due to the non-linear nature of the MBS setup, see Eq. 2.38. The goal is to assess the system stability for small perturbations about an equilibrium $\boldsymbol{x}_0(t)$. The deflections during this periodic steady state may be entering the non-linear range. Still, system is assumed to be linear for small perturbations around this periodic steady state. The fundamental matrices $\boldsymbol{\phi}_k$ are computed by adding a small perturbation at state k to the initial condition $\boldsymbol{x}_0(t=0)$, using the non-linear time integration to obtain the system response $\boldsymbol{x}(t)$, and subtracting the steady state $\boldsymbol{x}_0(t)$ afterward, as Eq. 2.51 shows.

$$\boldsymbol{\phi}_k(t) = \boldsymbol{x}(t) - \boldsymbol{x}_0(t) \tag{2.51}$$

Multi-Blade Coordinates

Subsection 2.3.2 in this chapter describes the formalism of the MBS-system Simpack used within this thesis. Simpack formulates the equations of motion in relative coordinates, so the DOFs of each body are formulated relative to its reference coordinate system, which can be a moving frame. For example, consider the case of a rotor with elastic blades. The elastic blade equations are formulated relative to the blade reference frame at the hub, which is rotating with respect to the inertial reference frame. This formulation in relative coordinates poses two issues for analyzing phenomena in which the rotor couples as a whole entity with an underlying, non-rotating airframe. First, as the blades rotate, they experience harmonic oscillations in the support stiffness, as they rotate relative to the non-rotating airframe-DOF[14]. This makes the equations of motion periodic, even for cases in which the system is time-invariant. Second, the individual blade DOFs appear in the system's eigenvectors. This can be useful in some cases, but in most cases, it is easier to interpret the motion of

[14] Only in the particular case of an isotropic airframe the harmonic part in the blade equations vanish.

the whole rotor disc as one unit (e.g., to identify a coning mode or a whirl mode due to blade bending) as the entire rotor couples with the airframe.

To solve these two issues, the multi-blade coordinate (MBC) transformation [94] is applied to the state vector $\boldsymbol{x}$. The MBC transformation projects the individual blade-DOF into the non-rotating system and transforms the individual blade modes into global rotor modes. The transformation is based on summation over all N_b blades, weighted with the respective blade azimuth Ψ_b, compare Eq. 2.52 [94].

$$\begin{aligned} x_{col} &= \frac{1}{N_b}\sum_{b=1}^{N_b} x_b \\ x_{cos,n} &= \frac{2}{N_b}\sum_{b=1}^{N_b} x_b \cos(n\Psi_b) \\ x_{sin,n} &= \frac{2}{N_b}\sum_{b=1}^{N_b} x_b \sin(n\Psi_b) \\ x_{diff} &= \frac{1}{N_b}\sum_{b=1}^{N_b} x_b(-1)^b \end{aligned} \tag{2.52}$$

The sketch in Fig. 2.10 shows two sets of lead-lag modes for a four-bladed rotor: The top row shows individual blade modes (x_b in Eq. 2.52), where only one blade is oscillating in each mode. The bottom row shows global rotor modes obtained by MBC-transformation. The left mode is called collective mode x_{col}, and all blades oscillate in phase. The second mode is the first cosine-cyclic mode $x_{cos,1}$, while the third mode represents the first sine-cyclic mode $x_{sin,1}$. Here, the blades oscillate with a 180°phase shift in each mode. The two cyclice modes have an additional phase shift of 90°towards each other. A rotor with five blades or more shows cyclic modes of second order, where the blades oscillate with a 45°phase. A rotor with an even number of blades also shows a differential mode x_{diff}, in which the blades oscillate with 90°phase, as it is shown in the last sketch on the bottom left of Fig. 2.10.

For coupling between the rotor and the airframe, especially the first three rotor modes are essential, as they create effective loads about the hub [34]. In the example of lead-lag modes in Fig. 2.10, the collective mode creates a moment about the rotor axis due to, e.g., inertial loads. The first cyclic modes create lateral forces about the rotor hub. The differential mode and all higher cyclic modes are called reaction-less because the effective loads about the rotor hub

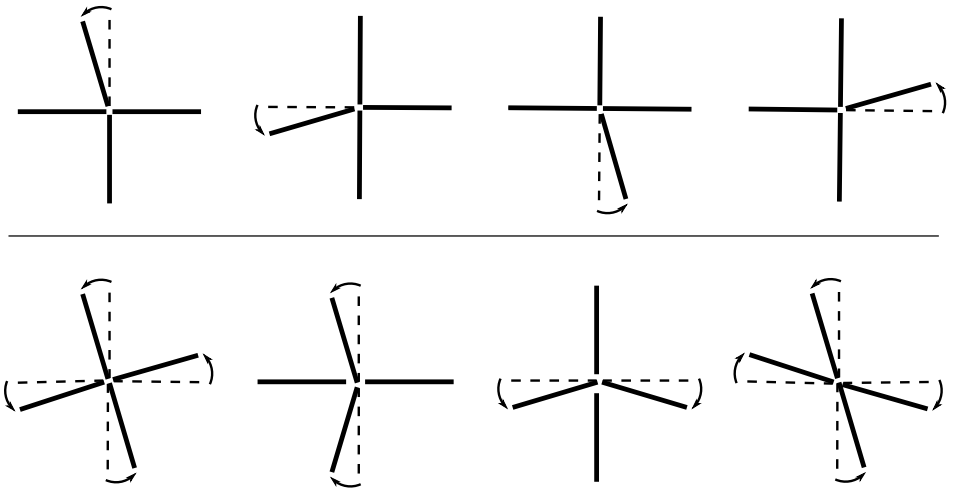

Figure 2.10.: Set of four individual blade modes and the corresponding global rotor modes for a four-blades rotor with lead-lag DOF.

are zero. Therefore, they do not couple with the airframe. Under rotation, the first-order cyclic modes couple with each other due to gyroscopics and create the progressive and regressive cyclic modes, equivalent to the forward and backward whirl modes of global airframe modes.

The MBC transformation is applied in this thesis to the state vectors in the fundamental matrices in Eq. 2.51 to reduce periodicity and obtain the results of the Floquet analysis afterwards in the non-rotating frame, including global rotor modes.

Treatment of aerodynamic states during a Floquet analysis

To apply the Floquet theory to a coupled MBS system, the time history of the complete state vector $\boldsymbol{x}(t)$ needs to be computed and analyzed. This includes the states representing the unsteady aerodynamics, compare $\boldsymbol{a}$ in Eq. 2.38. Neglecting parts of the state vector can otherwise lead to wrong results, especially in the damping forecast (compare Peters and Sue [95]). Additionally, the MBC transformation is applied in this paper to transform elastic blade states into global rotor modes. This ensures all system modes are based on the non-rotating coordinate system and are comparable to the results obtained with the TM-method. This leads to a problem in conjunction with the presence of the aerodynamic states: Technically, the aerodynamic states are in the rotating blade frame, but the application of the MBC transformation on

the aerodynamic states does not give meaningful results. Hence, three analysis cases occur in this thesis:

1. **Unsteady aerodynamics, but no elastic blade modes:**
   No MBC transformation is required, as no structural states occur in the rotating frame. The Floquet analysis can be applied to the full state vector, including unsteady aerodynamics, but only the results for the structural states are shown.

2. **Unsteady aerodynamics and elastic blade modes:**
   The presence of elastic blade modes requires the MBC transformation to compare the results with the TM-method's results. Therefore, the aerodynamic states are omitted when computing the fundamental matrices, which leads to (small) inaccuracies in the damping prediction.

3. **Quasi-steady aerodynamics and elastic blade modes:**
   Due to the Quasi-steady aerodynamics, no aerodynamic states are present in the model, and the full state vector can be transformed into the non-rotating frame. The Floquet results are exact in this case.

To assess the potential impact on the damping prediction, App. A.3 gives a comparison of frequency and damping results obtained with rigid blades and with and without including the aerodynamic states in the Floquet analysis. The observed differences are small but visible. Hence, for verifying the TM-method with elastic blades in chapter 4, both cases 2. and 3. are used to make sure the inaccuracy in the damping prediction due to the omission of aerodynamic states does not affect the verification.

3 Models

The models to apply and verify the Transfer-Matrix method in this thesis are introduced in this chapter. The propeller blade geometry, as well as the structural and aerodynamic modeling data, are introduced first. The two airframe models are explained in the second part, comprising a simplified pylon system with two DOFs and a generic, two-engine, free-flying commuter aircraft.

3.1. Propeller model

First, this chapter introduces the propeller model used for all studies. The geometry is close to a commercial off-the-shelf regional turboprop propeller but kept generic. The structural model is based on engineering constants derived from the outer shape and material constants for wooden laminate. The aerodynamic properties of the blade are also listed, assuming simplified airfoil data. The propeller geometry was used in previous publications [73, 74, 75].

3.1.1. Geometry

The propeller used in this thesis resembles a five-bladed, variable-pitch propeller with a 1.25m radius. The blade sections start at 18% radius. Everything inside is covered by the spinner and not modeled. The chord and twist distribution can be found in Fig. 3.1. Due to the variable-pitch mechanism, a variable root pitch angle can be added to the twist distribution to trim the propeller to a given thrust or power setting. The direction of rotation of the propeller is clockwise, looking from the front.

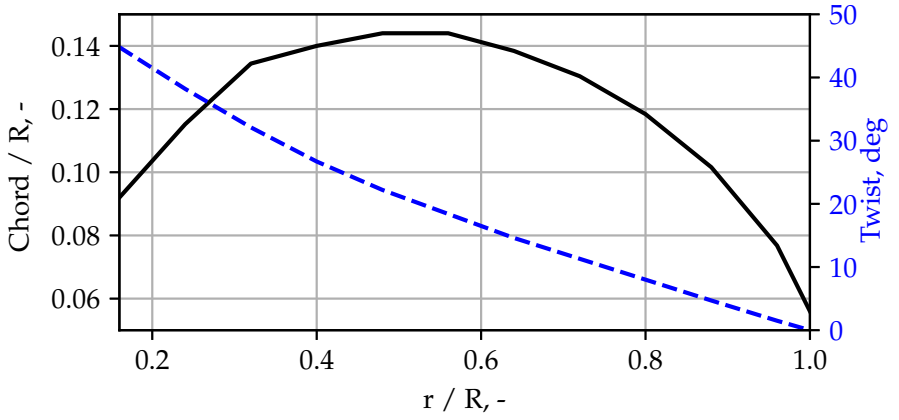

Figure 3.1.: Propeller blade chord and twist distribution (reproduced from [75]))

3.1.2. Structural dynamics

The propeller blade's structure is assumed to be made entirely from wooden composite with a steel leading edge protection on the outer 40% of the radius. Due to its long, slender shape, a modeling approach with beam elements is chosen for the blade structure. The blade structural model does not resemble an existing propeller blade but is generic for this study. The general layout is kept close to off-the-shelf wooden propeller blades to ensure realistic orders of magnitudes.

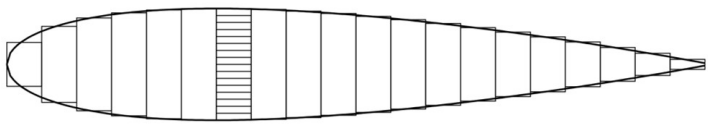

Figure 3.2.: Generic propeller airfoil section, discretized into rectangles to obtain engineering constants.

The engineering constants of the individual blade sections are derived numerically by discretizing the airfoil section (assumed as a symmetrical, four-digit NACA airfoil) into small rectangles (compare Fig. 3.2) and numeric integration to obtain the different engineering constants in the local reference frame (aligned with the blade chord). Eq. 3.1 gives an example for the numerical derivation of the tensile stiffness EA from the Young's modulus of the individual rectangle E_{rect} and its respective area A_{rect}.

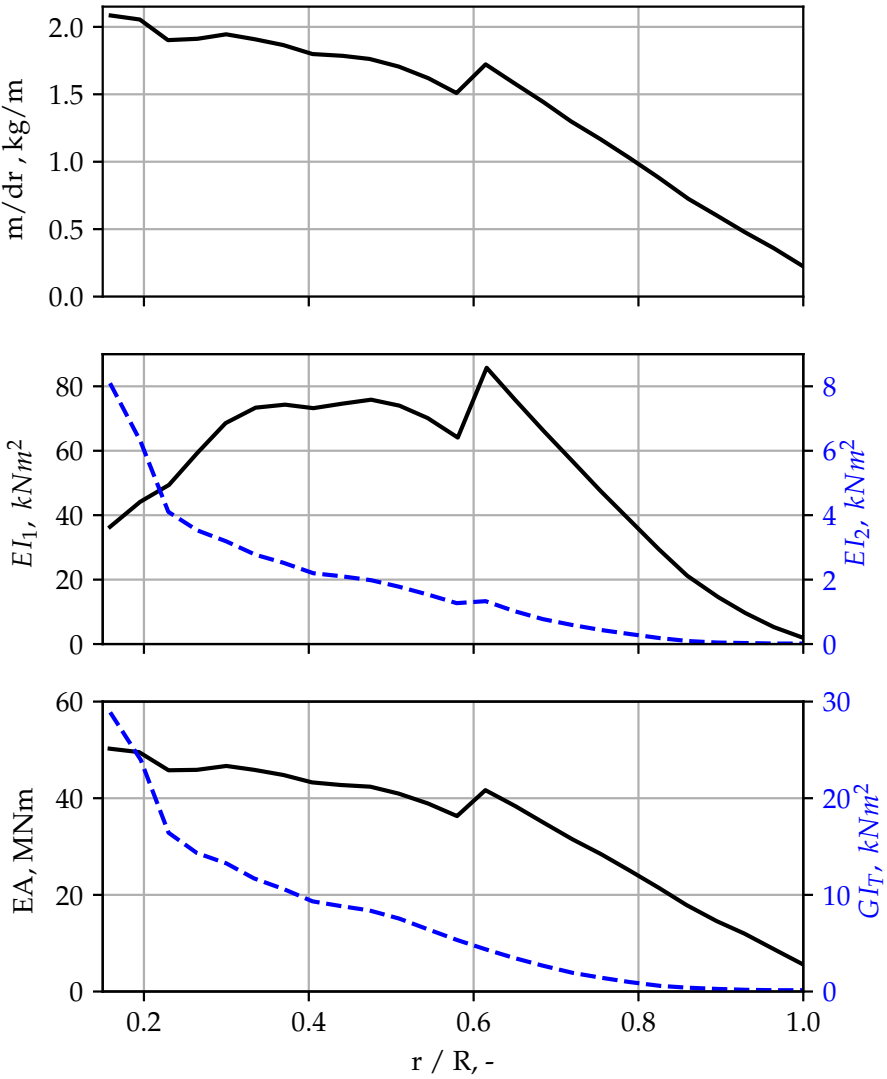

Figure 3.3.: Propeller blade stiffness and mass distribution

$$EA = \sum_{0}^{n_{rects}} E_{rect} A_{rect} \tag{3.1}$$

Fig. 3.3 shows the resulting mass and stiffness distribution for the blade. The top plot shows the mass per unit length. The total mass of one blade adds up to 1.542 kg, and the blade has a mass moment of inertia about the rotational axis of 0.395 kgm^2. The middle plot shows the two respective bending stiffness distributions about the axis vertical to the chord (EI_1) and the chord axis (EI_2). The bottom plot gives the tensile and torsional stiffness. The jump in the structural properties at 60% radius is due to the steel leading edge protection, which covers the outer 40% and leads to a local increase in stiffness and mass.

The structural model is built up using the Finite-Element-Method (FEM) using Timoshenko beam elements with constant properties over one individual element. Twenty-five elements are used, although the innermost element covers the connection between zero and 18% radius and is assumed to be rigid. The internal FEM-library SIMBEAM of the MBS-code Simpack [85] is used for modeling the blade, and the stiffness values are input in the local coordinate system aligned with the blade chord at the respective blade sections. SIMBEAM internally performs a modal analysis of the model followed by a modal reduction, including the respective geometric stiffness terms for considering geometric stiffening under rotational speed or effects from propeller moments [85]. Three structural modes per blade are chosen as a compromise between accuracy and computational time. Including more (and therefore higher-frequency) modes would improve the accuracy, e.g., of the deflection shape under load, but lead to high-frequency content in the time response, which would lead to a required reduction of the time step and, therefore, an increased computational effort.

The first three in-vacuo eigenfrequencies and their development with rotational speed are presented in Fig. 3.4. The left plot shows the three eigenfrequencies in a blade Campbell diagram alongside the first ten harmonics of the rotational speed (thin lines starting at [0,0]). The three right plots depict the mode shapes in terms of flap (or out-of-plane) and lead-lag (or in-plane) deflection, starting at the bottom with the first blade mode. The first blade mode, "B1", is the first flap bending with some in-plane bending components due to the strong blade twist. The first eigenfrequency starts at 31.2 Hz in the non-rotating case. Due to geometric stiffening, it increases to 40.7 Hz at nominal rotational speed (vertical dashed line in the Campbell diagram). The second blade mode, "B2", resembles the first lead-lag bending with components of the second flap bending. Its eigenfrequency starts at 92.2 Hz and increases to 104 Hz at nominal rotational speed. Finally, the third blade mode, "B3", comprises components from the second flap and lead-lag bending. It increases its frequency from

148.5 Hz to 162 Hz. Due to the filled airfoil section and the resulting high torsional stiffness, no relevant torsional mode shape components arise in the first three mode shapes. At nominal rotational speed, the first blade mode is located at about 1.5P, meaning at about 150% of the current rotational speed. This is in accordance with other propeller blades from literature [96], indicating that the propeller blade model is representative.

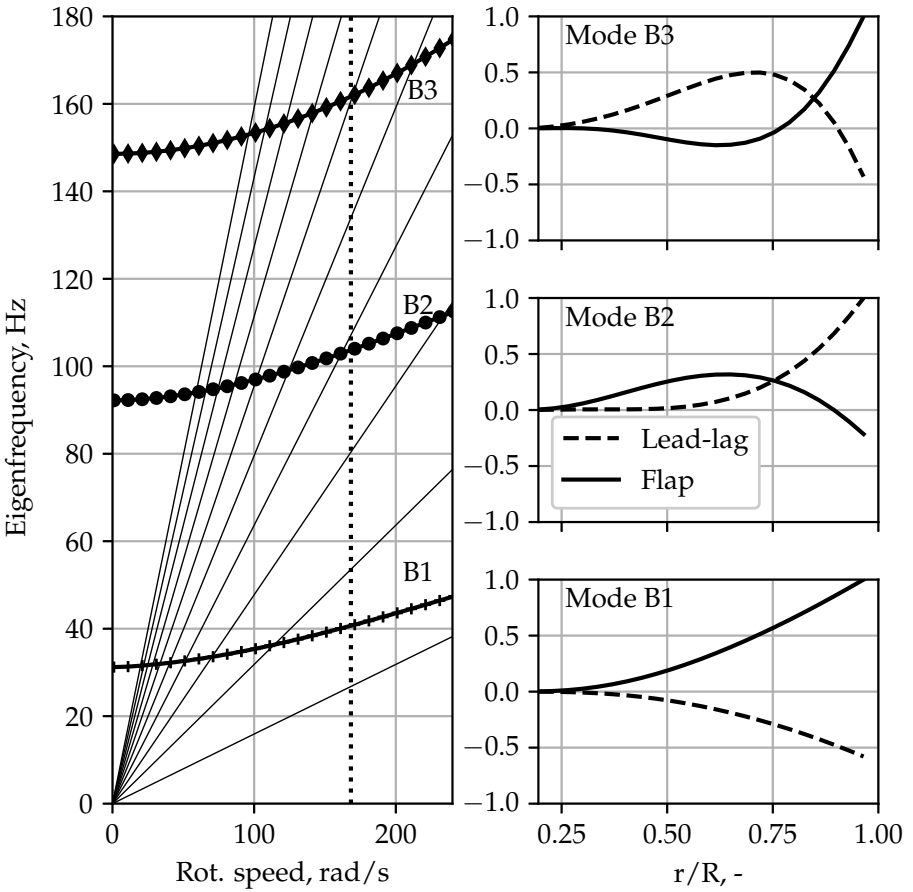

Figure 3.4.: Propeller blade Campbell diagram for the first three blade modes (left) and the corresponding mode shapes (right) in terms of flap and lead-lag motion (reproduced from [73, 74]).

3.1.3. Blade aerodynamics

The aerodynamic model of the blade is based on the airfoil characteristics of a symmetric NACA 0008 airfoil and only considers a constant lift curve slope of $C_{l\alpha}$ of 6.5864, which is used for the strip theory models. The geometry is discretized into strips with constant chord length (see Fig. 3.1). Two versions of the strip theory model are used in this study:

1. The aerodynamic model for the MBS model in Simpack, which is coupled directly to the structural model. In this case, twelve strips are distributed uniformly over the radius, covering two beam elements each and having a collocation point (in the middle of each strip) congruent with a structural node for coupling.
2. The aerodynamic models used for comparing different aerodynamic methods, which run externally in a Python code and are refined into twenty strips with a cosine distribution refining at the blade tip. The finer layout matches the UPM panel model, which also has 20 strips in radial and 30 panels in chord-wise direction.

The different propeller models are trimmed according to the workflow in section 2.2.3. If not stated otherwise, the trim is conducted for zero torque, called windmilling, and referred to as the critical case in literature [4].

Table 3.1.: Nominal operating point

Quantity	Symbol	Value
Airspeed	V	142 m/s
Shaft rotational velocity	Ω	167.5 rad/s / 26.7 Hz / 1600 rpm
Shaft torque	M_x	0 Nm
Air density	ρ	1.225 kg/m^3

Based on a reference operating point given in Tab. 3.1, two trim approaches are used within this thesis:

a) Constant pitch: By keeping the advance ratio $\mu = V/(\Omega R)$ constant, the angle of attack at the blade tip stays constant and the blade pitch angle can also remain constant over a range of airspeeds (in case of strip theory without inflow (*Wagner* from Tab. 2.2), at 32.67°). The shaft rotational speed is scaled accordingly to keep the advance ratio constant.

b) Constant speed: For the constant speed trim (which is more representative of larger propeller aircraft [97]), the blade pitch angle is adjusted to adjust the torque to the trim goal. The shaft speed is kept con-

stant. The trim angles required for zero torque using the strip theory model without inflow (*Wagner* from Tab. 2.2) are shown in Fig. 3.5

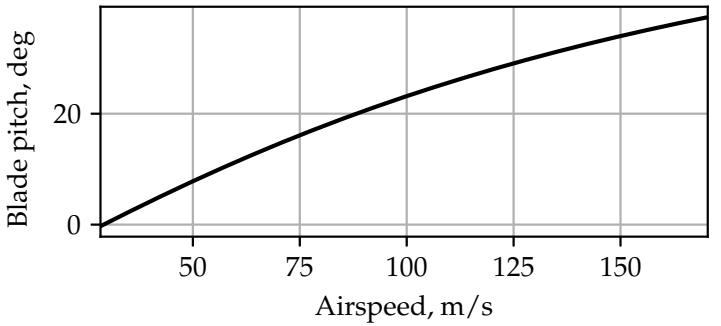

Figure 3.5.: Blade pitch for varying airspeed in the constant-speed windmilling trim.

3.2. Airframe models

Two airframe models are used in this thesis. The simplified pylon system from Fig. 1.1(b) is used for the verification and most parameter studies due to its simplicity. A generic, twin-engine turboprop aircraft model is employed to demonstrate the TM-method's application to a more complex aircraft configuration. Both models are briefly described in the following section.

3.2.1. Simplified Pylon Model

The first structural airframe model resembles the simplified pylon model from Fig. 1.1(b). It comprises a rigid pylon/engine that can pivot about a pivot point in a distance a behind the propeller plane. The pivoting in pitch and yaw directions is restrained by torsional springs. The engine itself has rotational inertia in both directions. The parameters of the nominal system are listed in Tab. 3.2, resulting in an uncoupled pitch and yaw frequency ($f_\theta = \frac{1}{2\pi}\sqrt{\frac{K_\theta}{J_\theta}}$) of 8 Hz. The stiffness values are varied to obtain whirl flutter stability maps as shown in Fig. 1.4.

Table 3.2.: Properties of the simplified pylon system

Property	Symbol	Value
Pitch/Yaw inertia	J_θ / J_ψ	100 kgm^2
Total polar inertia	J_P	6.5 kgm^2
Nominal pitch/yaw stiffness	K_θ / K_ψ	252662 Nm/rad
Distance pivot point to propeller plane	a	0.85 m

The (linearized) kinematic relations between pitch angle θ and the displacements at the propeller hub lead to the modal matrix $\underline{\Phi}_{hub}$ of the system as shown in Eq. 3.2

$$\underline{\Phi}_{hub} = \begin{bmatrix} 0 & 0 \\ 0 & a \\ -a & 0 \\ 0 & 0 \\ 1 & 0 \\ 0 & 1 \end{bmatrix} \tag{3.2}$$

The first column represents the rigid body pitch mode, and the second column represents the system's yaw mode.

3.2.2. Generic Turboprop Aircraft

The second airframe model comprises a free-flying aircraft configuration and was modified to the state used in this thesis in [76]. It represents a twin-engine, high-wing turboprop aircraft with twenty PAX and 6500 kg maximum take-off weight, as commonly found for commuter aircraft. The aeroelastic airframe model consists of structural and unsteady aerodynamic models. The configuration is generic and used to demonstrate the application of the TM-method on a full-aircraft level.

Fig. 3.6 outlines the configuration. The discretization is equivalent to the aerodynamic panel grid used for the DLM model (using the ZONA6-method implemented in the ZAERO aeroelastic software [98]). It comprises the wing and empennage lifting surfaces modeled using lifting surface panels, and the fuselage and nacelle bodies comprise body panels. The wing span is approximately seventeen meters; the fuselage is sixteen meters long.

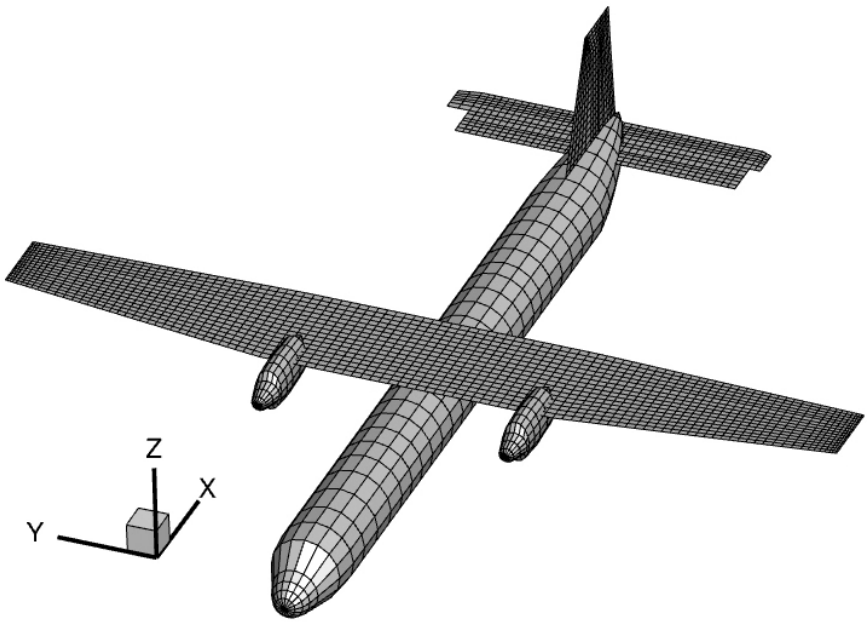

Figure 3.6.: Outline of the generic aircraft configuration on the aerodynamic panel grid

The structural model is a FEM model for MSC Nastran [99], including the wing, pylon, fuselage, empennage, and control surface structure. The fuselage is modeled with beam elements, and the rest of the structure is modeled by shell elements (e.g., for the wing box and pylon structure). Connections between the aircraft components are established with rigid RBE2 elements. Although individually modeled, the control surfaces are fixed. They cannot rotate with respect to the remaining structure to simplify the aeroelastic model since the focus should be on whirl flutter and not the control surface couplings. The mass distribution is partly modeled using material properties on the structure and with additional point masses connected using multi-point constraints (RBE3). Special attention is directed to the engine support, as this part of the structure is crucial for the whirl flutter stability. Fig. 3.7 shows a sketch of the engine support structure and the engine itself. The engine is modeled as a rigid point mass (compare the node marked as "Engine mass"), and a separate node at the propeller hub is rigidly connected to it (referred to as "Hub node"). The modal displacements of the two hub nodes (one on each side of the aircraft) make up the modal matrix $\underline{\Phi}_{hub}$ for the TM-method in Eq. 2.10. The engine is connected with rigid RBE2 elements (dotted lines) to the interface points, at which the

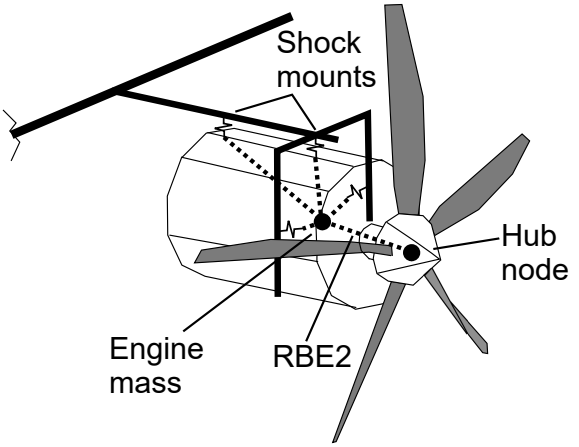

Figure 3.7.: Outline of the structural model of the engine and its support with shock mounts

engine is supported by elastomer springs ("Shock mounts"). The shock mounts are modeled as translational springs and are shown in Fig. 3.7 as small springs. The shock mounts connect the engine with the elastic pylon structure, which is attached at the leading edge of the wing box. To obtain a configuration that shows whirl flutter within the envelope and is therefore suited for studying whirl flutter, the shock mount stiffness values are chosen low to obtain low frequencies for the engine yaw and pitch modes. The structural model is fully unsupported, leading to six rigid body modes for the whole aircraft. These modes are considered in the flutter analysis but are not further post-processed and are omitted from the flutter plots for clarity.

The coupling between the aerodynamic and structural model is achieved using Infinite-Plate-Splines for the lifting surfaces and Thin-Plate-Splines [98] for the bodies. The components (wing, horizontal and vertical tail, control surfaces, fuselage, and nacelles) are splined individually. The front panels of the nacelle (representing the spinner) are splined to the engine nodes (marked in Fig. 3.7), while the rest of the nacelle panels are splined to the pylon nodes to visualize the relative motion between the engine and pylon.

Fig. 3.8 and 3.9 present the first eight structural modes shapes without any propeller influence, splined on the aerodynamic panel grid. The first two structural modes (Mode 7 and 8, as Modes 1-6 comprise the rigid body modes) make up the first wing out-of-plane bending, antisymmetric in Mode 7 and symmetric in Mode 8. Modes 9, 10, and 11 comprise couplings of the engine pitch with wing torsion, while modes 12, 13, and 14 show couplings of the first

wing in-plane bending with engine yaw motion. These six modes couple under the influence of gyroscopics to form the whirl modes of the engine, as section 4.4 shows. The modes 15 to 26 are shown in Appendix A.2, and the higher modes 27 to 50 are present in the analysis but not shown in this thesis.

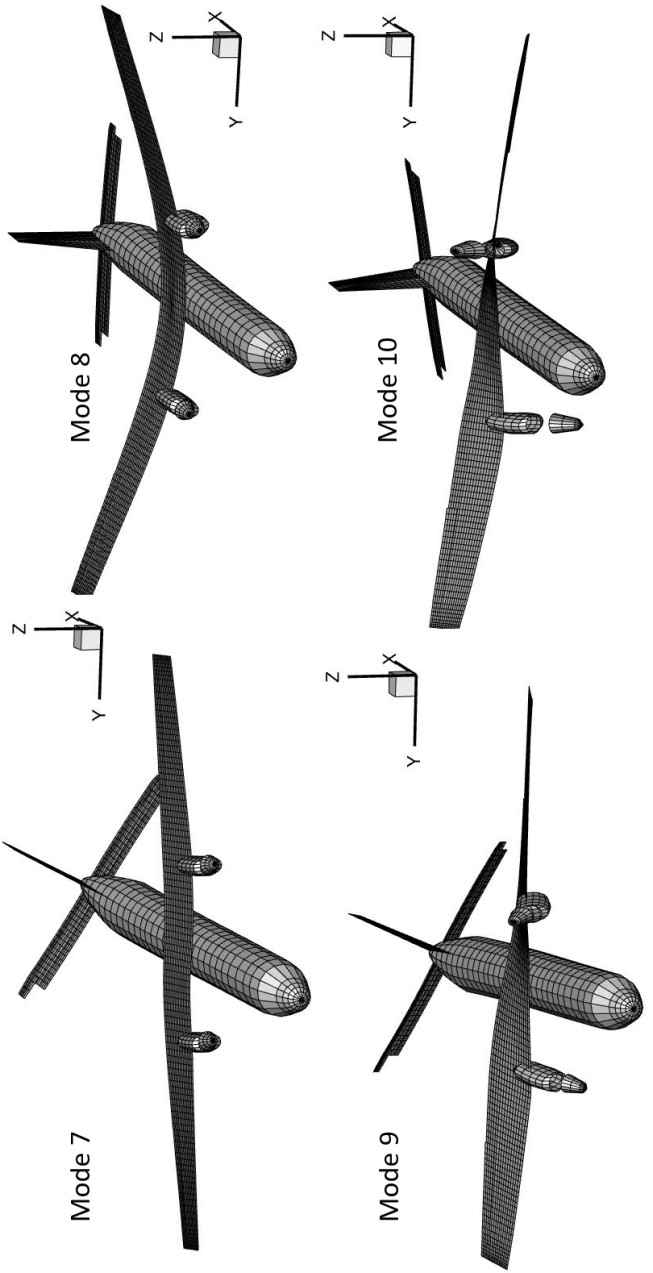

Figure 3.8.: The first four elastic modes (7-10) of the full aircraft, visualized on the aerodynamic panel grid

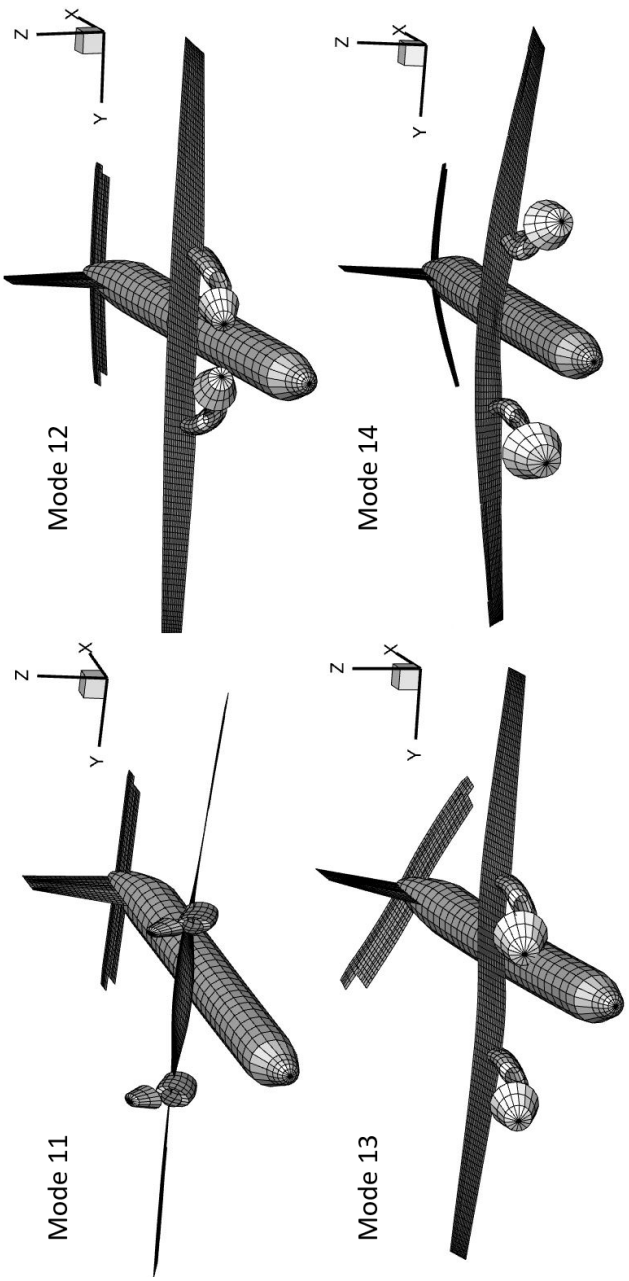

Figure 3.9.: The elastic modes 11-14 of the full aircraft, visualized on the aerodynamic panel grid

4
Results

Chapter 4 presents the results obtained within the scope of this thesis. The first section verifies the proposed TM-method by comparing stability results with available reference methods. After the verification, the effect of different modeling aspects on whirl flutter stability predictions, such as elastic blade modeling and the impact of the chosen aerodynamic method, is explored. The last section demonstrates the findings of the parameter study on a more complex airframe model.

4.1. Verification

Within the scope of this thesis, the proposed Transfer-Matrix method is verified by comparing results obtained with it with flutter results obtained with other, similar simulation methods to ensure the TM-method works correctly from a methodological point of view[15]. Two verification cases are considered:

4.1.1 Comparison of stability predictions for the simplified pylon model and a propeller with rigid blades. The classical Houbolt/Reed analysis and time-domain Floquet analysis are reference methods for this case. The transfer behavior captured by the transfer matrices comprises the unsteady aerodynamics from the Wagner strip theory.

4.1.2 Comparison of stability predictions for the simplified pylon model and a propeller with elastic blades. In this case, only time-domain Floquet analysis is used as a methodological reference. The transfer matrices for the propeller with elastic blades contain the unsteady aerodynamic response of the Wagner strip theory and the dynamic response of the elastic propeller blades.

[15] Validation in this context would require experimental results and would also encompass the modeling aspect of the simulations.

For each case, the identified transfer matrices are compared between harmonic and pulse excitation to check the numerical settings first (for the rigid blade case, transfer matrices are also compared with the Houbolt/Reed matrices). The primary verification is obtained by comparing flutter results (frequency and damping) over a range of airspeeds for a fixed-pitch trim. The verification in the rigid blade case is further enhanced by comparing a stability map similar to Fig. 1.4. Preliminary verification results with a different propeller and pylon model are published by the author in [71].

4.1.1. Rigid Propeller Blades

First, the transfer matrices for the nominal operating point from Tab. 3.1 for the case with rigid blades are compared. Fig. 4.1 presents the amplitude and phase of the complex transfer functions for propeller disc pitch θ (fifth column of Eq. 2.23), omitting the x-components. The left column contains the in-plane force transfer functions, and the right column includes the in-plane moment transfer functions. Transfer matrices obtained with the Houbolt/Reed method are shown as dashed lines. To better compare with the transfer matrices obtained with the Wagner strip theory, the aspect ration correction (see. Eq. 2.21) was omitted. The solid lines represent the transfer matrices obtained using pulse perturbation of the rigid propeller model in Simpack. A pulse with an amplitude of 0.001 rad and a maximum excitation frequency of 30 Hz (compare section 2.2.3) was chosen, and the response was recorded for 51 pulse widths with 101 time steps per pulse width. To verify the numerical settings of the pulse perturbation, a few transfer function samples were also computed using harmonic excitation with the same amplitude (markers in Fig. 4.1), using five periods of the harmonic excitation, of which the first two were omitted to exclude the transient response. Three hundred sixty time steps per period were used.

The transfer functions match precisely when comparing the pulse and harmonic identification results. This means the pulse excitation gives valid frequency-domain transfer functions in the frequency range of interest. When comparing to the transfer functions from the Houbolt/Reed method, overall, a good fit regarding amplitude and phase is found. The match is better for low frequencies and becomes worse at the higher end of the frequency range. This can be explained by the assumptions made in the Houbolt/Reed method, such as the definition of the reduced frequency k in Eq. 2.20. The Houbolt/Reed method only considers the rotational speed Ω for the reduced frequency, assuming $\omega << \Omega$ [8]. In the case of Fig. 4.1, the rotational speed is at 26.7 Hz, explaining the more significant difference between the methods in the higher frequency range. Section 4.3 compares the different aerodynamic methods more closely. For this verification, the exact fit between the harmonic and pulse

transfer functions and the good fit between the identified and the Houbolt/Reed transfer functions are sufficient.

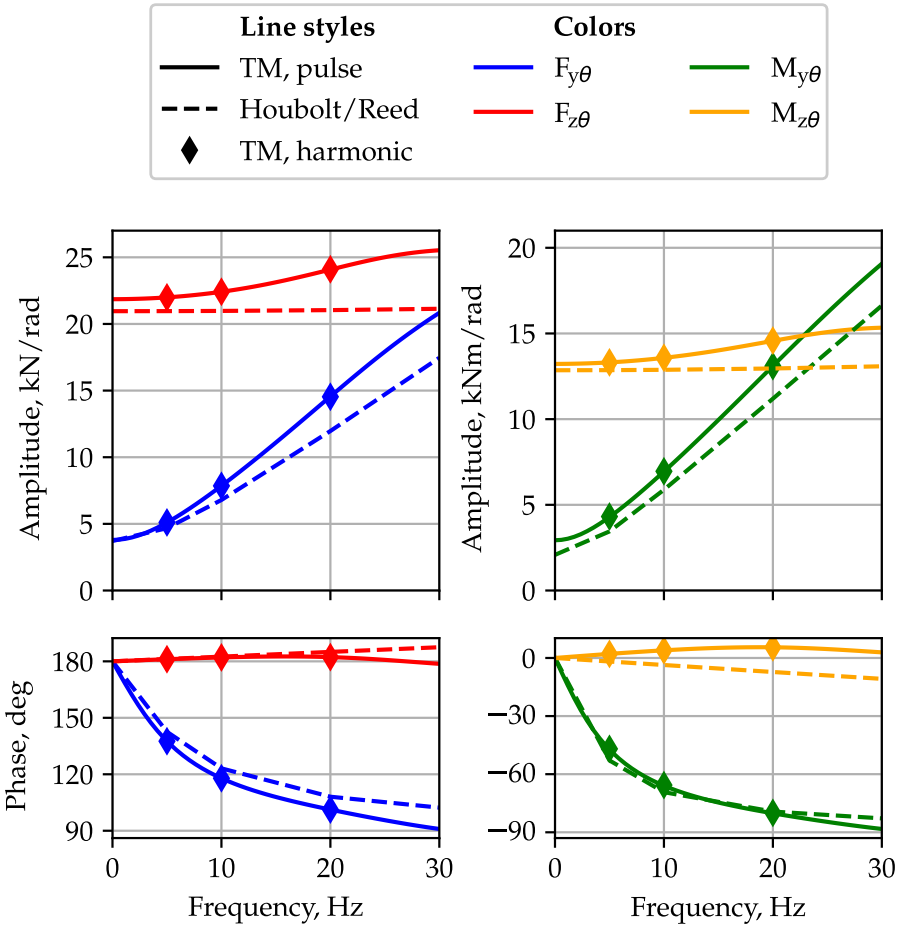

Figure 4.1.: Comparison of transfer matrices for the rigid propeller between TM-method and Houbolt/Reed.

Before extending the operating range to an entire flutter plot with varying airspeed, stability results for the nominal operating point using the transfer matrices shown in Fig. 4.1 are compared. Fig. 4.2 compares three whirl flutter stability maps. The dashed line is the stability map computed using the Houbolt/Reed approach, while the solid line represents results from the TM-method.

For verification, some points were sampled using the time-domain Floquet method. While the Houbolt/Reed method differs in modeling the propeller aerodynamics, the other methods are based on the same Simpack model of the propeller. Hence, the hypothesis is that the TM-method and Floquet analysis results should match exactly, while the Houbolt/Reed method can show offsets (similar to Fig. 4.1). Comparing the stability maps in Fig. 4.2 confirms the hypothesis. The stability boundary separating whirl flutter and stable areas of engine suspension frequencies matches precisely between the two methods based on the Simpack model. Regarding computational time, the Floquet-analysis evaluation is more expensive, though. The results of the Houbolt/Reed method show a slightly more unstable system with a three percent larger extent of the whirl flutter boundary. The divergence predictions (horizontal/vertical part of the boundary) are closer between the three methods.

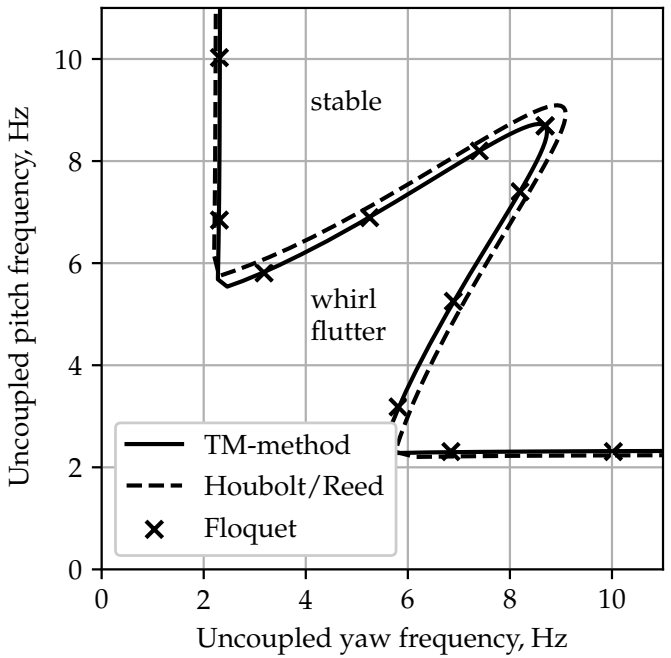

Figure 4.2.: Comparison of whirl flutter stability maps for rigid propeller between the TM-method, the Floquet reference and the Houbolt/Reed method.

Finally, for the rigid blade case, frequency and damping trends over a range of airspeeds are compared between the three methods. The results are obtained for the fixed-pitch windmilling trim in a velocity range from $0.2V_D$ to $1.2V_D$ using 21 velocity steps. The transfer matrices for the TM-method were identified for each operating point and not interpolated over the airspeed. For the Floquet analysis, all system states were considered, making the results an exact reference. The nominal stiffness configuration with 8 Hz uncoupled pitch and yaw frequency was chosen within the unstable range in Fig. 4.2. Hence, the system shows a backward whirl flutter instability at nominal operating conditions (142 m/s). As for the stability map, two hypotheses are tested: The TM-method and the Floquet-reference results should match precisely due to the same underlying model. The Houbolt/Reed results are expected to show a slightly more unstable behavior based on Fig. 4.2.

As expected, all damping trends for the backward whirl mode in Fig. 4.3 show a flutter crossing around 130 m/s, below nominal airspeed. For higher airspeeds, the system is unstable with a backward whirl flutter. The forward whirl mode stays at positive damping values and keeps a positive damping trend (damping values are outside the plot for higher airspeeds). The frequencies of the forward and backward whirl mode diverge for increasing velocity due to the increase in gyroscopic effects. Gyroscopic coupling rises due to the increasing rotational speed along the x-axis (proportional to the airspeed). The slight negative curvature in the frequency trends is caused by the increasing negative aerodynamic stiffness. Also, both hypotheses from Fig. 4.3 can be confirmed. The frequency and damping predictions for TM-method and Floquet analysis match precisely in the airspeed range covered. The Houbolt/Reed method results show similar trends as the TM-method results but predict slightly lower damping values and an earlier flutter crossing (about five m/s lower). The differences are more significant for the forward whirl mode, which also shows a slightly increased frequency at higher airspeeds.

Summarizing the verification results for the rigid blade case, the TM-method could successfully be verified with the exactly matching time-domain Floquet reference results. The Houbolt/Reed method gives very similar results, further increasing the fidelity of the verification but showing minor differences attributed to different propeller modeling assumptions.

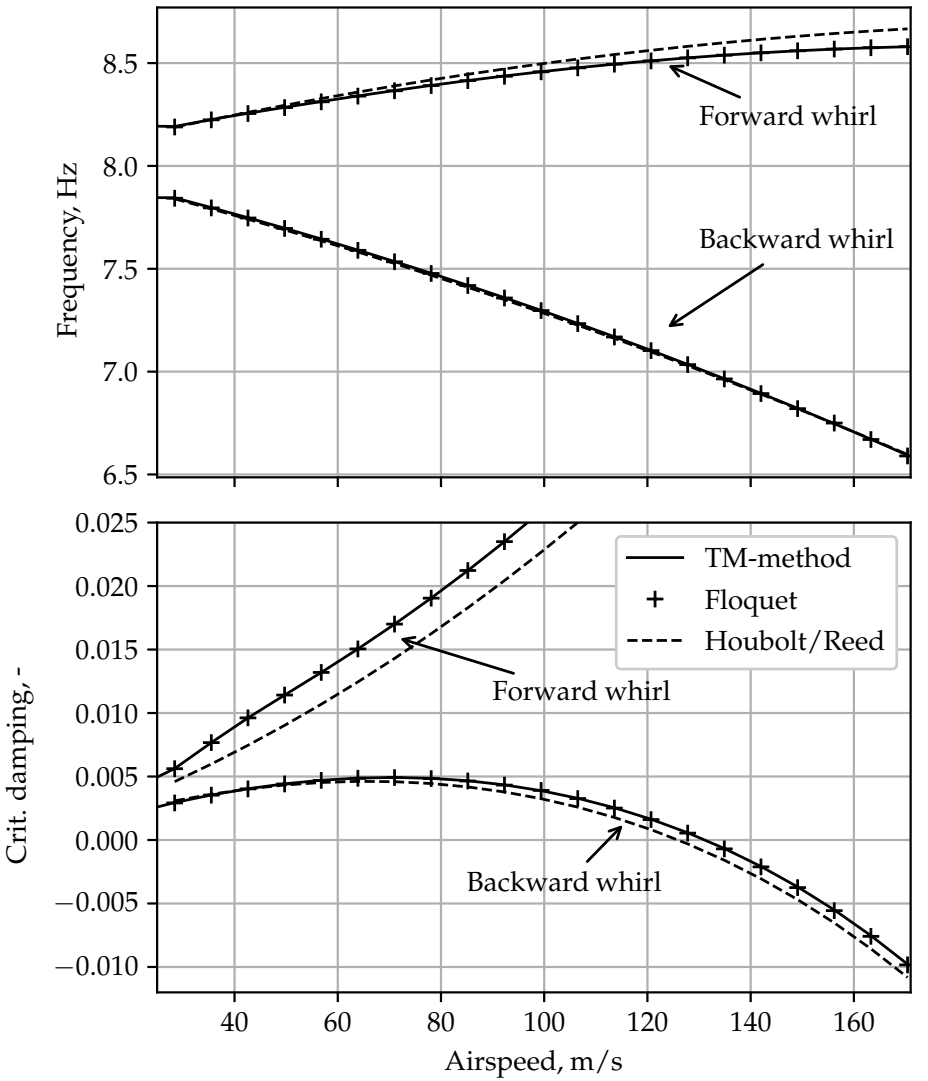

Figure 4.3.: Comparison of frequency and damping for varying airspeed and a fixed-pitch windmilling trim between three stability analysis methods. The two modes of the simplified pylon system (forward and backward whirl) are labeled.

4.1.2. Elastic Propeller Blades

For the verification case with elastic propeller blades, the frequency-domain transfer matrices contain more dynamic content due to the added dynamic response of the flexible propeller blades. Because the Houbolt/Reed method assumes rigid blades, it is omitted in this case, and only the two Simpack approaches are compared. Similar results obtained with a slightly different propeller system are published in [73, 74].

First, the numerical procedure for identifying the transfer matrices using pulse excitation is checked by comparing them to transfer samples from harmonic identification. Due to the model's higher dynamic content, the numerical settings for the identifications were refined. A maximum excitation frequency of 250 Hz was chosen for the pulse to identify the highest blade mode. The shorter pulse was furthermore sampled with 201 time steps per pulse width. To get a high frequency resolution within the frequency range of interest and adequately capture the transfer behavior, the response was recorded for a time equal to 501 pulse widths. Similarly, the response to the harmonic excitation was also extended to 20 periods, and only the last five were used for identification. The perturbation amplitudes stayed constant compared to the rigid blade case.

Fig. 4.4 presents the transfer functions for propeller disc pitch excitation θ in a frequency range between zero and 250 Hz. Harmonic transfer functions were sampled up to 80 Hz. The upper two plots show the amplitude of the in-plane force and moment transfer functions and the lowest plot shows the corresponding phase angles. While the transfer functions in the rigid blade case in Fig. 4.1 only represent the unsteady aerodynamic response, the transfer functions in this case also contain the dynamic response of the blade modes to the hub excitation. Hence, distinct resonance peaks can be observed in the amplitude spectra alongside the corresponding phase jumps. The resonance peaks are not located at the rotating blade eigenfrequency (see, e.g., Fig. 3.4), as the hub loads are in the non-rotating system and, therefore, the response of the combined propeller is recorded. Consequently, the peaks are located at the frequencies of the global propeller modes (see section 2.4). An excitation by disc pitch mainly excites the first cyclic modes. Thus, two peaks (regressive and progressive cyclic) per blade mode are present. The frequencies of the propeller modes are marked with vertical lines (dashed for regressive, dotted for progressive) and labeled according to the blade mode from Fig. 3.4.

The comparison between harmonic and pulse excitation shows no differences in amplitude or phase. It can be concluded that pulse excitation also works for the elastic blade case. For this case, the benefit compared to harmonic excitations becomes evident since the sampling rate in the frequency range of interest is higher with pulse excitation, leading to much smoother transfer functions.

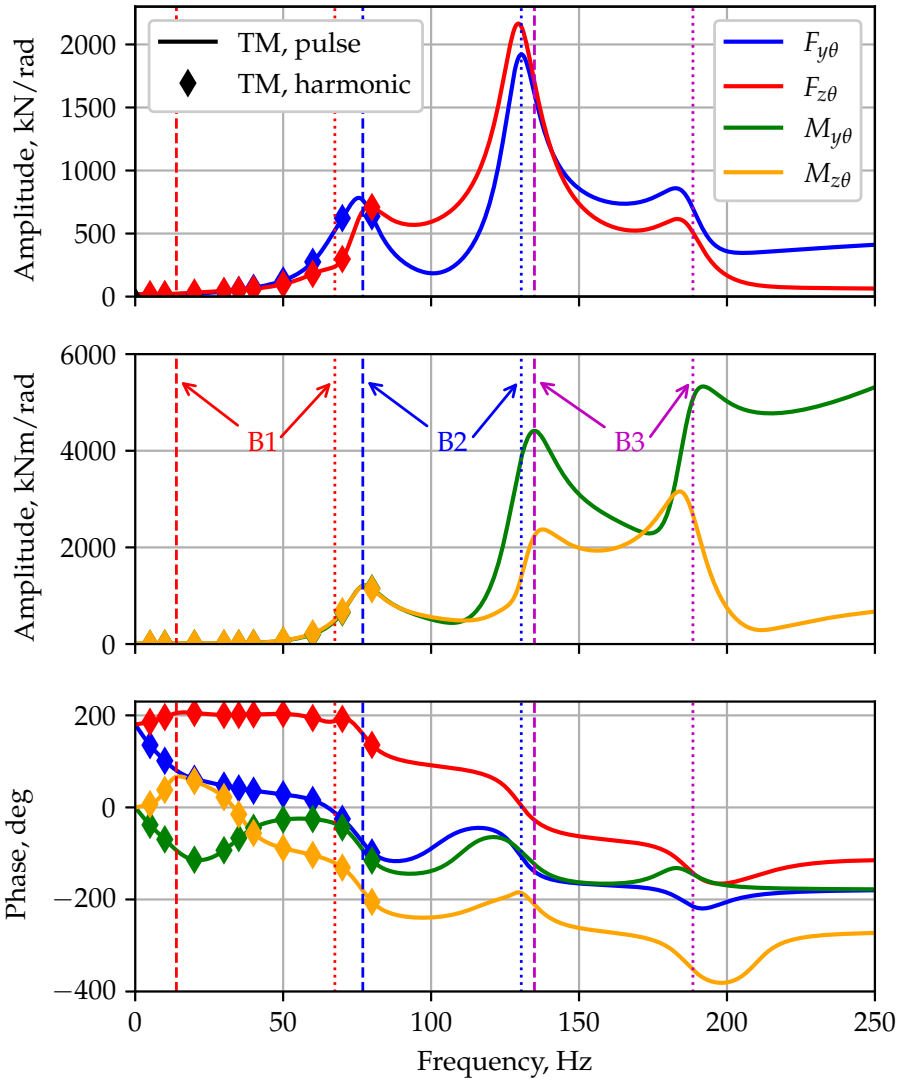

Figure 4.4.: Comparison of transfer matrices for the flexible propeller.

Fig. 4.5 presents the results of a flutter analysis of the simplified pylon system with flexible blades over a range of airspeeds. The results are again computed with a fixed-pitch trim in a velocity range from $0.2V_D$ to $1.2V_D$ using 21 velocity steps. The transfer matrices for the TM-method were identified for each operating point and not interpolated over the airspeed. The TM-method results are presented as solid lines and were obtained using the cFRF solver (see section 2.1). The reference results (markers) were computed with the Floquet analysis. Due to the presence of rotating blade states, the aerodynamic states were omitted from the analysis (see section 2.4). Hence, slight differences in the damping predictions might occur, but the unsteady aerodynamics based on Wagner were still retained for compatibility with all previous verification results. Appendix A.3 shows the same comparison of results obtained with quasi-steady aerodynamics. The Floquet results in this case are exact.

Fig. 4.5 presents the frequency and damping of the relevant system modes. In this case, more modes are contained compared to the rigid blade case in Fig. 4.3 due to the presence of elastic blade modes. As before in Fig. 4.4, the elastic blade modes are presented in global, non-rotating propeller modes. The modes shown comprise the two pylon whirl modes ("plus" and "circle" markers), the collective mode ("tri-star" for the collective B1 mode), the first-order cyclic modes (regressive B1 as "triangle", progressive B1 as "squares", regressive B2 as "stars"). The remaining modes (B2 collective upwards) are outside the plot at higher frequencies and not shown here. Also not shown are the second-order cyclic modes, which do not interact with the pylon modes and are omitted for the simplicity of the plot. From Fig. 4.5, several observations can be drawn:

1. The frequency and damping predictions between Floquet and TM-method fit very well. The damping trends stay positive over the full range of airspeeds. Small deviations can be observed for the forward whirl mode damping at high velocities, which is attributed to the deviation in damping in the Floquet analysis due to the omission of the aerodynamic states[16].

2. The TM-method does not capture the collective B1 mode. This is due to the lack of DOF of the pylon in the x-direction, so the respective transfer-matrix terms vanish from the generalized propeller forces. In case the pylon had modes showing x-motion, the cFRF method could find the collective modes. Because it is not relevant for whirl flutter, this does not impact stability predictions.

3. Beyond 160 m/s, a mode switch occurs between the progressive-cyclic B1 mode and the regressive-cyclic B2 mode for the TM-method (see the switch in damping). This is caused by the lack of mode-tracking for the blade modes. The blade modes are not explicitly represented in the

[16] The damping predictions for quasi-steady aerodynamics match exactly, compare App. A.3

eigenvectors of the systems, as they are hidden as poles in the right-hand side of Eq. 2.14 and can, therefore, not be tracked directly. This does not affect the mode-tracking for airframe modes, as the modes of the airframes make up the components of the eigenvectors of Eq. 2.14 and can, therefore, be tracked directly.

4. Differences occur in the frequency and damping predictions for the regressive-cyclic B1 mode for higher velocities. B1 is the first flap mode and shows very high levels of (aerodynamic) damping. The regressive-cyclic B1 mode at 80 m/s already has a damping higher than 20%. The peaks in the system response (see Eq. 2.7) are, therefore, very low and hard to fit precisely by pole-fitting routines. Fig. 4.6 shows an example system transfer function as an input for the cFRF solver at 114 m/s (first column of $\underline{H}_{system}$), with the modes of the system marked as vertical lines. The two whirl modes with the lowest damping can be identified as peaks in the amplitude spectrum and phase jumps in the phase spectrum, whereas the higher-damped blade modes are more challenging to spot. However, this difficulty of precisely predicting the eigenvalues of highly damped modes does not affect flutter stability predictions, as the modes of interest here are lowly damped.

The TM-method can recover the frequency and damping of the pylon whirl modes accurately and gives predictions for the frequency and damping for the relevant (cyclic) blade modes. The latter can be recovered using the cFRF solver but cannot be tracked accurately due to the missing eigenvector components. For propeller whirl flutter analysis, where mainly the frequency and damping of the airframe modes are of interest, the TM-method is well-suited and computationally less expensive than time-domain Floquet analysis (especially for studies with more complex airframe models).

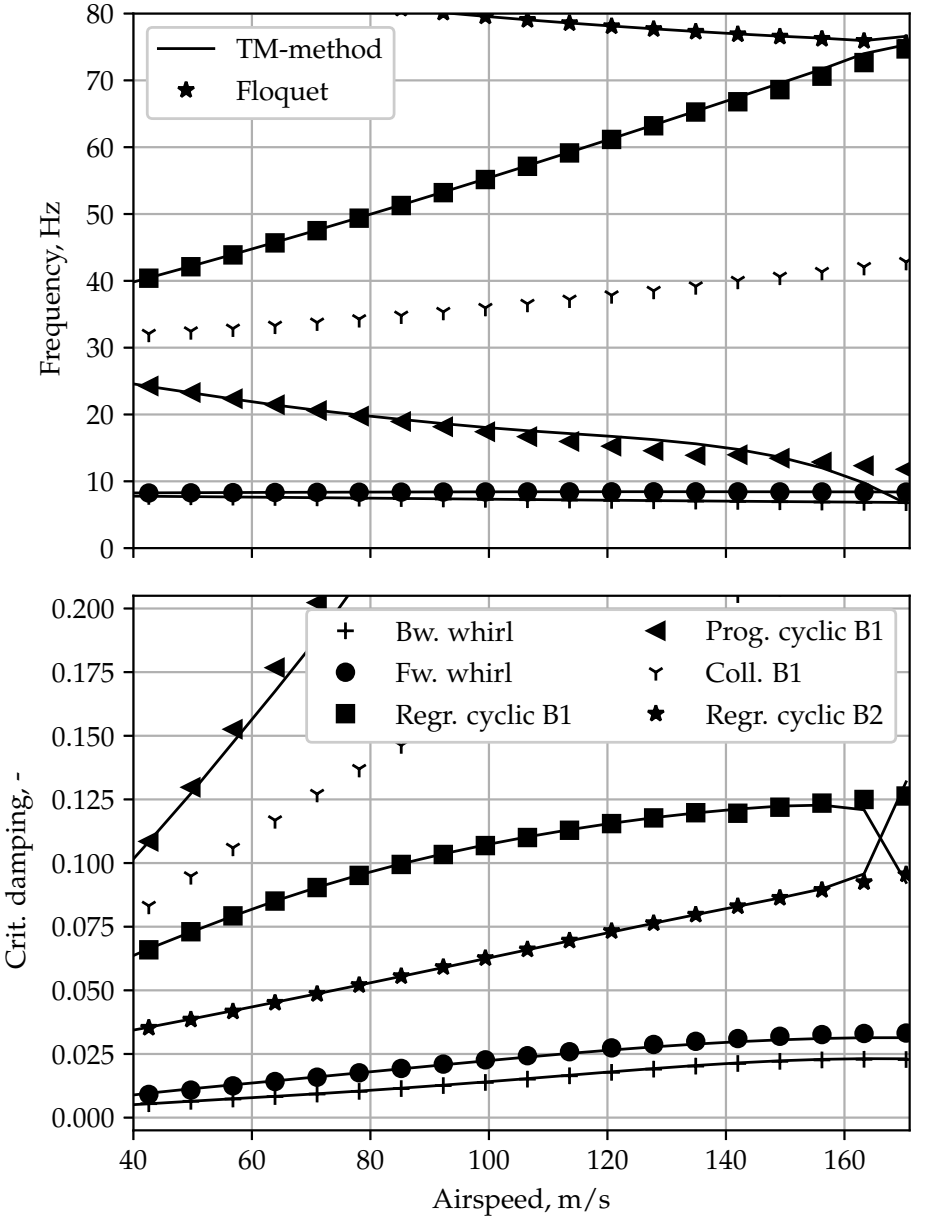

Figure 4.5.: Comparison of flutter results for the simplified pylon system with elastic blades

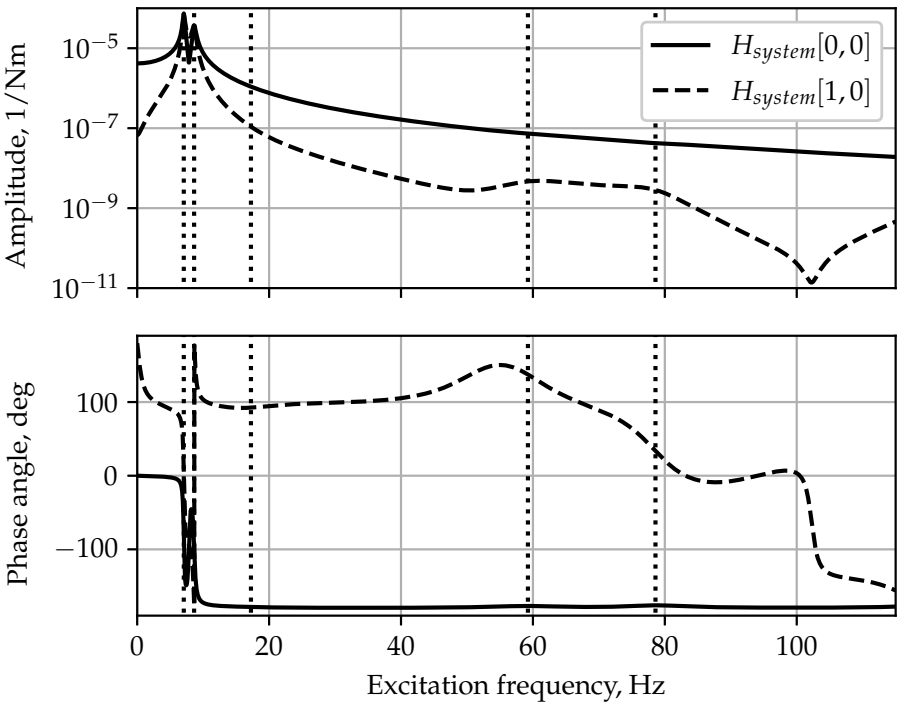

Figure 4.6.: Two entries of the transfer function of the coupled system, together with the system poles (as vertical dotted lines)

4.2. Influence of blade elasticity

After successfully verifying the TM-method for the isolated propeller model with rigid and flexible blades, this section applies the TM-method to study the influence of blade elasticity on whirl flutter more extensively. The main goals of this section are to

1. Reproduce the stabilizing effect of blade elasticity reported in literature [55, 57] using the TM-method in conjunction with frequency-domain flutter analysis.
2. Use the transfer matrices to gain more insights into the driving effects behind the stabilization.

The comparisons and results can also be found in previous publications by the author [73, 74], which uses a slightly different propeller and pylon system.

The results for the flutter plots of the simplified pylon system in fixed-pitch trim conditions using rigid and flexible propeller blade modeling have already been presented separately in Fig. 4.3 and 4.5. Fig. 4.7 compares the frequency and damping for the backward and forward whirl modes from both plots. The pylon structure is the same in the rigid and flexible blade analysis, and both propeller models use the Wagner strip theory in fixed-pitch windmilling trim. All plots shown from here on contain results obtained with the TM-method using pulse identification for the transfer matrix generation. The only difference is the modeling of the blade structure, which is rigid in one case and flexible in the other. Significant discrepancies become apparent when comparing the stability behavior of the backward whirl mode in both cases. While with the rigid blades, the system becomes unstable at 130 m/s, for the flexible case, the backward whirl mode stays stable. It has a positive damping trend within the airspeed range without any trend towards instability. Slight differences also appear in the frequency of the backward whirl mode at higher airspeeds. Comparing the damping of the forward whirl mode between the two cases reveals a decrease in damping for the flexible case, but the damping level stays well above the backward whirl mode, and trends are still positive. It can be concluded that the influence of blade elasticity is strongly stabilizing on the backward whirl mode and destabilizing on the forward whirl mode. The system with rigid blades shows whirl flutter within the airspeed range studied. The system with elastic blades does not. The results obtained with the TM-method confirm the findings in the literature obtained mainly by time-domain analysis or direct linearization [55].

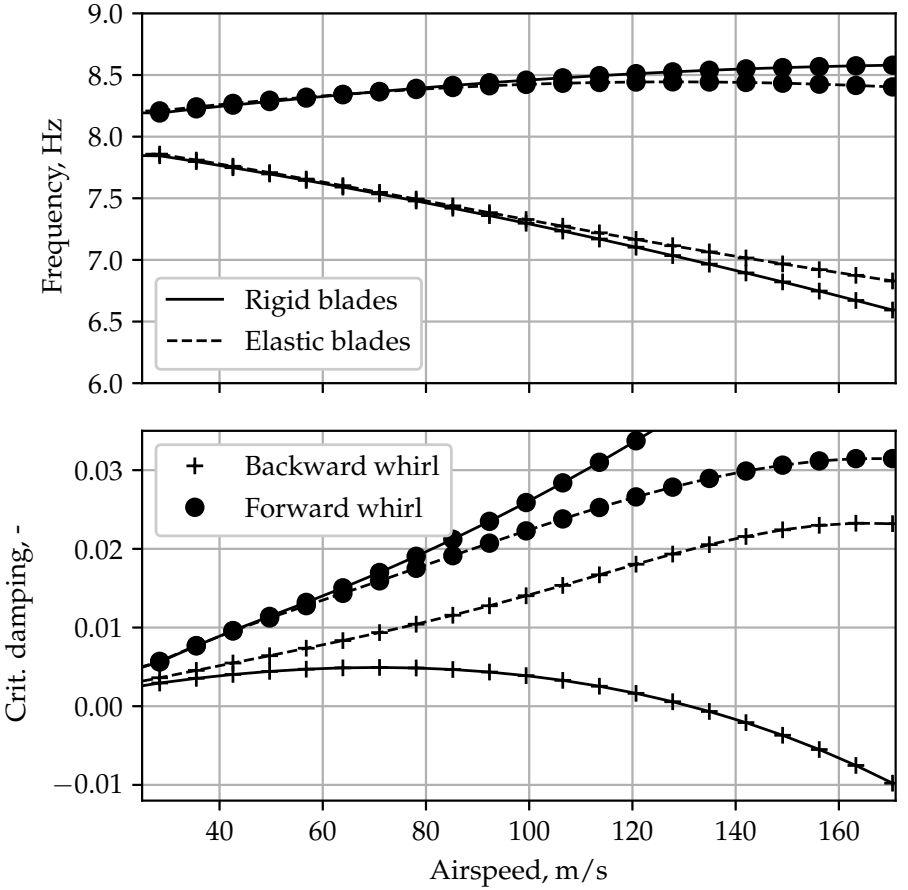

Figure 4.7.: Comparison of whirl flutter results for the rigid and elastic propeller over a range of airspeed.

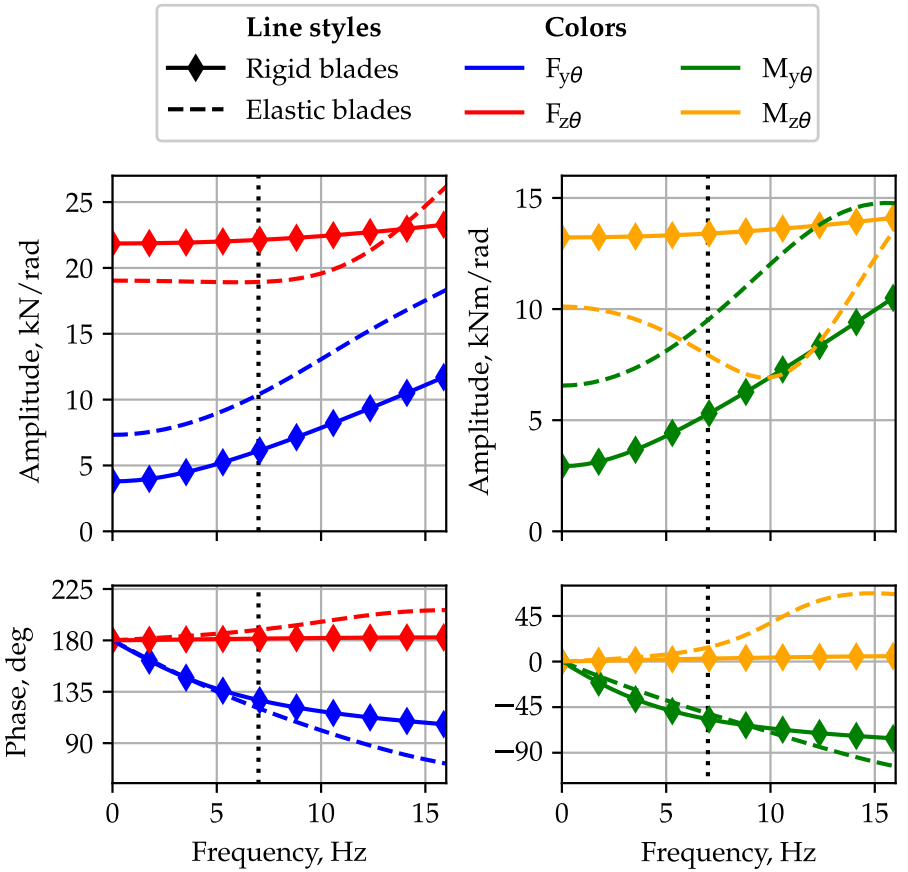

Figure 4.8.: Comparison of transfer matrices for the rigid and flexible propeller.

The reason for the stabilization of the backward whirl mode in the elastic blade case can be found in the altering of the propeller hub transfer function. The in-plane load transfer functions for propeller disc pitch are compared in Fig. 4.8 in amplitude and phase. The coupling moment $M_{z\theta}$ in the top right plot (and the symmetric component $M_{y\psi}$, respectively) is reduced in the frequency range relevant for the whirl modes (around 8 Hz, backward whirl frequency is marked as dotted line), as Fig. 4.8 demonstrates for the nominal operating point marked at 142 m/s. This coupling moment is the leading cause for backward whirl flutter instability (see Fig. 2.5), and its reduction in amplitude by 40 percent compared to the rigid blade case is the reason for the stabilization. All other components of the transfer matrices are also affected, but the changes mostly cancel each other. For example, the increase in the stabilizing force transfer function $F_{y\theta}$ is canceled by the decrease in the also stabilizing $F_{z\theta}$. The change in phase of the complex transfer functions compared to the rigid case is minimal at the whirl flutter frequency of 7 Hz. At higher frequencies, the start of the first resonance peak in the transfer functions for the elastic blade case can be seen (e.g., in $M_{y\theta}$, the dashed green line in the top left plot), caused by the dynamic response of the regressive-cyclic B1 mode (around 15 Hz).

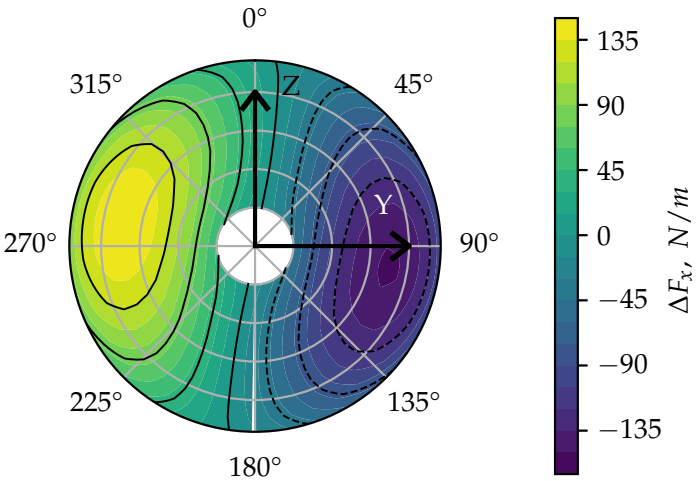

Figure 4.9.: Contour plot of the x-component of the rigid blade lift over one revolution under 1°angle of attack

To explain the decrease in the coupling moment $M_{z\theta}$, Fig. 4.9-4.11 take a look at the response of the blade to disc pitch for zero frequency. Fig. 4.8 shows a significant offset between the rigid and flexible blade transfer functions already

at zero frequency. This response is equivalent to the so-called 1P hub loads, the propeller load response to a steady disc pitch angle. Fig. 4.9 shows the load distribution of one blade over one revolution under 1° disc pitch about the positive y-axis. The plot only shows the axial component of the lift force (or global x-component, respectively). The steady lift distribution under axial conditions was subtracted, too. Disc pitch about the y-axis means the top of the disc (positive z-direction) tilts forward. The direction of rotation is clockwise.

During the down-stroke of the blade (on the right side at 90°azimuth), the local airfoil sections experience a lower angle of attack due to the global disc pitch angle, compare Eq. 4.1. Hence, the blade produces less lift on the down-stroke, as seen in the negative delta load in Fig. 4.9. The same, but reverse, can be said for the up-stroke on the left side of the disc, where the blade sections experience an increase in angle of attack and, therefore, lift.

$$\Delta\alpha_{kin} \;=\; -\theta \sin(\Omega t) \tag{4.1}$$

The resulting axial force distribution, as shown on the disc in Fig. 4.9, is mainly anti-symmetric about the global z-axis, following the anti-symmetric angle of attack distribution. This results in the moment about the z-axis, $M_{z\theta}$. Because the terms about the z-axis are in phase with the quasi-steady angle of attack variation, they are named in-phase components in this thesis. Due to the unsteady lift lag effect (modeled with Wagner's function here), the maxima of the unsteady lift are delayed with respect to the angle of attack maxima at 90° and 270° and therefore at slightly higher azimuth angles. The azimuthal offset also produces a small moment about the global y-axis ($M_{y\theta}$). Similar to the in-phase components, the forces and moments about the y-axis are called out-of-phase components as they are out of phase with the angle of attack perturbation. The tangential force on the blade follows a similar pattern and produces the two in-plane force components, $F_{y\theta}$ and $F_{z\theta}$

The blades run through the loading shown in Fig. 4.9 once per revolution and experience a periodic excitation. In the case of elastic blades, this triggers a dynamic response of the blade bending dynamics. The negative loading on the down-stroke bends the blade backward, while positive loading on the other side bends the blade forward. Fig. 4.10 shows this by comparing the tip path of the flexible blades (dashed line) with the one for the rigid blades (solid line). Two factors drive the magnitude of the deflection: the blade stiffness, which determines the blades' quasi-steady response to the loading, and the frequency placement of the blade eigenfrequency with respect to the rotational speed (which is the frequency of the periodic load in this case). The closer the rotational speed comes to the eigenfrequency, the higher the dynamic

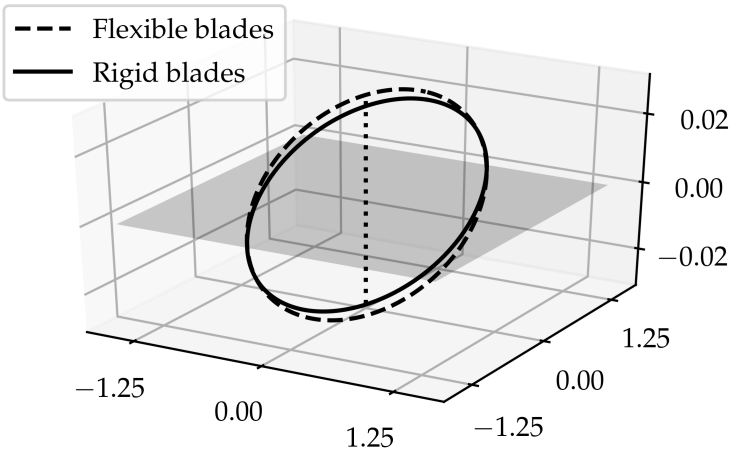

Figure 4.10.: Comparison of the tip path plane for the rigid and elastic blades under steady angle of attack

amplification due to resonance. The dynamic response is also phase-shifted to the loading, leading to a further azimuthal shift of the deformation maximum.

The periodic deflection of the blades leads to additional hub loads due to inertial forces. For example, the deflection of the blades when passing through the 90° and 270° position leads to an x-offset of the blade masses to the propeller plane. Hence, the centrifugal forces on the blade masses create a moment about the z-axis that counteracts the aerodynamic moment from Fig. 4.9.

The periodic bending deflection of the blades induces additional motion components on the blade sections, changing the local angle of attack (e.g., due to a flap velocity). This leads to an azimuthal shift in the angle of attack and, therefore, aerodynamic lift distribution. Fig. 4.11 shows the axial force distribution for the flexible blade case, similar to Fig. 4.9 for the rigid blade case. Comparing the two distributions, the shift of the lift maxima towards higher azimuth angles can be seen clearly. The shift is higher at the outer radii, where the bending deflection of the first bending mode (the one with the closest frequency spacing) is highest. The azimuthal shift in the aerodynamic forces brings the maxima closer to the global z-axis. It reduces the in-phase component while increasing the out-of-phase components about the y-axis. Both can also be seen in the moment transfer functions in the top left plot of Fig. 4.8 for zero frequency.

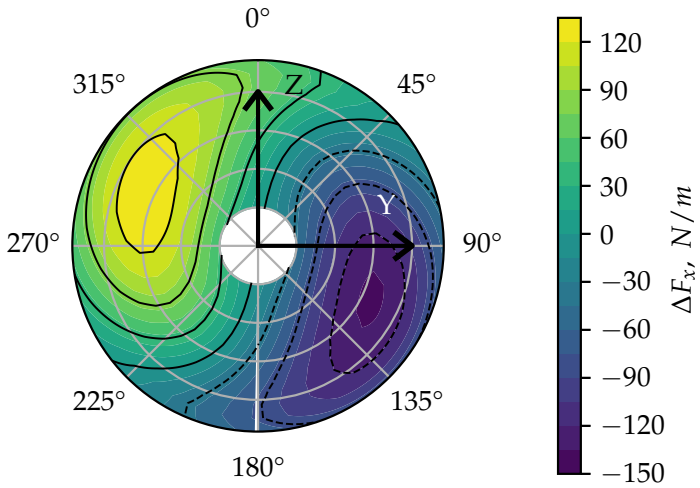

Figure 4.11.: Contour plot of the x-component of the flexible blade lift over one revolution under 1°angle of attack

It can be concluded that at least two effects contribute to the decrease in $M_{z\theta}$: the counteracting moment from the centrifugal loads due to the blade deflection and the reduction of the aerodynamic moment due to the angles of attack induced by the blade dynamic response. The effects are explained here for the case of zero pitch frequency due to simplicity but extend towards the higher frequencies.

To further investigate the effect of different levels of blade elasticity on whirl flutter stability, Fig. 4.12 and Fig. 4.13 present whirl flutter stability maps with different blade stiffness and eigenfrequency settings. Fig. 4.12 shows the whirl flutter stability maps for the simplified pylon system with scaled blade stiffness values. The reference rigid blade case from Fig. 4.2 is shown (solid line), as well as three different stability boundaries for different blade stiffnesses. The nominal stiffness (K=100%, dashed line) as well as a case with reduced stiffness (K=75%, dash-dotted line) and a case with four times the nominal stiffness (K=400%, dotted line). All stiffness directions of the blade (tensile, bending, torsion) have been scaled with the same factor.

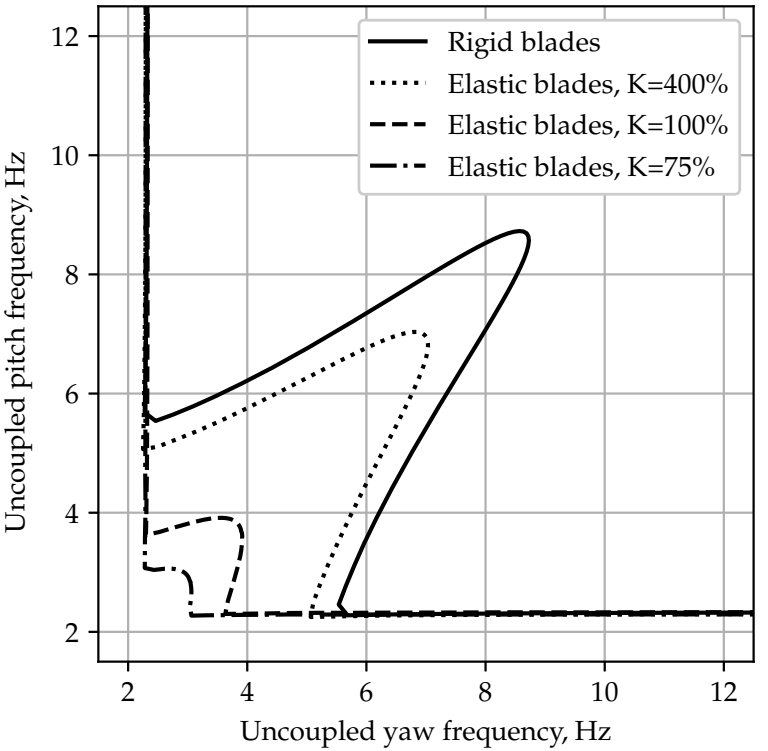

Figure 4.12.: Comparison of whirl flutter stability maps with varying blade stiffness

The hypothesis going into this plot is based on the findings in the previous paragraphs: A decrease in blade stiffness should lead to higher deflection and higher azimuthal load shift due to the lower stiffness and eigenfrequency of the blades and should, therefore, be stabilizing. Fig. 4.12 confirms this hypothesis. The nominal stiffness case (dashed line) shows a significantly smaller extent of the area of whirl flutter instability. The required uncoupled pitch and yaw frequency for stability in the symmetric case is reduced to 43% compared to the rigid case (resulting in only 18.5% of stiffness needed). Decreasing the blade stiffness further (dash-dotted line) almost eliminates the area of whirl flutter. Even the stiffer blade with four times higher stiffness still shows significant offset from the rigid blade case. The stiffer blades require 20% less uncoupled pitch and yaw eigenfrequency. Decreasing the blade stiffness and, therefore, the eigenfrequencies of the blades has a stabilizing effect on the whirl flutter of the simplified pylon system. Static divergence (the horizontal and vertical parts of the stability boundary) are not affected by scaling the stiffness, as the

reduction in destabilizing $F_{z\theta}$ is compensated by an increase in the destabilizing $M_{y\theta}$ (compare Fig. 4.8).

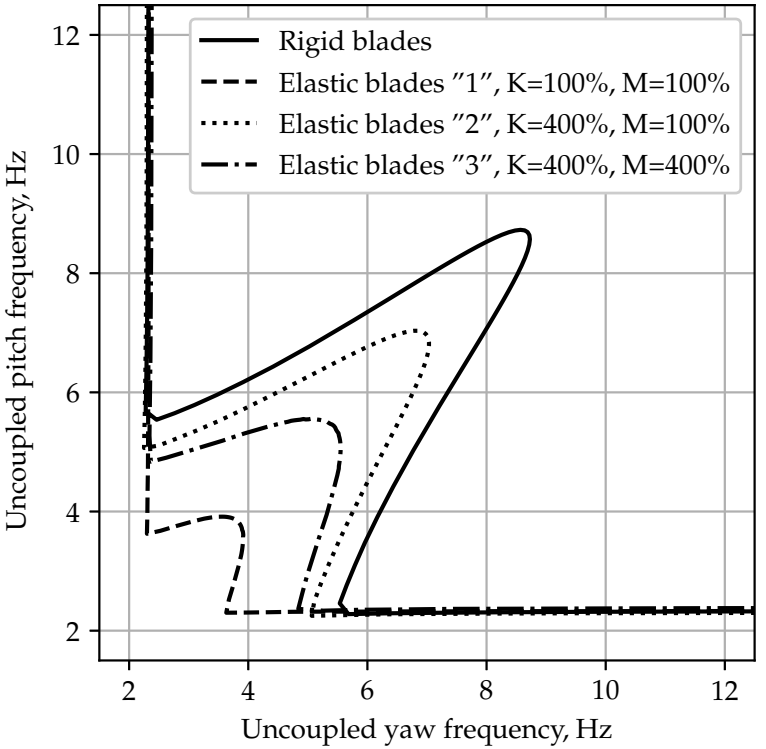

Figure 4.13.: Comparison of whirl flutter stability maps with varying blade stiffness and mass

To further test the hypothesis that stiffness and frequency placement of the blade eigenfrequencies drive the stabilization, Fig. 4.13 compares stability maps for blades with varying stiffness and mass distribution. The rigid reference (solid line), case "1", the elastic blades with nominal stiffness and nominal mass distribution (K=100%, M=100%) as well as case "2", the blade with nominal mass and four times higher stiffness (K=400%, M=100%) have been taken from Fig. 4.12. Case "2" has a higher stiffness and eigenfrequency than case "1". Additionally, case "3" shows the stability map for blades with four times higher stiffness and mass (K=400%, M=400%). Because both mass and stiffness are scaled equally, the eigenfrequencies of the blades stay the same but with higher stiffness values. Comparison of case "3" to cases "1" and "2" allows the

separation of the effect of stiffness changes alone compared to combined stiffness and eigenfrequency changes. The stability boundary for case "3" should fall in between the ones for cases "1" and "2" if both stiffness and eigenfrequency drive stability, as for case "3" only one factor is altered. Again, as in Fig. 4.12, all blade stiffness and inertia terms are scaled equally. Further, to allow for a better comparison, the pylon-propeller system's total inertia (in all three directions) was kept constant when scaling the mass. Fig. 4.13 confirms the hypothesis: the stability boundary for case "3" ($\Delta\omega_{stab}$=-38%) falls exactly in between those of cases "1" ($\Delta\omega_{stab}$=-56%) and "2" ($\Delta\omega_{stab}$=-20%). This shows that the stabilization effect due to blade deflection (driven by pure stiffness) is of the same order as the stabilization due to blade frequency placing (which drives dynamic amplification).

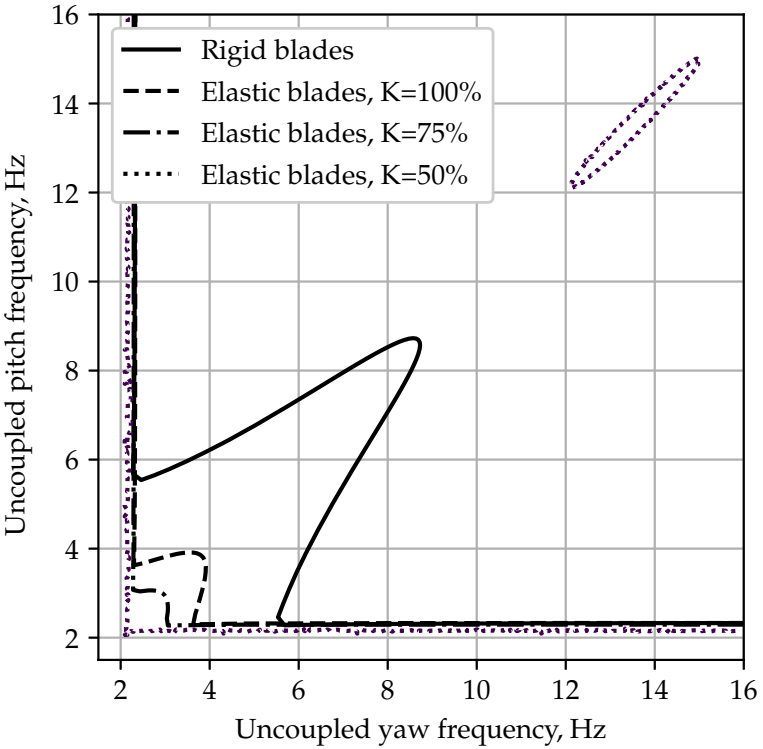

Figure 4.14.: Comparison of whirl flutter stability maps with low blade stiffness

The previous paragraphs showed a stabilizing influence of decreasing blade stiffness on whirl flutter stability. Fig. 4.14 demonstrates that there is a lower bound for the blade stiffness for this effect. If the blade stiffness is decreased further, new flutter mechanisms arise, e.g., due to the direct coupling of the blades and the pylon. The stability maps shown in Fig. 4.14 also contain one for the case with 50% nominal blade stiffness as a dotted line. In this case, the classical propeller whirl flutter region below the parabola on the bottom left is completely gone. Only the static divergence remains. However, a new region of unstable stiffness combination is found around 14 Hz uncoupled pitch and yaw frequency. The driving instability behind this region is most likely different from the classical backward whirl flutter. It is already known from the literature (compare, e.g., Johnston [36, Fig. 10]) that decreasing blade stiffness below a certain threshold changes the instability mechanism towards whirl flutter mechanisms as they occur on tiltrotor configurations, where direct dynamic coupling between the rotor and pylon modes dominate the stability behavior. The blade stiffnesses considered here are unrealistic for propeller aircraft propellers. The TM-method is also not ideally suited to investigate these types of couplings due to the lack of blade DOF in the eigenvectors. Fig. 4.14 served two purposes in this thesis, though: First, it showed that there is a boundary for decreasing blade stiffness, from which the system becomes unstable again. Second, it proved that the TM-method can detect these instabilities, although it does not give enough insights into the exact coupling mechanisms.

Including blade elasticity in propeller whirl flutter prediction stabilizes flutter predictions, as shown in the literature and reproduced here in the frequency domain using the proposed TM-method. The stabilization is driven by the blade stiffness due to the deflection of the blade under the aerodynamic forcing and by the distance between blade eigenfrequencies and the rotational speed due to dynamic amplification of the aerodynamic forcing. Blade elasticity could, therefore, be used as a design parameter to mitigate whirl flutter. Still, two things must be kept in mind: First, there is a lower bound of blade stiffness, below which the system becomes more unstable again. Second, only the effect of blade elasticity on whirl flutter stability has been considered here, neglecting impacts on other disciplines such as loads or performance. However, including the existing blade elasticity changes stability predictions towards lower engine support stiffness requirements or higher flutter speeds, which is worth considering in the propeller aircraft design process. The TM-method allows these effects to be considered in the frequency-domain flutter process.

4.3. Comparison of unsteady aerodynamic methods

In the previous sections, the aerodynamic method used for all investigations was kept the same to verify the TM-method and compare the influence of blade elasticity without additional influence from the aerodynamic method. The method chosen was the unsteady strip theory with Wagner's function (see Tab. 2.2). This section presents a comparative study on the influence of different aerodynamic methods on predicting transfer matrices and whirl flutter stability. All other parameters (TM-method settings, blade elasticity) are kept constant as in the previous sections. The propeller blades are assumed to be rigid to facilitate further comparison with the Houbolt/Reed method. The investigations are partly published in [75], but using a different pylon system and including more results from different mid-fidelity methods. This section only contains the results contributed by the author.

The first subsection deals with the comparison of the predictions of the different methods listed in Tab. 2.2 regarding unsteady aerodynamics and whirl flutter stability for a windmilling operating condition, while the second subsection highlights the influence of the trim state.

4.3.1. Windmilling Condition

This subsection first examines the predictions of the different aerodynamic methods for the hub load response to propeller disc pitch. The quasi-steady response, the 1P hub loads, are compared in Fig. 4.15. They resemble the linear transfer function from a steady disc pitch angle[17] to the in-plane hub loads. All methods from Tab. 2.2 are listed by descending magnitude of the in-phase components. The aspect ration correction is neglected for the Houbolt/Reed methods (quasi-steady (QS) and unsteady) for better comparison with their strip-theory equivalent. The top two plots in Fig. 4.15 present the two in-plane force components, and the bottom plots the corresponding moments. The right two plots list the in-phase components, which are of higher magnitude than the corresponding out-of-phase components in the left two plots. Comparing the two quasi-steady methods (identified Quasi-steady and Houbolt/Reed QS) reveals a good match in amplitudes of the in-phase terms, with the identified ones approx. five percent higher.

[17] In this case, computed for 1°disc pitch angle.

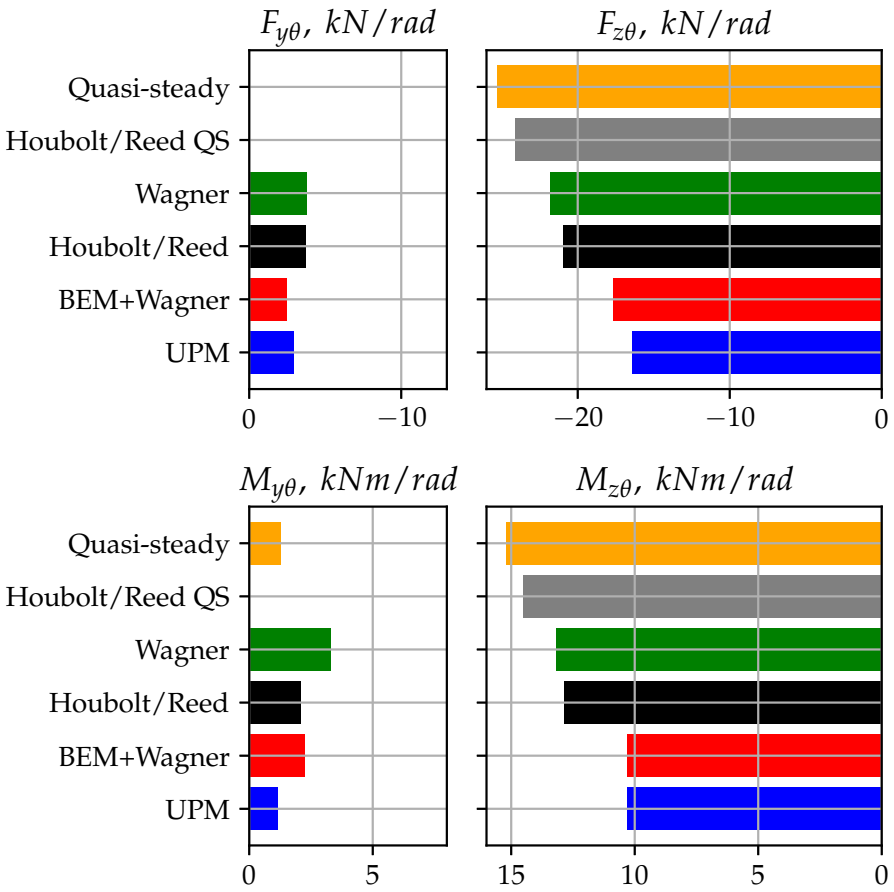

Figure 4.15.: Comparison of in-plane loads of the propeller under steady disc pitch between different aerodynamic methods

The out-of-phase components are zero due to a lack of lift-lag, which produces an anti-symmetric response of the blade lift (compare explanation to Fig. 4.9). The only exception is $M_{y\theta}$ for the quasi-steady version of the time-domain strip theory (named Quasi-steady) because the airfoil moments are considered in this method and neglected in the Houbolt/Reed method. The airfoil moments reach their maxima together with the unsteady lift at 90°and 270°, adding up to a global moment about the y-axis. The comparison between the time-domain and Houbolt/Reed versions of the strip theory is also similar for the unsteady versions (Wagner and Houbolt/Reed). For these, the amplitude of the in-phase components is reduced due to the lift lag by twelve to fifteen percent depending

on the component. The out-of-phase components are increased compared to their quasi-steady equivalents. The difference in $M_{y\theta}$ due to the missing airfoil moment in the Houbolt/Reed theory can also be observed here. Comparing the strip theory with and without the induced velocity model (BEM+Wagner and Wagner) reveals a general reduction in the predicted aerodynamic loads when induced velocity is considered. $M_{z\theta}$, for example, is reduced by 22% in the BEM+Wagner result compared to the Wagner result without induced velocities. The dampening effect of the induced velocities on the unsteady angle of attack on the blades explains this. In disc sections that produce more lift (up-stroke), more circulation is shed to the wake, and more velocity is induced on the propeller disc, leading, in turn, to a reduction in the local angle of attack. The same but vice-versa applies for disc sections with less lift (down-stroke). BEM+Wagner is the most complete analytical model, generally showing a good match with the prediction of UPM, the 3D panel method. The remaining differences (e.g., about seven percent in $F_{z\theta}$ and almost 50% in $M_{y\theta}$) can be attributed to 3D effects like better tip-loss modeling and a different prediction for the airfoil moments. The differences in 1P hub load predictions between UPM and BEM+Wagner are in the same range as those between different mid-fidelity methods [75]. The weighted BEM approach helps with this fit, as the pure element-wise formulation under-predicts aerodynamic forces, while the ring-wise approach over-predicts them [75].

Fig. 4.16 extends the method comparison to the prediction of unsteady hub load transfer functions. As before, only the response to propeller disc pitch is shown, here up to 20 Hz perturbation frequency. The four hub load components are split into real (solid line) and imaginary (dashed line) part. The real part represents the aerodynamic stiffness (compare sec. 2.2.3). The slope of the imaginary part represents the aerodynamic damping components. The transfer functions from the Houbolt/Reed methods are omitted to make space in the plot as they are linear anyway. The transfer functions from UPM were identified using harmonic excitation, and the others were identified using pulse excitation. The transfer functions from the quasi-steady strip theory (orange) also show a linear behavior. The frequency-dependency in the other transfer functions (especially in the real part) stems from unsteady aerodynamics. In general, the shape of the frequency-nonlinearity (compare, e.g., the decrease in the real part of $F_{z\theta}$) is comparable between the methods, only an offset equal to the difference in the 1P hub loads can be observed[18]. Regarding the amplitudes of aerodynamic stiffness and damping, the results are similar as for Fig. 4.15: Quasi-steady transfer functions (orange) are predicted larger than those from unsteady Wagner theory (green) due to the lift-lag effect, and the additional induced velocity model in the BEM+Wagner-method (red) and UPM (blue)

[18] The transfer function for zero frequency is equivalent to the 1P hub load from Fig. 4.15.

further reduces amplitudes. Again, the fit between UPM and BEM+Wagner is good, especially for the real part of $M_{z\theta}$ and the aerodynamic damping terms in $F_{y\theta}$ and $M_{y\theta}$.

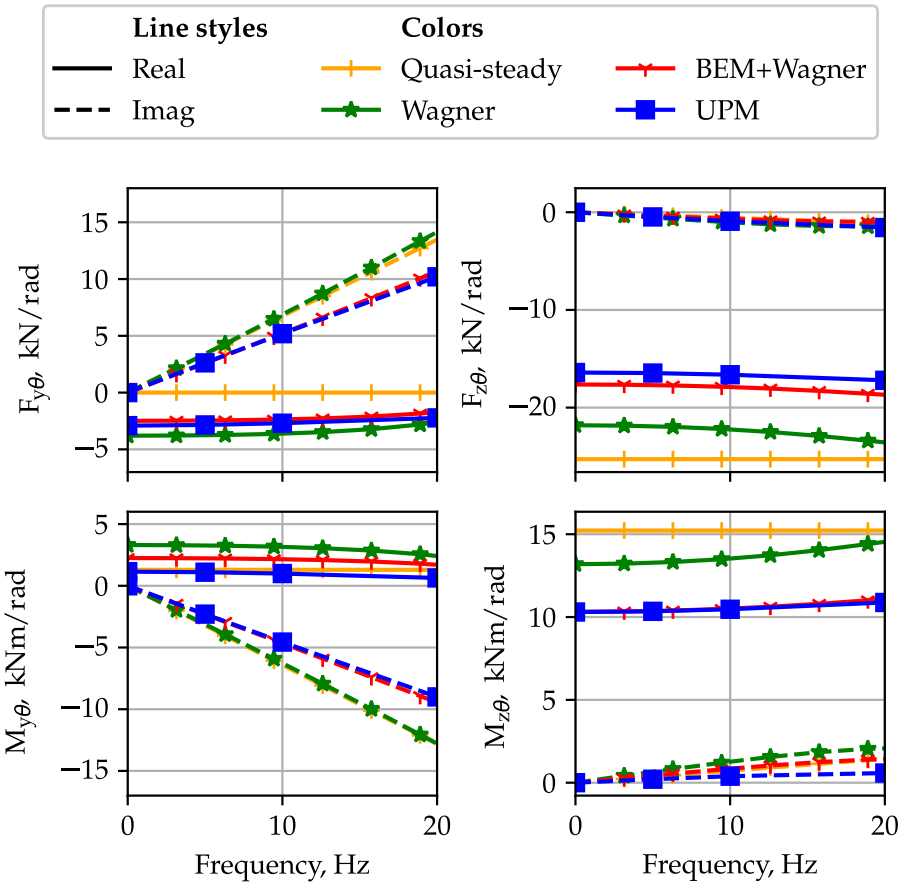

Figure 4.16.: Comparison of transfer matrices for the rigid propeller and computed with various aerodynamic methods

The transfer functions are linearized into aerodynamic derivatives according to section 2.2.3 to further investigate the differences in aerodynamic stiffness and damping and facilitate a more quantitative comparison between the methods. The reference frequency was chosen at 10 Hz, and only the real part of the derivatives was retained. Fig. 4.17 compares the four derivatives for the aerodynamic stiffness in the left column and the corresponding damping derivatives in the right column. In this case, the notation is equivalent to the Houbolt/Reed derivatives (compare section 2.2.2). The derivatives from the Houbolt/Reed method are also listed, and the value of the unsteady Houbolt/Reed theory is marked with a horizontal dashed line for reference. The sorting of the individual plots is the same as in Fig. 4.15, so with descending magnitude of the in-phase stiffness components ($C_{z\theta}$ and $C_{n\theta}$ in this case). Comparing the magnitude of the different derivatives with each other shows the same pattern as observed before. The in-phase components ($C_{z\theta}$, C_{yq}, $C_{n\theta}$ and C_{mq}) are larger in magnitude than the out-of-phase components. The variation between the different methods is higher for the out-of-phase components, which depend on the unsteady aerodynamic model and the airfoil moment (both differ between the methods). As for the 1P hub loads, the magnitude of the in-phase damping components (C_{yq} and C_{mq}) are predicted higher by the quasi-steady and unsteady strip theory and reduced by induced-velocity effects in BEM+Wagner and UPM predictions. One noticeable discrepancy between UPM and BEM+Wagner prediction is for $C_{m\theta}$, where BEM+Wagner predicts a 50% higher value. According to Fig. 2.5, this should not affect stability predictions much as the sensitivity for this component is low. The influence, if detectable, is stabilizing for BEM+Wagner. Noticeable differences between all the methods also occur for the smallest derivative, C_{nq}, where all time-domain methods even predict a different sign than the Houbolt/Reed method due to missing consideration of the airfoil moment in the latter. The "smallness and the lack of experimental correlation" [14] of C_{nq} was already stated in literature, and therefore, C_{nq} (and also C_{zq}) are sometimes set to zero in literature.

The comparison of the unsteady aerodynamic predictions from the different methods reveals a pattern: Quasi-steady methods predict higher aerodynamic forces than unsteady, and modeling induced velocities on the propeller disc reduces loads further. The two most detailed methods (UPM and BEM+Wagner) match well for most components. Only small offsets in individual components remain due to different tip-loss and airfoil moment modeling.

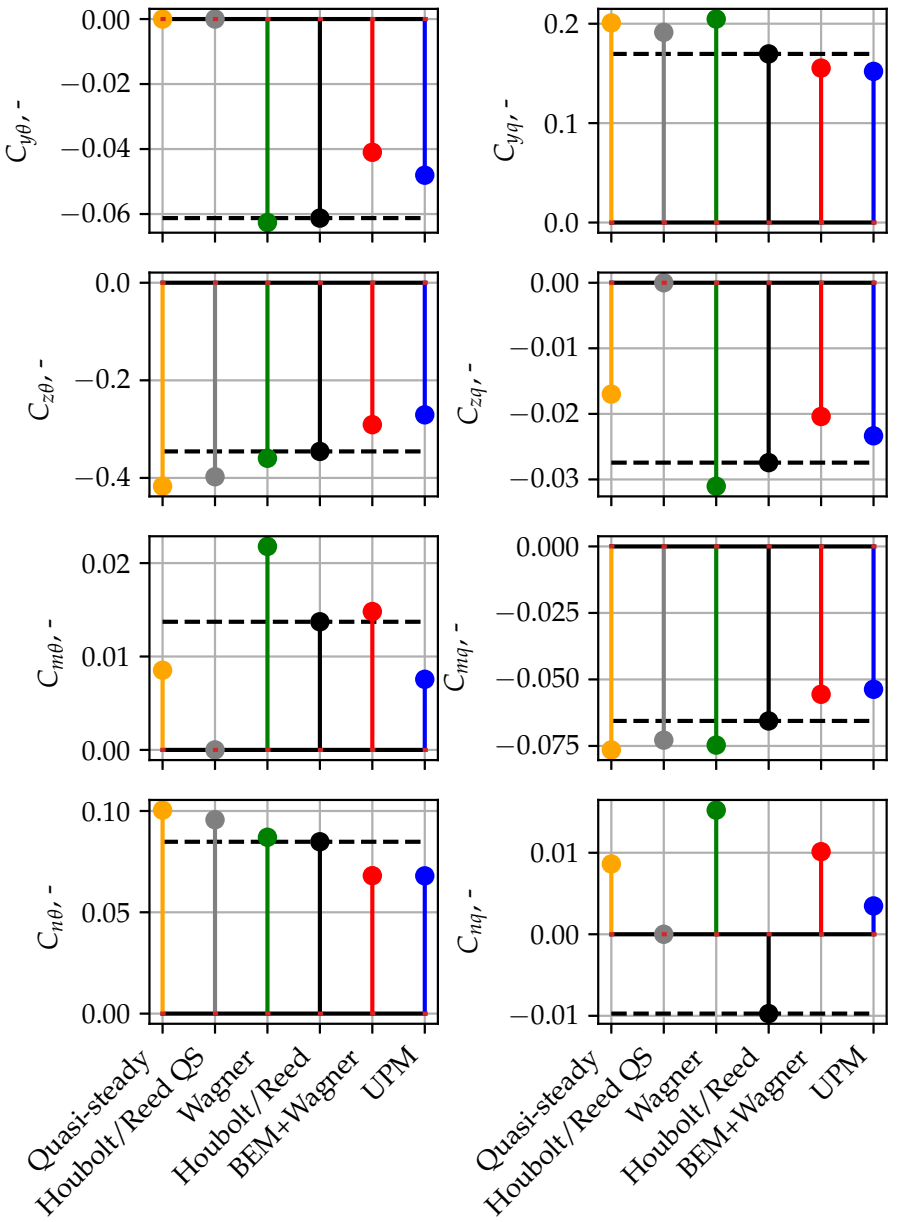

Figure 4.17.: Comparison of the linearized propeller derivatives between the different aerodynamic methods

To compare the effect of different aerodynamic modeling on whirl flutter stability, the frequency-dependent transfer matrices[19] are used to compute whirl flutter stability maps for the simplified pylon system. The top plot of Fig. 4.18 compares the maps for the simplified pylon system used before. The insert axes show parts of the tip of the whirl flutter region enlarged for better comparison. The grey and orange lines represent the two quasi-steady methods (Houbolt/Reed and time domain). These two methods predict the most unstable system regarding the extent of the whirl flutter region. The most stable prediction is given by Wagner strip theory (green line), closely followed by unsteady Houbolt/Reed (black) and BEM+Wagner, which provide almost identical predictions for this system. Stability maps with UPM aerodynamics show a larger extent but are still smaller than the quasi-steady methods. At first sight, this does not fit to the predictions from unsteady aerodynamics, where BEM+Wagner and UPM showed a good match and, e.g., Wagner strip theory over-predicted aerodynamic loads, especially the destabilizing $M_{z\theta}$. The explanation lies in the different sensitivities of the system's stability to the individual aerodynamic stiffness and damping derivatives. A general over-prediction increases the stabilizing components along with the destabilizing ones and does not affect overall whirl flutter stability as much as a difference in a single component (e.g., a significant difference in the slightly stabilizing $C_{m\theta}$ between BEM+Wagner and UPM). The more significant differences in all derivatives to the Wagner method cancel each other out in this case. These findings can not be generalized regarding which method shows more or less stable predictions compared to the others. Different structures weigh the force and moment components differently. This is demonstrated by the two plots on the bottom of Fig. 4.18, for which the distance between the pivot point and the propeller plane was doubled (left plot) or halved (right plot). For the shorter pylon, the moment coefficients dominate the generalized propeller forces (as the forces are multiplied by a shorter distance in $\underline{\Phi}_{prop}$). Therefore, the lower prediction of the stabilizing moment $C_{m\theta}$ in UPM yields an even more unstable system. This fits to findings in the literature: Gennaretti and Greco found that for their system with a pivot to radius ratio $a/R = 0.3$, their panel free-wake methods predicts a more unstable system even compared to the quasi-steady strip theory [30, Fig. 12][20]. On the other hand, on the bottom left of Fig. 4.18, stability maps with UPM aerodynamics are the smallest for the longer pylon. For the longer pylon, the results with the quasi-steady methods fall outside of the plot at higher pylon uncoupled frequencies [75].

[19] Not their linearization!

[20] Note: their investigation is at a slightly higher advance ratio, $\mu = 1.0$, compared to this investigation at $\mu = 0.67$.

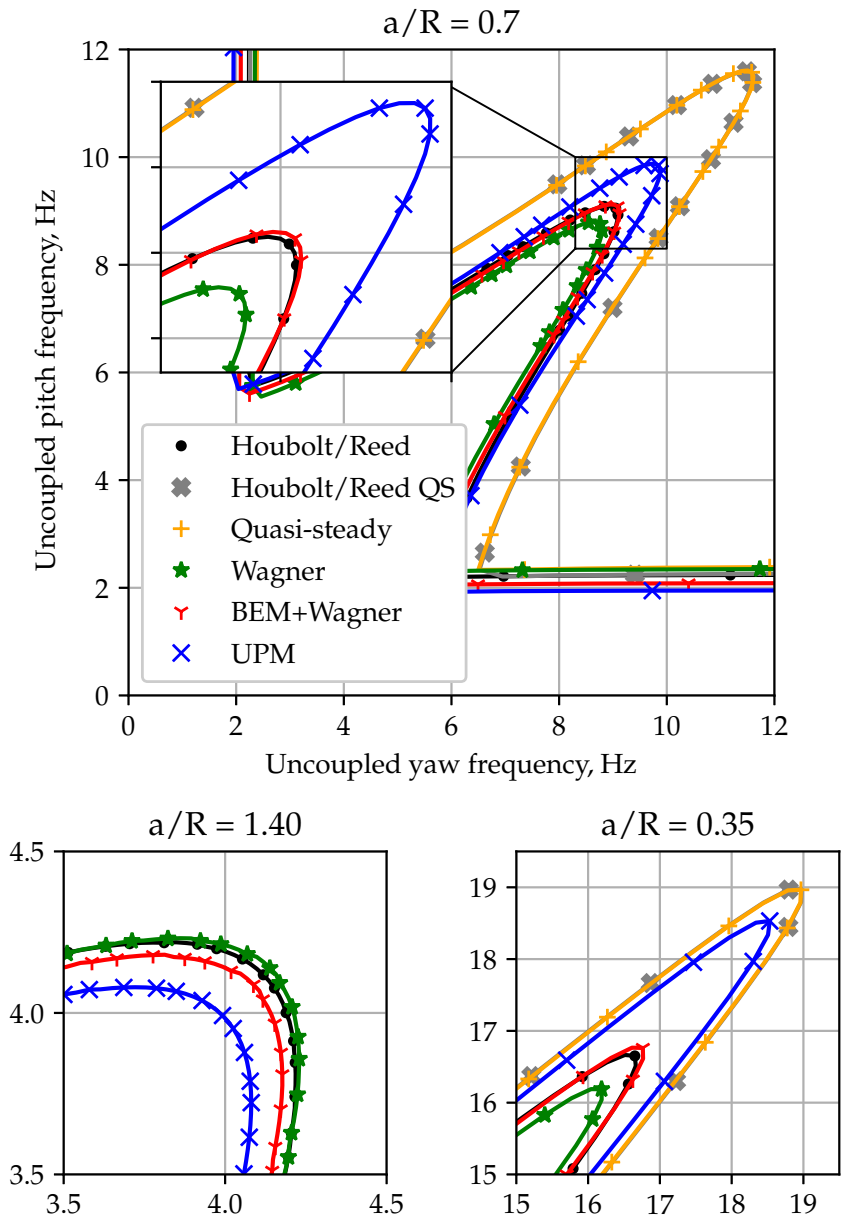

Figure 4.18.: Comparison of whirl flutter stability maps for three pylon lengths and between the different aerodynamic methods. For the bottom left plot, the quasi-steady results are out of range at higher frequencies.

This means no clear trend regarding the effect of propeller aerodynamic modeling on whirl flutter stability can be derived from the results with the simplified pylon system. The main finding is the system's high sensitivity to small relative changes of the individual components, opposed to a low sensitivity to the overall scaling of the loads. Choosing a better or worse method for stability prediction is impossible without a high-fidelity or experimental reference. Until a validation case is set up, great care should be taken when modeling real aircraft propellers, and as many aspects as possible (induced velocities, unsteadiness, airfoil moment, tip loss) should be considered.

4.3.2. Powered Condition

The last subsection compared predictions of different aerodynamic methods for unsteady propeller aerodynamics and whirl flutter stability. The trim condition chosen for this was the windmilling trim to allow a better comparison with the Houbolt/Reed method. This subsection deals with the influence of the trim condition on the transfer matrices and whirl flutter stability. Only results calculated with the mid-fidelity method UPM are shown. The differences are representative of other aerodynamic methods.

Fig. 4.19 compares the transfer functions regarding disc pitch angle for the windmilling (black lines) and powered (grey lines) case. In windmilling, the propeller blade pitch angle is adjusted to yield zero torque about the propeller axis and, therefore, zero power. The blade pitch is increased for the powered case until the power required to drive the propeller reaches 500 kW, a realistic maximum continuous power for a representative turboprop engine of this size. Comparing the transfer functions between the two trim conditions reveals two main differences. The magnitude of the real part of $F_{z\theta}$ increases in the powered case due to the tilting thrust vector. When the propeller rotates about the global y-axis, the steady thrust vector rotates with it (compare Fig. 4.20). This produces a vertical force component in the negative z-direction, increasing the aerodynamic transfer function in this direction (top right plot) by the amplitude of the thrust vector. The same applies to the global torque vector, which produces a negative $M_{z\theta}$, reducing the amplitude of the real part of the transfer functions (bottom right plot). Not shown in this plot is the amplitude offset in the real part of M_{zy}. This is also caused by the steady thrust vector, which, when moved in the y-direction, has an offset to the global z-axis and causes a moment component about the z-axis. For the simplified pylon system, the changes in $F_{z\theta}$ and M_{zy} caused by the thrust vector cancel each other in the generalized propeller forces because the thrust vector always moves on an axis pointing through the pivot point and hence can not do work on the system. On the other hand, the decrease in $M_{z\theta}$ directly stabilizes the system

by reducing the destabilizing component. The other transfer functions either stay the same or show minor changes (e.g., aerodynamic damping in $F_{y\theta}$) caused by the different steady angles of attack on the blades.

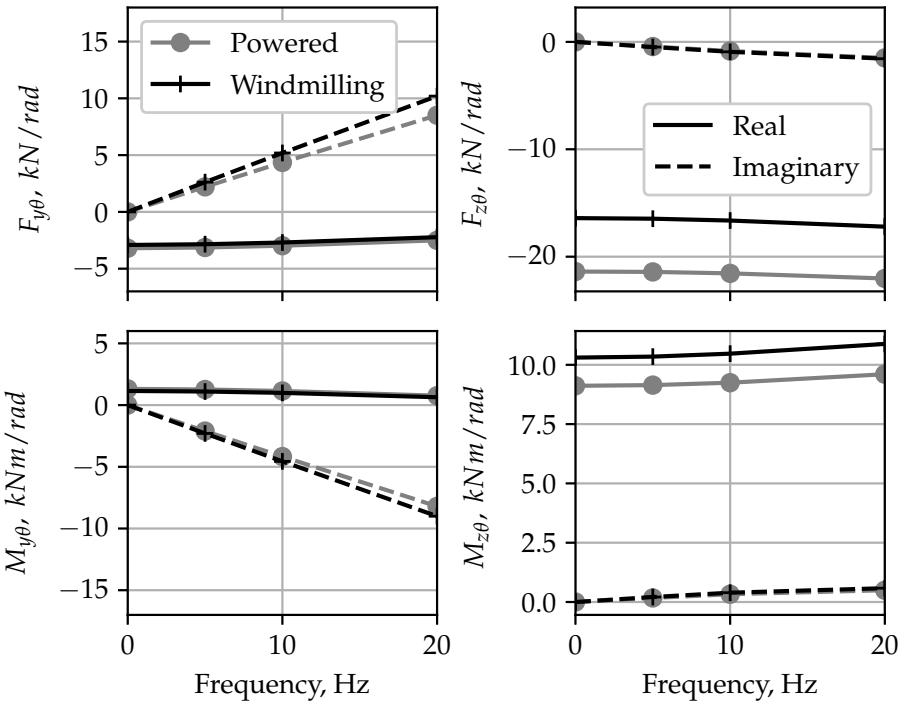

Figure 4.19.: Comparison of transfer matrices for the rigid propeller in different trim conditions

Fig. 4.21 compares the whirl flutter stability maps for the simplified pylon system for the windmilling and the powered case. From the transfer matrices in Fig. 4.19, the hypothesis is that the powered case should be more stable than the windmilling case. This hypothesis is consistent with statements in literature [4]. Fig. 4.21 confirms this hypothesis: the powered case is almost 20% more stable concerning whirl flutter in terms of uncoupled pitch and yaw frequency. Static divergence is almost not affected, as the thrust force effects cancel out for the system.

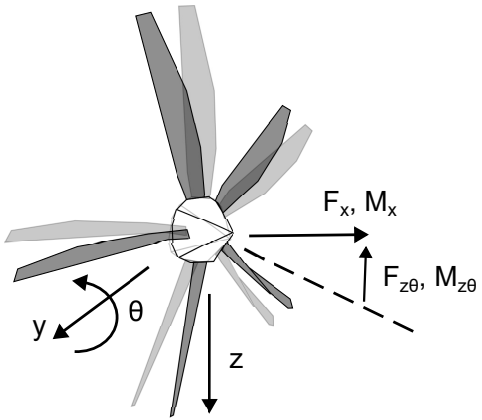

Figure 4.20.: Sketch of the tilting propeller, including the tilting thrust and torque vector

The stabilizing effect of power (or, better, torque) is known from literature and is confirmed here using rigid propeller transfer functions using mid-fidelity aerodynamics. The stabilizing influence can be reproduced with low-fidelity aerodynamics [75] and flexible blades [74].

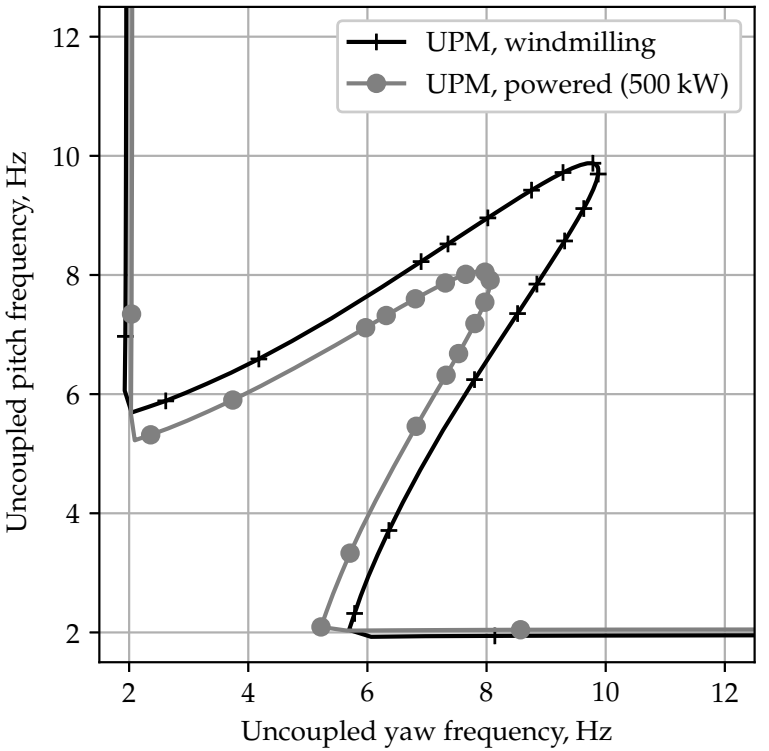

Figure 4.21.: Comparison of whirl flutter stability maps for the rigid propeller in windmilling and powered condition

4.4. Application to full aircraft model

Up to this point in this thesis, the simplified pylon system was used for all whirl flutter analyses. The following section extends the findings regarding the influence of blade elasticity and aerodynamic modeling gained with the simplified pylon system to the full aircraft model described in section 3.2.2. First, the flutter results obtained with the classical Houbolt/Reed method are examined in detail, including the description of the two flutter modes of interest. After this, the effect of propeller modeling using the TM-method is analyzed by comparing the frequency and damping predictions for the two critical modes with varying blade elasticity and aerodynamic modeling. The results are published in two conference papers with contributions of the author [76, 77] and are reproduced here for a slightly different propeller configuration (J_p and $C_{l\alpha}$ of the propeller differ).

Fig. 4.22 presents the frequency and damping of the first 25 elastic modes of the full aircraft configuration over a range of airspeed from zero to 170 m/s. In total, 50 modes, including six rigid body modes, were considered for the flutter analysis. Still, both the rigid body modes and the higher frequency modes are not shown in Fig. 4.22 as they are not of primary interest and to obtain readable plots. Classical Houbolt/Reed propeller modeling for the two propellers with clock-wise rotational sense has been used, neglecting the aspect ratio correction. Unlike the previous analysis, a constant speed trim to zero power (windmilling) was used. To ease the mode-tracking in the lower speed range, the rotational speed was ramped up slowly from a standstill to full speed between zero and 32 m/s. All analyses have been conducted with incompressible aerodynamics both for the DLM- as well as for the propeller aerodynamics. Aerodynamic interaction between propeller and wing has been neglected according to the assumptions of this thesis. Analyses were conducted using the g-method.

Because the aircraft model is tuned to show whirl flutter within the envelope, Fig. 4.22 shows two modes that become unstable in the speed range analyzed. Modes nine (blue '+'-markers) and ten (red stars) are highlighted and become unstable at 127.5 m/s and 163 m/s respectively. The flutter mechanism behind the instability of mode ten is a coupling between symmetric engine pitch, symmetric wing torsion, and antisymmetric engine yaw (the latter with 90 deg phase shift), as Fig. 4.23 shows with four global pictures of the complex eigenvector during one mode cycle. The coupling of symmetric engine pitch and anti-symmetric engine yaw leads to an anti-clockwise (or backward) whirling motion of the propeller hub, with the pitch motion being in phase. Due to the coupling between engine pitch and wing torsion, the wing also undergoes a torsional motion (compare t=0.5T in Fig. 4.23).

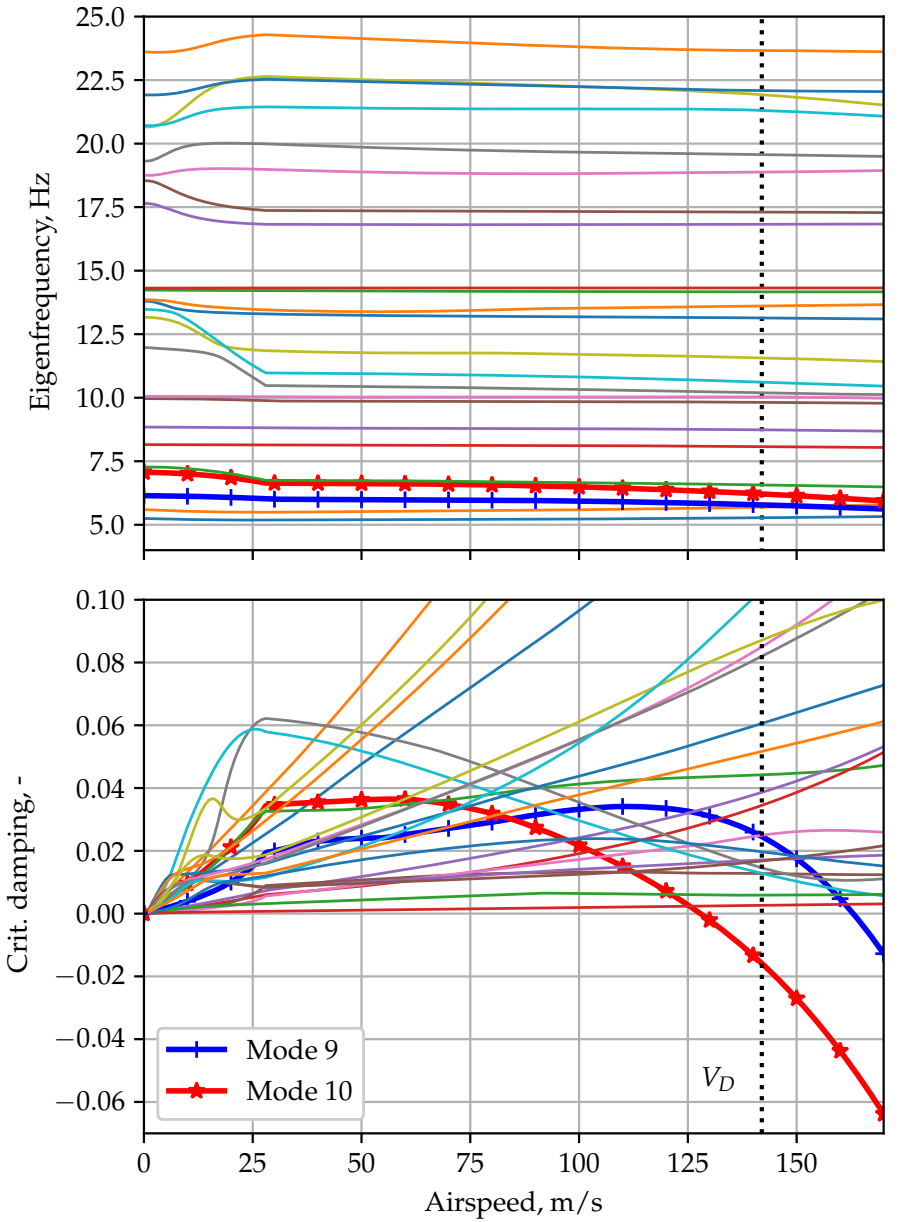

Figure 4.22.: Flutter results of the full aircraft model using Houbolt/Reed propeller transfer matrices

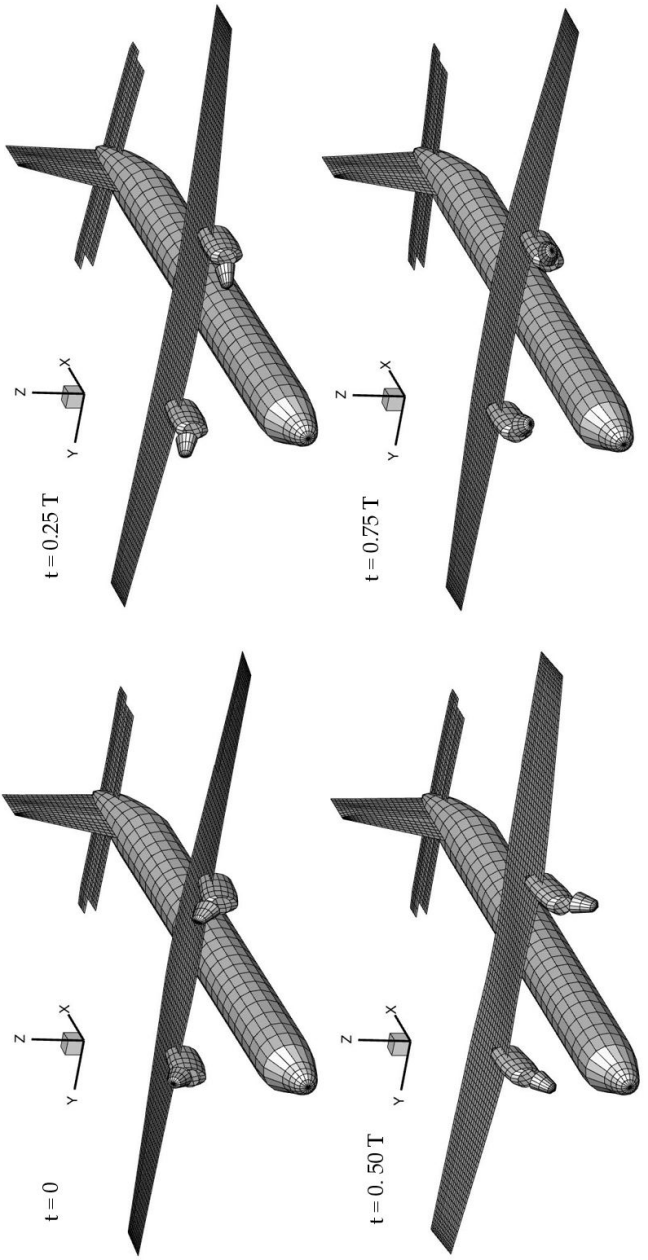

Figure 4.23.: Complex flutter eigenvector (at zero damping) for mode 10

The flutter mechanism behind the instability of mode 9 is the out-of-phase equivalent of mode 10. The coupling is between anti-symmetric engine pitch, anti-symmetric wing-torsion, and symmetric engine yaw. Again, both propeller hubs undergo a backward whirling motion (compare Fig. 4.24), but in this case, with approximately 180°phase difference in the pitch. Like the first instability, anti-symmetric wing torsion is involved due to coupling with the engine pitch. Both flutter couplings can not be categorized as purely symmetric or anti-symmetric due to the asymmetry imposed by the rotational sense of the two propellers. Both instabilities are classical backward whirl flutter mechanisms. The remaining modes all stay stable within the investigated range of airspeeds. The ramping up of the engine rotational speed causes the significant changes in frequency and damping at low airspeeds. Due to the constant speed trim, the engine gyroscopics are already fully present at low speeds and induce changes in frequency. The rotational speed is slowly ramped up to ease the mode-tracking back to the structural mode shapes, so results below 32 m/s are not physical. The low speeds are not crucial for the flutter assessment as flutter occurs mainly at high airspeeds.

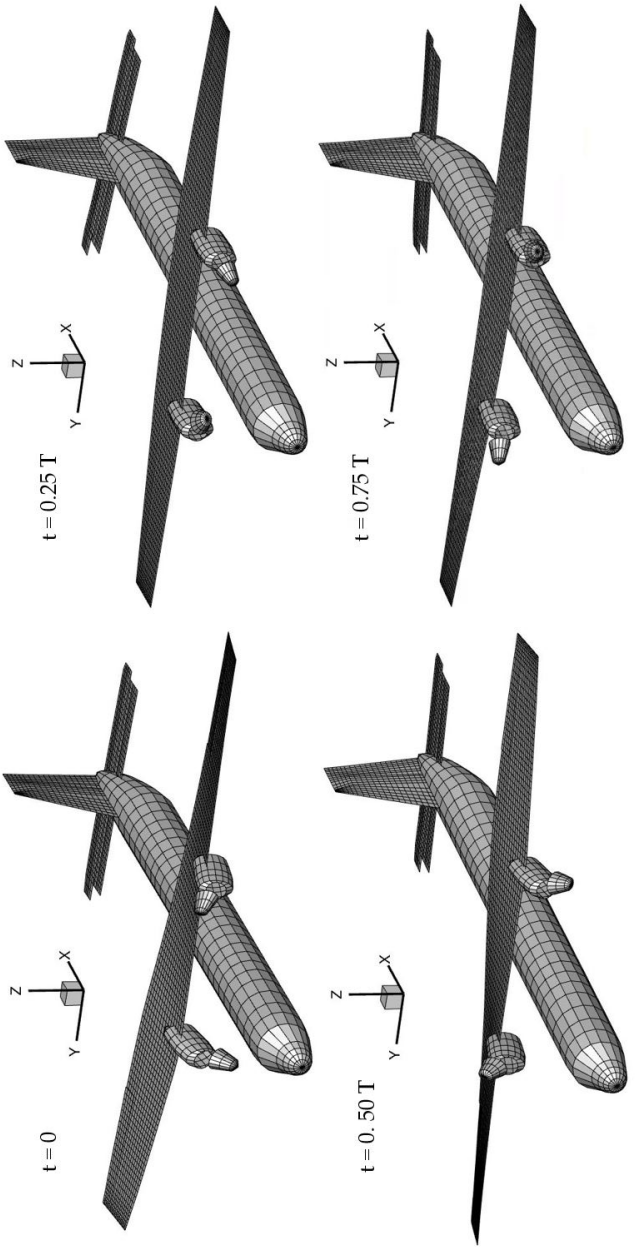

Figure 4.24.: Complex flutter eigenvector (at zero damping) for mode 9

The following two figures explore the sensitivity of the two flutter couplings described in the last paragraph to propeller modeling. First, Fig. 4.25 investigates the effect of blade elasticity on the frequency and damping of modes nine and ten. Second, Fig. 4.26 shows the frequency and damping of the two whirl modes for the rigid propeller analysis using different methods for the propeller aerodynamics.

Fig. 4.25 shows the frequency and damping trends for modes nine and ten only, which are those becoming unstable in the Houbolt/Reed analysis from Fig. 4.22. Mode nine is shown as blue lines with a "+" marker, and mode ten is shown as red lines with "star" markers. For each mode, three different results are presented: the Houbolt/Reed results from Fig. 4.22 as a reference (solid lines), the results using rigid propeller blades and Wagner aerodynamics using the TM-method (dashed lines) and the frequency and damping for the analysis with flexible propeller blades and Wagner aerodynamics (dotted lines). The aeroelastic airframe model is the same for all analyses. Frequency and damping were computed between 0 and 170 m/s in steps of 1 m/s. The transfer matrices were calculated on 21 equidistant velocity points and interpolated linearly over the velocity range. The constant-speed trim was used as in Fig. 4.22. In section 4.2, the results obtained with the Houbolt/Reed propeller model and the rigid blade transfer matrices were shown to be very similar, while the results with elastic blades were drastically stabilized. The results from 4.25 confirm these findings also for the more complex full-aircraft model. The frequency and damping results for Houbolt/Reed and rigid blade transfer matrices are very close, with the Wagner aerodynamics in the TM-method results giving a slightly higher flutter speed. However, the elastic blade results in the dotted lines differ again considerably from the rigid blade results. The damping trends stay positive over the airspeed range, and no trend toward whirl flutter can be seen. All other modes (not shown in Fig. 4.25) stay stable, too, so with elastic blades, the configuration shown is free from flutter up to at least 170 m/s. Due to the decreased negative stiffness terms in the transfer matrices with elastic blades (compare Fig. 4.8), the frequency of modes nine and ten is slightly higher for the elastic blade case. It can be concluded that the stabilizing influence of blade elasticity on whirl flutter can be reproduced on a full-aircraft level and is not an artifact of the simplified pylon system.

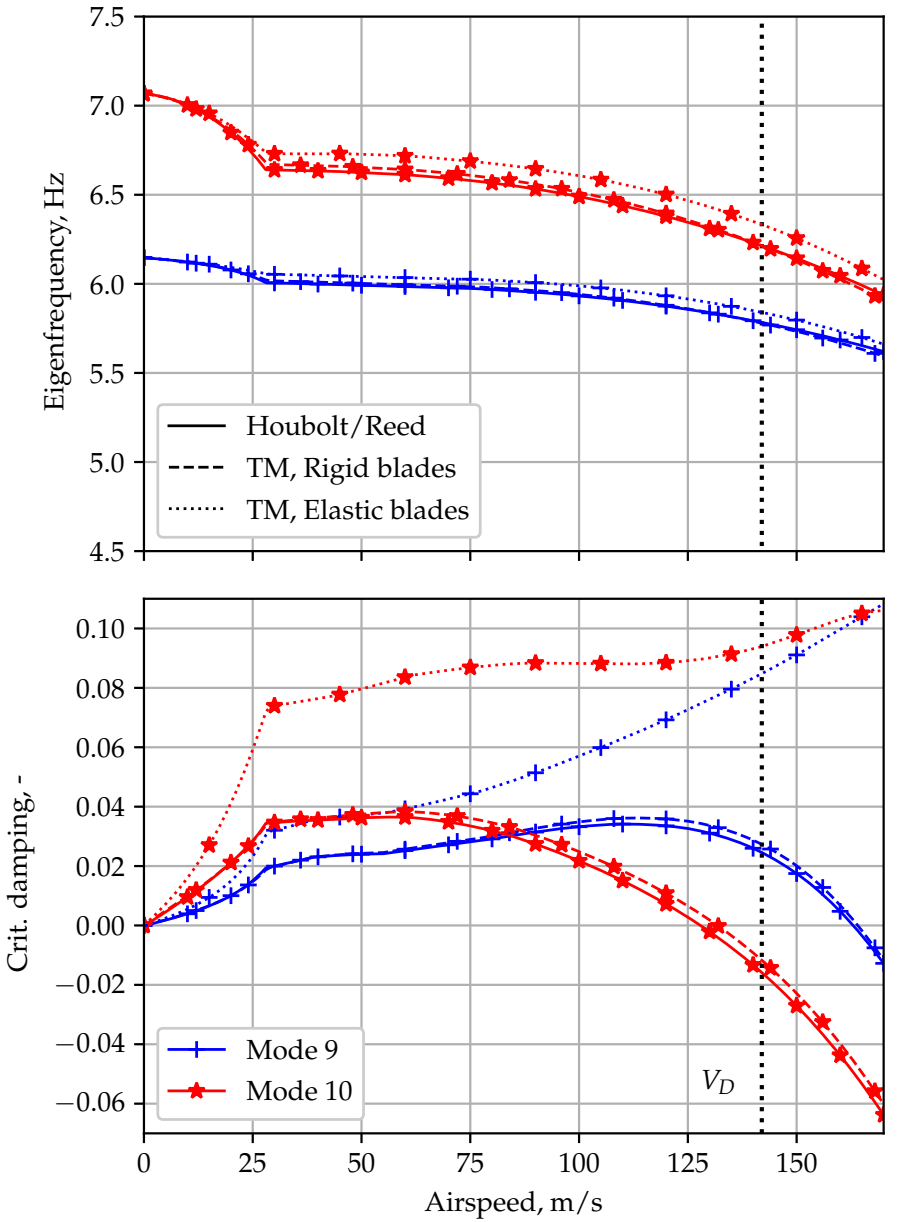

Figure 4.25.: Comparison of the frequency and damping trends for the unstable modes between Houbolt/Reed and rigid and flexible blade TM-method results.

While Fig. 4.25 shows results for varying blade elasticity and a fixed aerodynamic model, Fig. 4.26 presents results from a study with rigid blades and varying blade aerodynamics. For the same airframe setup as in the previous plots, five aerodynamic methods are compared: Houbolt/Reed (solid lines), low-fidelity Quasi-steady (dotted) and Wagner (dashed) aerodynamics without induced velocities as well as BEM+Wagner results (dash-dotted) and mid-fidelity UPM results (dash-dot-dotted). The transfer matrices have been computed for operating points at five different airspeeds (0.25, 0.5, 0.75, 1.0, and 1.2 times dive speed V_D) with the constant-speed windmilling trim. The increased spacing of the operating points is possible due to the more linear behavior of the rigid blade transfer matrices (compare, e.g., Fig. 4.4 and Fig. 4.1). The interpolation over the airspeed range was conducted using cubic polynomial interpolation. As in Fig. 4.25, only the frequency and damping trends for the two unstable whirl modes nine and ten are shown. From the damping plot (lower plot in Fig. 4.26), it can be seen that quasi-steady aerodynamic modeling yields the most unstable results, with flutter speeds almost twenty percent lower than the Houbolt/Reed results. The results with Wagner aerodynamics are close to the Houbolt/Reed results, as Fig. 4.25 already showed. The results from the methods with induced velocity modeling (BEM+Wagner and UPM) display higher flutter speed and match closely for mode ten. For mode nine, the flutter speeds of the latter two methods are outside of the covered airspeed range but show more significant discrepancies compared to mode ten for the damping trends. These differences between the modes and the higher flutter speed compared to Houbolt/Reed highlight the results from section 4.3 and stress the sensitivity of the problem with regard to the flutter mode shape and the airframe model in general. In the case of the full aircraft configuration, additional stabilizing terms are present in the equations of motion in the form of unsteady wing aerodynamics. This makes the sensitivity of the system smaller regarding the stabilizing propeller transfer functions (e.g., $F_{y\theta}$ and $F_{z\theta}$), as in the flutter point the destabilizing moment term $M_{z\theta}$ is balanced by the wing aerodynamic damping and the stabilizing propeller terms together. Hence, the absolute value of the destabilizing term is more important here, which is why the aeroelastic stability (expressed by the value of the flutter speed) correlates better with the magnitude of the propeller transfer functions (compare, e.g., $M_{z\theta}$ in Fig. 4.15). When looking at the frequency trends (upper plot in Fig. 4.26), the more prominent changes in frequency at lower airspeeds are again due to the slow increase in gyroscopics and not physical. The results with quasi-steady propeller aerodynamics predict the lowest frequencies at higher airspeeds, while those with transfer matrices from UPM predict the highest. This is again due to the higher negative stiffness terms for the Quasi-steady method, which can already be seen in the higher amplitudes, e.g., in the 1P hub loads (compare Fig. 4.15).

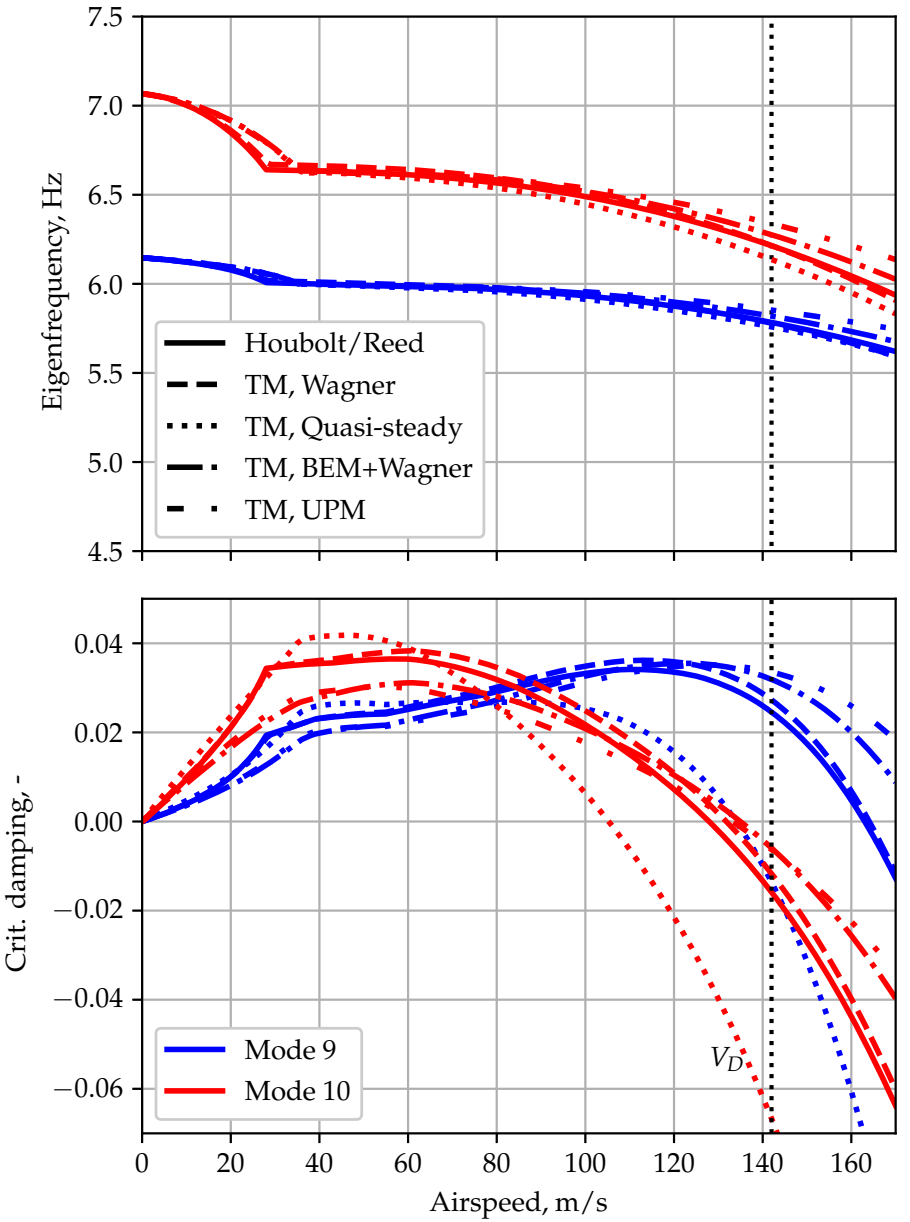

Figure 4.26.: Comparison of the frequency and damping trends for the unstable modes between different aerodynamic methods for the propeller transfer matrices

Tab. 4.1 compares the flutter speeds of modes nine and ten from Fig. 4.22 to Fig. 4.26 in true airspeed and relative to the Houbolt/Reed results (percentages). The figure from which the values are obtained is listed in the first column, and the flutter speeds for modes nine and ten are listed in the last two columns. The comparison shows the destabilizing influence of quasi-steady aerodynamics, as the flutter speeds of the Quasi-steady method are 18% lower compared to the Houbolt/Reed results. The three other aerodynamic methods lie one to six percent higher than the reference. The flutter speeds for Mode 9 and BEM+Wagner and UPM aerodynamics are marked as higher than 170 m/s, as no flutter crossing was found, but a clear trend towards whirl flutter exists. On the other hand, for the elastic blade modeling in the last column, no results have been given as no trend towards whirl flutter was found in the given airspeed range.

Table 4.1.: Flutter speed predictions of the generic turboprop model using different propeller modeling

		Flutter speed, m/s (%)	
Figure	Propeller-modeling	Mode 9	Mode 10
4.22	Houbolt/Reed	163.0 (100%)	127.5 (100%)
4.26	TM, Quasisteady	133.9 (82%)	105.0 (82%)
	TM, Wagner	164.0 (101%)	131.3 (103%)
	TM, BEM+Wagner	$>$ 170.0 ($>$105%)	135.0 (106%)
	TM, UPM	$>$ 170.0 ($>$105%)	133.2 (104%)
4.25	TM, Wagner, Elastic blades	-	-

Tab. 4.1 summarizes the results from this section and the whole parameter studies in this thesis: While propeller aerodynamic modeling does influence stability predictions, which partly depends on the mode shape, the effect of blade elasticity on whirl flutter stability is much higher and so far always found to be stabilizing. Without validation results from experiments or high-fidelity numerical simulations, none of the modeling approaches can be considered conservative or non-conservative.

5 Conclusion

To conclude this thesis, the last chapter summarizes the key contribution of this work to the state of the art. Afterward, the method and the results are discussed in a broader context, pointing out advantages over existing methods and discussing the potential impact of the limitations of this work. Alongside this discussion, recommendations for further work are given.

5.1. Key contribution

This thesis contributes a new method for frequency-domain whirl flutter analysis of propeller aircraft. The Transfer-Matrix method is based on identifying frequency-domain transfer functions from propeller hub motion to hub loads using a time-domain simulation model of the isolated propeller. This allows the inclusion of all modeling aspects of the time-domain propeller model, such as blade elasticity and complex propeller aerodynamics, into the frequency domain whirl flutter analysis. The new method increases the fidelity of the isolated propeller representation compared to state-of-the-art methods like the one developed by Houbolt and Reed. This thesis successfully verifies the method by comparing frequency and damping to results obtained by coupled time-domain stability analysis. The work demonstrates a significant impact of elastic blade modeling on whirl flutter stability, eliminating whirl flutter in the operating range studied by considering blade elasticity.

5.2. Discussion

The Transfer-Matrix method described in this thesis enables the representation of an aeroelastic model of an isolated propeller in a frequency-domain flutter analysis of a full aircraft configuration. It aims to increase the propeller transfer

functions' modeling fidelity for whirl flutter analysis. It is verified and applied in this thesis to study the impact of blade elasticity and aerodynamic modeling on propeller whirl flutter. The following section discusses the advantages and limitations of this work in three main subsections. First, the method is compared to other available methods to highlight fundamental differences from the methodological point of view. Second, the main findings of this thesis regarding the influence of blade elasticity and aerodynamic modeling are discussed. Their potential impact is assessed in the context of existing literature. Third and last, the limitations of the method and the models chosen for the studies in this thesis are discussed, and recommendations for future work are given as means to overcome these limitations.

5.2.1. Discussion of the method

The workflow of the Transfer-Matrix method is briefly summarized below, and the fundamental differences to the other methods (the workflow for time-domain ROM by Gori et al., the Houbolt/Reed method and coupled time-domain stability analysis) are outlined.

The **TM-method** starts with an aeroelastic time-domain model of an isolated propeller. The model can include linear or non-linear blade dynamic and aerodynamic models. First, the model is trimmed to a reference operating point, and then, a polynomial pulse perturbation for the propeller hub motion (e.g., disc pitch or translation) is applied. The time response of the propeller hub loads to the perturbation is computed using time integration. Hub motion and loads are transferred into the frequency domain, and the linear transfer function is determined by division. After identifying all directions, the frequency-domain transfer matrices are transformed into modal coordinates and inserted into the frequency-domain flutter equation. This equation can be solved for the eigenvalues of the aeroelastic system afterwards using frequency-domain flutter solvers.

The TM-method is derived from the **workflow described by Gori et al.** [60]. The latter introduces identifying the hub load transfer functions from time-domain perturbations. The critical difference to the proposed TM-method is the direct use of the frequency-domain transfer matrices in the frequency-domain flutter analysis. In contrast, in the method by Gori et al., the transfer functions are approximated by a rational matrix approximation and then transformed back into the time domain. The ROM obtained by this process is used, e.g., for controller design and real-time applications for helicopters, while the primary goal of the TM-method is propeller whirl flutter analysis. The axial inflow conditions found in propeller applications are exploited for the TM-method by

introducing pulse perturbation of selected DOF. At the same time, Gori et al. rely on computationally more expensive harmonic perturbation of all hub DOF.

The TM-method provides an alternative to the classical propeller representation developed by **Houbolt and Reed** [8]. In contrast to the TM-method, which numerically identifies the propeller transfer functions, the Houbolt/Reed method derives them analytically. It provides purely aerodynamic transfer functions, including a linearized strip theory. The analytical character makes the Houbolt/Reed method fast and easy to apply but restricts its scope of modeling features. On the other hand, the TM-method mainly provides a workflow to reduce existing time-domain propeller models into frequency-domain transfer functions, so the scope of potential modeling features is only limited by available time-domain models. Many models for including blade elasticity and complex rotor aerodynamics exist today, and future developments can be included. Depending on the simulation model chosen, the TM-method requires higher computational times compared to the Houbolt/Reed method, but only for the identification of the propeller transfer matrices.

The main benefit of the TM-method is that it allows the whirl flutter analysis to remain embedded into the frequency-domain flutter analysis of the whole propeller aircraft. Contrary to this approach, methods exist for the **stability analysis of coupled time-domain aircraft models**, as described in chapter 1. These are based on modeling the entire aircraft (and not only the propeller) in the time domain and directly assessing stability there. By this, they can make full use of, e.g., non-linear descriptions of the aeroelastic system and eventual couplings between the different sub-models (e.g., aerodynamic interaction between rotor and wing, see Corle et al. [32]). However, these methods are computationally more expensive than a frequency-domain flutter analysis. Furthermore, the complete stability analysis has to be repeated when changing any model parameter (e.g., for different mass cases). In contrast, for the frequency-domain flutter analysis, only the relatively inexpensive last solution step has to be repeated and the transfer matrices can be reused.

5.2.2. Discussion of the main findings

This thesis investigates two main questions using the proposed TM-method: First, which influence does blade elasticity have on propeller whirl flutter stability predictions, and what are the underlying mechanisms? Second, which effect does aerodynamic modeling have on whirl flutter, and which features (unsteadiness, wake modeling, etc.) are required to capture the essential aspects of incompressible flow?

The main findings from the studies regarding **blade elasticity** are a mostly stabilizing effect when elasticity is considered. This stabilizing influence was reported before by other authors [55, 57] and is reproduced in this work using the TM-method for frequency-domain flutter analysis. The reason for the stabilization could be revealed by analyzing the transfer functions. The main contribution comes from a reduction in the destabilizing coupling moment between pitch and yaw ($M_{z\theta}$ and $M_{y\psi}$). Two underlying mechanisms of this reduction are identified: First, the deformation of the blades due to the harmonic loading during one revolution, which is driven by the blade stiffness and produces inertial loads, is found to counteract the aerodynamic moment term. Second, the blade responds to the harmonic loading, which induces additional angles of attack on the blade and shifts the blade loads to higher azimuth angles, reducing the aerodynamic coupling moment. The blade response is dynamically amplified and shifted in phase relative to the quasi-steady deformation if the first blade bending mode comes closer to the shaft speed. Hence, this effect is driven by the frequency placement of the first bending mode(s). The stabilizing effect has been found on the simplified pylon system and confirmed for the full aircraft configuration, eliminating whirl flutter in the studied operating range in both cases. For very flexible blades, the trend towards stabilization is reversed by the occurrence of new flutter couplings, as, e.g., common for tilt-rotor configurations [36, 56]. This serves as a lower bound for using blade elasticity directly as a mitigation measure during the design of propeller configurations, next to side effects on propeller loads and performance due to more elastic blades, which have not been studied here. On the other hand, ignoring existing blade elasticity and only considering rigid blades might make whirl flutter predictions overly conservative, as this thesis could demonstrate a stabilizing effect even for very stiff blades. Regardless of the flexibility, the TM-method enables its consideration during frequency-domain flutter analysis, allowing further studies for research and design purposes.

In contrast to the studies on the influence on blade elasticity, the studies regarding **aerodynamic modeling** revealed a clear trend for unsteady propeller aerodynamics but no clear trend concerning whirl flutter stability. Significant differences between the methods studied have been shown in predicting 1P hub loads and for the unsteady propeller transfer matrices. Quasi-steady propeller aerodynamics significantly over-predict the in-plane loads compared to the panel free wake reference by 47.5%. Considering unsteady blade aerodynamics by using Wagner's function improves the fit, especially for the out-of-phase components, but still shows considerable over-prediction. The effect of azimuthally varying induced velocities improves the predictions further to the level of the panel-free-wake reference. The requirement for an unsteady blade model and azimuthally varying induced velocities are already reported in the literature for the

predictions of 1P hub forces [25]. Furthermore, an effect of the airfoil moment on the out-of-phase 1P hub moment is found. The following studies on whirl flutter stability with the simplified pylon system reveal a spread between the different methods that is, on the one hand, not directly related to the absolute level of agreement between the unsteady aerodynamic predictions and, on the other hand, dependent on the mode shapes involved. Further investigations indicate that relative differences between force and moment terms are more critical than the absolute force level of the hub loads, as destabilizing and stabilizing terms cancel each other. For the full aircraft configuration, the flutter speeds correlate better with the absolute level of the predicted aerodynamic loads (small 1P hub loads yield a more stable system). This is attributed to additional stabilizing terms in the flutter equation in the form of wing aerodynamic forces. Hence, the sensitivity with regard to the stabilizing propeller derivatives is smaller, and the reduction in the amplitude of the destabilizing coupling moment takes precedence. Although not investigated in this thesis, the absolute value of the harmonic blade loads should play a more significant role when considering blade flexibility simultaneously, as the harmonic blade loading deforms the blades and creates the stabilizing effect of blade deformation. With smaller amplitudes, e.g., due to induced velocities considered, the stabilizing effect should be slightly reduced.

In general, the effect of blade flexibility has proven to be much larger than the sensitivity to aerodynamic parameters such as shaft power or aerodynamic modeling. For the full aircraft configuration, only a relatively small variation (up to 6%) of the flutter speed occurred between the unsteady aerodynamic methods, while blade elasticity eliminated whirl flutter. Not all aerodynamic parameters have been studied in this thesis. For example, only incompressible aerodynamics are investigated. Still, the results strongly indicate the importance of blade elasticity.

The TM-method allows for the inclusion of many effects in the flutter analysis that are neglected, e.g., in the Houbolt/Reed method. The findings about the influence of the investigated parameters described above are purely based on numerical simulations with low- to mid-fidelity methods. To exploit these new capabilities for aircraft design and certification, the propeller models used for the identification should be validated, e.g., with **validation** cases from high-fidelity numerical simulations or experiments. Measuring the dynamic hub load response of a propeller undergoing forced-motion pitch oscillations in a representative wind-tunnel experiment would, for example, yield an excellent validation basis for the TM-method and the models used with it. Extending these experiments towards a propeller-wing configuration could also cover potential aerodynamic interaction effects, which have been neglected in this thesis (compare next discussion section). After the aeroelastic transfer functions

of such systems are understood and validated, flutter stability experiments or in-flight damping measurements can provide the final validation cases for the whirl-flutter workflow.

5.2.3. Discussion of the limitations

The following section discusses the limitations of this work and potential measures to overcome them. Some limitations concern the method and the systems or operating points that can be covered. Others apply to the studies conducted with the TM-method in this thesis and the assumptions, e.g., for the aerodynamics. Both are repeated and discussed concerning their potential impact, suggesting further studies.

To derive the efficient procedure suited for propeller whirl flutter analysis in the frequency domain as outlined in section 2.2.3, some limitations have been put onto the system to be analyzed. First of all, to allow for an efficient pulse identification, **axial inflow conditions** (e.g., zero angle of attack) have been assumed for this work. This makes the system time-invariant concerning the non-rotating hub loads, allowing for pulse perturbation. Furthermore, it makes the system axially symmetric, reducing the number of directions in which the hub loads must be identified. The system becomes time-periodic for non-axial inflow conditions (e.g., a propeller under angle or attack). When subtracting the steady loads in Eq. 2.27, this must be considered. Furthermore, a single-harmonic input to a periodic system yields a multi-harmonic output, which prevents pulse-identification. For small angles of attack, the effect might be small. For larger angles, harmonic identification has to be used (as used by Gori et al. [60]), which makes the process computationally more expensive. Due to the lack of axial symmetry, all hub DOFs must be identified individually. The effect is expected to be small for propeller aircraft configurations, as the angles of attack are small, especially in the high-speed regime. This aspect is more critical for other configurations, e.g., those from urban air mobility that might also use propellers to generate lift.

The **propeller blade control system** has been neglected as a possible load path in all the studies shown. Aircraft propellers usually only feature a control system for the blade collective angle to set the power or thrust. Dynamics stemming from this control system path might influence the hub transfer functions regarding the x-axis. Still, they should have negligible influence on the in-plane loads, which are essential for whirl flutter. As shown by Gori et al. [60], additional load paths through the control system (in their case, through the swash plate of a helicopter rotor) can be considered as additional input- and output quantities, making the transfer matrices larger than six by six and requiring additional perturbations during identification.

The TM-method is based on small perturbations for the hub motion and loads and is intended for linear whirl flutter stability analysis. The response is likely not linear for hub motion with **larger amplitudes**. Nonlinearities might arise due to geometric effects (e.g., from rotations with a large angle), unsteady aerodynamics (e.g., non-linear local lift polars), or periodicity at higher inflow angles. The effect of amplitude-dependency of the transfer matrices could be studied using harmonic perturbations with varying amplitude. The impact of nonlinearities is more critical for load analysis (e.g., gust response), where the perturbations are more significant than in a linear flutter analysis.

By identifying transfer functions from a model of the isolated propeller, **aerodynamic interaction** between the propeller and the wing is neglected, too. Aerodynamic interaction influences the steady state of both the propeller and the wing aerodynamics, as well as the unsteady loads. The steady influence of the propeller slipstream on the wing affects the dynamic pressure and flow speed by increasing the axial velocity behind the propeller and the local angle of attack on the wing due to the tangential-induced velocity. For subsonic aerodynamics, the increase of dynamic pressure affects the GAFs, and corrections for this are proposed by Rodden and Rose [14]. These can be combined with the TM-method. For transonic cases, the steady state can more significantly influence the GAFs, e.g., due to changes in shock position. To cover this, a representation of the propeller in the steady flow field, e.g., using an actuator disc in a CFD computation, could give a starting point for investigations. The steady influence of the wing's induced velocity field on the propeller's steady state changes, e.g., the angle of attack on the propeller and the local blade lift. These changes in steady state are expected to have negligible influence on the propeller transfer functions but make the process more complicated (compare the discussion of non-axial inflow above). Unsteady interaction stems from motion-induced velocities induced by the oscillating propeller on the wing or vice versa. Corrections for the induced flow angles at the propeller hub due to wing motion are proposed by Rodden and Rose [14], using DLM aerodynamics. This or a similar approach could also be used with the TM-method. To verify all these corrections, a fully coupled aerodynamic time-domain model of the propeller-wing system, e.g., using mid-fidelity methods such as UPM or even CFD, can be used (as used for the tilt-rotor studies on this topic, e.g. by Corle et al. [32]). For the fully coupled model, GAFs of the coupled system can be identified using pulse or harmonic excitation of the modal DOF and compared with GAFs obtained using the isolated wing and propeller model. One problem will remain, though, with all approaches, as it is inherent in the physics of the system: The GAFs of the system are then dependent on one additional parameter describing the operating point of the propeller, be it the rotational speed, advance ratio, or steady thrust coefficient. The correction factors proposed by Rodden and Rose, for example, depend on the propeller's

disc loading. The disc loading changes for the constant power trim, requiring velocity-dependent correction factors and, therefore, GAFs. In general, whirl flutter is a high-speed phenomenon critical in windmilling conditions. The blade lift and the induced velocities in the slipstream are negligible in these conditions. In high-speed flight, the unsteady induced flow angles are also small, as the high axial speed dominates. The aerodynamic interaction is expected to have a minor influence on the whirl flutter stability, compared to, e.g., considering blade elasticity. This should be verified, though, using the time-domain approach proposed above.

The studies in this thesis all have been conducted using incompressible aerodynamics. Potential effects of **compressible flow** range from an increase in the lift curve slope, which can be covered, e.g., using Prandtl-Glauert factor corrections for the local airfoil polars, to the evolution of shocks and supersonic areas, e.g., at the blade tips. For the nominal case studied here, the tip Mach number is 0.74, already on the border of potential transonic effects. Compressible flow phenomena are most dominant on the blade tips, where the highest local speeds occur. As changes in the aerodynamics at the blade tips affect the hub moments more than the hub forces due to the longer lever arm, they could affect whirl flutter stability and, again, could be dependent on the mode shape. To study the impact of compressible flow, full, three-dimensional CFD using Euler or URANS-equations can be used. Prandtl-Glauert corrections factors or non-linear, Mach-number dependent airfoil polars can serve as a first starting point for the strip-theory approach.

In general, to increase the aerodynamic fidelity, the current state-of-the-art uses **CFD aerodynamics**, e.g., based on the Navier-Stokes equations. For rigid propeller 1P hub load computations, CFD methods reach a good level of agreement with wind-tunnel tests [27], although aspects like the spinner aerodynamics have to be correctly accounted for (compare Ortun et al. [27]). In this thesis, the prediction of 1P hub loads is revealed to be representative of the unsteady predictions of propeller transfer matrices. Full three-dimensional CFD should, therefore, be able to predict the propeller transfer matrices of a real system, although, to the author's knowledge, no validation data exists yet. A high spatial and temporal discretization is required to model a rotating propeller, leading to high computational costs. Reduced modeling approaches such as actuator disc formulations or actuator line models [100] promise a reduction in computational time but must be adequately verified and validated for unsteady applications with elastic blade and hub motion.

The investigations in this thesis have all been conducted using the same **propeller geometry**, a five-bladed wooden composite propeller with straight blades. As the aerodynamic moment due to the airfoil moment and the offset between the quarter-chord point and the blade axes has been shown in this

thesis to influence whirl flutter, blade sweep is expected to have a potential effect on whirl flutter due to the increased offset of the aerodynamic forces. This is especially interesting for high-speed propellers with swept tips. Further parameter studies can be conducted on the structural blade parameters, too. Only general mass and stiffness scaling were applied in this work. Still, more insights into the sensitivities regarding the individual structural parameters, such as bending and torsion stiffness for different blade layouts, could provide interesting insights. For example, a structured uncertainty quantification approach can be applied to find the driving fundamental parameters in the structural and aerodynamic model to focus future investigations on those dominating effects.

In its presented form, the TM-method is tailored towards application on large propeller aircraft, with propellers operating in high-speed axial inflow conditions. The application to other aircraft configurations is possible but comes with some challenges depending on the specific configuration. One alternative to classical propeller engines are **open-rotor** or even counter-rotating open-rotor engines. While the first features a rotating propeller with a stator behind it to retrieve the energy lost in the tangential velocity, the latter features two counter-rotating rotors. Literature on a potential whirl flutter of such configurations is scarce or non-existent. While the key concept of the TM-method should also apply to such configurations, some challenges might lie in the design of such engines and the different load paths between the rotor and stator. It might be necessary to include more hub-DOF (e.g., hub of rotating part and hub of stator parts) in the transfer matrices. As mentioned in the introduction, one aircraft category suffering from whirl flutter are **tilt-rotor aircraft** with their large, flexible rotors. Especially for high-speed forward flight, the TM-method can be applied for the aeroelastic stability analysis. Additional hub-DOF for the rotor control system might have to be included. One challenge of the current form of the TM-method relevant for these rotor systems is the limited amount of information about the participation of blade modes in the flutter mode shapes. This is not so relevant for propeller configurations, where the blade modes are not directly involved in the instability mechanism, but more critical for tilt-rotor whirl flutter, which usually includes significant participation of the blade modes. A third aircraft category that might benefit from the TM-method for aeroelastic stability analysis is the new class of **urban-air-mobility** (UAM) vehicles. These often feature several propellers in exposed locations on the airframe, which are used for lift and thrust generation. To efficiently use the TM-method, further investigation is needed to determine if it can be applied efficiently for propellers at higher angles of attack. If the propellers to be investigated only have two blades, the inherent periodicity prevents the application of the TM-method, and time-domain analysis, such as Floquet analysis, is better suited.

While this thesis revolves around creating a better representation of the propeller transfer functions for whirl flutter analysis, other parameters than the propeller influence the whirl flutter predictions significantly and must be better understood, too. On the side of the structural model, the characteristics of the **shock mounts** strongly impact the engine modes and, therefore, on whirl flutter stability. As these parts are often manufactured from elastomer materials, which change their characteristics under preload, with temperature, and due to aging [101], their influence on whirl flutter stability could be another focus of attention to strive for a more complete understanding of the intricacies of propeller whirl flutter prediction.

Bibliography

[1] C. M. Harris and A. G. Piersol, eds. *Harris' shock and vibration handbook*. 5th ed. McGraw-Hill handbooks. New York: McGraw-Hill, 2002. ISBN: 978-0-07-137081-3.

[2] G. Hrycko. "Design Of The Low Vibration Turboprop Powerplant Suspension System for The DASH 7 Aircraft". In: *SAE Transactions* 92 (1983), pp. 133–145.

[3] *Certification Specifications and Acceptable Means of Compliance for Large Aeroplanes*. Tech. rep. CS-25 Amd. 23. European Aviation Safety Agency, July 2019.

[4] W. H. Reed. "Propeller-rotor whirl flutter: A state-of-the-art review". In: *Journal of Sound and Vibration* 4.3 (Nov. 1966), pp. 526–544. DOI: 10.1016/0022-460X(66)90142-8.

[5] J. Cecrdle. *Whirl Flutter of Turboprop Aircraft Structures*. ISBN 978-1-78242-185-6. Elsevier, 2015. DOI: 10.1016/C2014-0-01800-X.

[6] E. S. Taylor and K. A. Browne. "Vibration Isolation of Aircraft Power Plants". In: *Journal of the Aeronautical Sciences* 6.2 (Dec. 1938), pp. 43–49. DOI: 10.2514/8.760.

[7] R. E. Donham and G. A. Watts. "The First Case of Whirl Flutter". In: *The revolution in structural dynamics: the big "shake-up" in airframe design*. Ed. by H. I. Flomenhoft. Palm Beach Gardens, FL: Dynaflo Press, 1997. ISBN: 978-0-9659773-0-2.

[8] J. C. Houbolt and W. H. Reed III. "Propeller-nacelle whirl flutter". In: *Journal of the Aerospace Sciences* 29.3 (1962), pp. 333–346. DOI: 10.2514/8.9417.

[9] H. S. Ribner. *Propellers in Yaw*. NACA Wartime Report 3L09. Langley Field, Hampton, Va., Dec. 1943.

[10] S. R. Bland and R. M. Bennett. *Wind-tunnel measurements of propeller whirl-flutter speeds and static-stability derivatives and comparison with theory*. NASA Technical Note NASA TN D-1807. Langley Station, Hampton, Va., Aug. 1963.

[11] R. M. Bennett and S. R. Bland. *Experimental and Analytical Investigation of Propeller Whirl Flutter of a Power Plant on a Flexible Wing*. NASA Technical Note NASA TN D-2399. Langley Station, Hampton, Va., Aug. 1964.

[12] F. Nitzsche. “Whirl-flutter investigation on an advanced turboprop configuration”. In: *Journal of Aircraft* 26.10 (1989), pp. 939–946. DOI: 10.2514/3.45865.

[13] F. Nitzsche. “Insights on the whirl-flutter phenomena of advanced turboprops and propfans”. In: *Journal of Aircraft* 28.7 (July 1991), pp. 463–470. DOI: 10.2514/3.46050.

[14] W. Rodden and T. Rose. “Propeller/nacelle whirl flutter addition to MSC/Nastran”. In: *Proceedings of the 1989 MSC World User’s Conference*. Anaheim, CA, USA, 1989.

[15] J. Cecrdle. “Exploitation of optimization solution for determination of whirl flutter stability boundaries”. In: *ICAS Secretariat - 26th Congress of International Council of the Aeronautical Sciences 2008, ICAS 2008*. Vol. 5. Optimage Ltd. on behalf of the International Council of the Aeronautical Sciences (ICAS), 2008, pp. 743–752.

[16] J. Cecrdle. “Analysis of Twin Turboprop Aircraft Whirl-Flutter Stability Boundaries”. In: *Journal of Aircraft* 49.6 (Nov. 2012), pp. 1718–1725. DOI: 10.2514/1.C031390.

[17] J Cecrdle. “Influence of propeller blade lift distribution on whirl flutter stability characteristics”. In: *Intern. J. of Mech., Aerosp., Manufact., Indust. Scien. and Engin* 8.4 (2014).

[18] J. Cecrdle. “Whirl flutter-related certification according to FAR/CS 23 and 25 regulation standards”. In: *Proceedings of International Forum on Aeroelasticity and Structural Dynamics (IFASD)*. Savannah, GA (USA), June 2019.

[19] C. Koch. “Parametric whirl flutter study using different modelling approaches”. In: *CEAS Aeronautical Journal* 13 (Oct. 2021), pp. 57–67. DOI: 10.1007/s13272-021-00548-0.

[20] N. Böhnisch, C. Braun, S. Koschel, and P. Marzocca. “Whirl Flutter for Distributed Propulsion Systems on a Flexible Wing”. In: *AIAA SCITECH 2022 Forum*. San Diego, CA & Virtual: American Institute of Aeronautics and Astronautics, Jan. 2022. DOI: 10.2514/6.2022-1755.

[21] N. Böhnisch, C. Braun, V. Muscarello, and P. Marzocca. “A Sensitivity Study on Aeroelastic Instabilities of Slender Wings with a Large Propeller”. In: *AIAA SCITECH 2023 Forum*. National Harbor, MD & Online: American Institute of Aeronautics and Astronautics, Jan. 2023. DOI: 10.2514/6.2023-1893.

[22] C. Mair, D. Rezgui, and B. Titurus. “Nonlinear stability analysis of whirl flutter in a rotor-nacelle system”. In: *Nonlinear Dynamics* 94.3 (Nov. 2018), pp. 2013–2032. DOI: 10.1007/s11071-018-4472-y.

[23] A. Quintana, B. E. Saunders, R. Vasconcellos, and A. Abdelkefi. "The influence of freeplay on the whirl flutter and nonlinear characteristics of rotor-nacelle systems". In: *Meccanica* 58.4 (Apr. 2023), pp. 659–686. DOI: 10.1007/s11012-023-01658-1.

[24] S. V. Gali, T. G. Goehmann, and C. Riso. "Fundamental investigation into output-based prediction of whirl flutter bifurcations". In: *Journal of Fluids and Structures* 123 (Nov. 2023). DOI: 10.1016/j.jfluidstructs.2023.103986.

[25] H. R. Smith. "Engineering models of aircraft propellers at incidence". PhD thesis. Glasgow, UK: University of Glasgow, Jan. 2015. URL: https://theses.gla.ac.uk/6799/.

[26] X. Fei, B. L. Litherland, and B. J. German. "Development of an Unsteady Vortex Lattice Method to Model Propellers at Incidence". In: *AIAA Journal* (Sept. 2021). DOI: 10.2514/1.J060133.

[27] B. Ortun, R. Boisard, and I. G. Martino. "Assessment of propeller 1P loads predictions". In: *International Journal of Engineering Systems Modelling and Simulation* 4.1/2 (2012). DOI: 10.1504/IJESMS.2012.044842.

[28] J.-M. Bousquet and P. Gardarein. "Improvements on computations of high speed propeller unsteady aerodynamics". In: *Aerospace Science and Technology* 7.6 (Sept. 2003), pp. 465–472. DOI: 10.1016/S1270-9638(03)00046-4.

[29] L. P. Ruiz-Calavera and D. Perdones-Diaz. "CFD computation of in-plane propeller shaft loads". In: *49th AIAA/ASME/SAE/ASEE Joint Propulsion Conference*. San Jose, CA: American Institute of Aeronautics and Astronautics, July 2013. DOI: 10.2514/6.2013-3798.

[30] M. Gennaretti and L. Greco. "Whirl flutter analysis of prop-rotors using unsteady aerodynamics reduced-order models". In: *The Aeronautical Journal* 112.1131 (May 2008), pp. 261–270. DOI: 10.1017/S0001924000002207.

[31] Z. Wang and P. Chen. "Whirl flutter analysis with propeller aerodynamic derivatives computed by unsteady vortex lattice method". In: *56th AIAA/ASCE/AHS/ASC Structures, Structural Dynamics, and Materials Conference*. Kissimmee, Florida: American Institute of Aeronautics and Astronautics, 2015. DOI: 10.2514/6.2015-1419.

[32] E. Corle, M. Floros, and S. Schmitz. "On the Influence of Inflow Model Selection for Time-Domain Tiltrotor Aeroelastic Analysis". In: *Journal of the American Helicopter Society* 66.3 (July 2021), pp. 1–12. DOI: 10.4050/JAHS.66.032009.

[33] S. Gul and H. Yeo. “Whirl flutter predictions for distributed tiltrotor configurations”. In: *ERF 2023 - 49th European Rotorcraft Forum*. Bückeburg, Germany, Sept. 2023.

[34] W. Johnson. *Dynamics of tilting proprotor aircraft in cruise flight*. NASA Technical Note NASA TN D-7677. NASA, May 1974.

[35] M. I. Young and R. T. Lytwyn. “The Influence of Blade Flapping Restraint on the Dynamic Stability of Low Disk Loading Propeller-Rotors”. In: *Journal of the American Helicopter Society* 12.4 (1967), pp. 38–54. DOI: 10.4050/JAHS.12.38.

[36] D. R. A. Johnston. “Parametric Studies of instabilities associated with large, flexible rotor propellers”. In: *28th Annual National Forum of the American Helicopter Society*. Washington, D.C.: American Helicopter Society, May 1972.

[37] D. L. Kunz. “Analysis of Proprotor Whirl Flutter: Review and Update”. In: *Journal of Aircraft* 42.1 (Jan. 2005), pp. 172–178. DOI: 10.2514/1.4953.

[38] W. Johnson and A. Datta. “Requirements for Next Generation Comprehensive Analysis of Rotorcraft”. In: *AHS Specialist’s Conference on Aeromechanics*. San Francisco, CA, US: American Helicopter Society, Jan. 2008.

[39] H. Yeo, J. Bosworth, C. W. Acree Jr., and A. R. Kreshock. “Comparison of CAMRAD II and RCAS Predictions of Tiltrotor Aeroelastic Stability”. In: *Journal of the American Helicopter Society* 63.2 (Apr. 2018), pp. 1–13. DOI: 10.4050/JAHS.63.022001.

[40] D. J. Piatak, R. G. Kvaternik, M. W. Nixon, C. W. Langston, J. D. Singleton, R. L. Bennett, and R. K. Brown. “A Parametric Investigation of Whirl-Flutter Stability on the WRATS Tiltrotor Model”. In: *Journal of the American Helicopter Society* 47.2 (Apr. 2002), pp. 134–144. DOI: 10.4050/JAHS.47.134.

[41] A. R. Kreshock, R. P. Thornburgh, and H. Yeo. “Comparison of Comprehensive Analyses Predicting Whirl Flutter Stability of the Wing and Rotor Aeroelastic Test System”. In: *Journal of the American Helicopter Society* 64.4 (Oct. 2019), pp. 1–12. DOI: 10.4050/JAHS.64.042010.

[42] J. Shen and H. Kang. “Comparison Study of Tiltrotor Whirl Flutter Using Two Rotorcraft Comprehensive Analyses”. In: *Journal of Aircraft* 54.2 (Mar. 2017), pp. 845–850. DOI: 10.2514/1.C033905.

[43] J. Shen, P. Masarati, B. Roget, D. Piatak, J. Singleton, and M. Nixon. “Modeling a stiff-inplane tiltrotor using two multibody analyses: A validation study”. In: *Annual Forum Proceedings - AHS International*. Vol. 3. American Helicopter Society, 2008, pp. 2307–2315.

[44] A. Cocco, S. Mazzetti, P. Masarati, S. v. Hoff, and B. Timmerman. "Numerical Whirl–Flutter analysis of a tiltrotor semi-span wind tunnel model". In: *CEAS Aeronautical Journal* 13 (Sept. 2022), 923—938. DOI: 10.1007/s13272-022-00605-2.

[45] S. van 't Hoff, J. van Vilsteren, A. Cocco, and P. Masarati. "Design of a Tiltrotor Semi-Span Wind Tunnel Model for Whirl Flutter Investigations". In: *AIAA SCITECH 2023 Forum*. National Harbor, MD & Online: American Institute of Aeronautics and Astronautics, Jan. 2023. DOI: 10.2514/6.2023-1306.

[46] A. R. Kreshock, R. Thornburgh, and M. Wilbur. "Overview of the TiltRotor Aeroelastic Stability Testbed". In: *AIAA SCITECH 2022 Forum*. San Diego, CA & Virtual: American Institute of Aeronautics and Astronautics, Jan. 2022. DOI: 10.2514/6.2022-0566.

[47] F. Tsai, J. R. Sutherland, A. Akinwale, A. Morin, S. Gul, and A. Datta. "Whirl Flutter Test of the Maryland Tiltrotor Rig: Overview". In: *AIAA SCITECH 2022 Forum*. San Diego, CA & Virtual: American Institute of Aeronautics and Astronautics, Jan. 2022. DOI: 10.2514/6.2022-0567.

[48] A. Cocco. "Comprehensive mid-fidelity simulation environment for aeroelastic stability analysis of tiltrotors with pilot-in-the-loop". PhD Thesis. Politecnio di Milano, 2022. URL: https://www.politesi.polimi.it/handle/10589/195753.

[49] V. Muscarello and G. Quaranta. "Exploration of the Effects of Rotor Blade Twist on Whirl-Flutter Stability Boundaries". In: *Journal of Aircraft* (Sept. 2023), pp. 1–16. DOI: 10.2514/1.C037479.

[50] R. Whittle. *The dream machine: the untold history of the notorious V-22 Osprey*. New York: Simon & Schuster, 2010. ISBN: 978-1-4165-6295-5.

[51] E. Corle, M. Floros, and S. Schmitz. "Transient CFD/CSD Tiltrotor Stability Analysis". In: *AIAA Scitech 2019 Forum*. San Diego, California: American Institute of Aeronautics and Astronautics, Jan. 2019. DOI: 10.2514/6.2019-2132.

[52] C. Acree Jr, K. Hoffman, and B. P. Works. "Whirl Flutter Studies for a SSTOL Transport Demonstrator". In: *American Helicopter Society 4 th Decennial Specialist's Conference on Aeromechanics*. San Francisco, CA: American Helicopter Society, 2004.

[53] C. B. Hoover, J. Shen, and A. R. Kreshock. "Propeller Whirl Flutter Stability and Its Influence on X-57 Aircraft Design". In: *Journal of Aircraft* 55.5 (Sept. 2018), pp. 2169–2175. DOI: 10.2514/1.C034950.

[54] C. B. Hoover and J. Shen. "Whirl Flutter Analysis of a Free-Flying Electric-Driven Propeller Aircraft". In: *Journal of Aircraft* 56.2 (Mar. 2019), pp. 831–836. DOI: 10.2514/1.C035263.

[55] C. B. Hoover and J. Shen. “Fundamental understanding of propeller whirl flutter through multibody dynamics”. In: *AIAA Scitech 2019 Forum*. San Diego, California: American Institute of Aeronautics and Astronautics, Jan. 2019. DOI: 10.2514/6.2019-1864.

[56] H. Yeo and A. R. Kreshock. “Whirl Flutter Investigation of Hingeless Proprotors”. In: *Journal of Aircraft* (Mar. 2020), pp. 1–11. DOI: 10.2514/1.C035609.

[57] R. E. Donham. “Effect of propeller blade bending dynamics on 1P loads and whirl flutter”. In: *Proceedings of International Forum on Aeroelasticity and Structural Dynamics (IFASD)*. Vol. 28. München, Germany: Deutsche Gesellschaft fuer Luft und Raumfahrt (DGLR), June 2005.

[58] R. L. Bielawa. “An improved technique for testing helicopter rotor-pylon aeromechanical stability using measured rotor dynamic impedance characteristics”. In: *European Rotorcraft Forum*. Paper-Nr. 97. The Hague, Netherlands: The Netherlands Association of Aeronautical Engineers, Aug. 1984.

[59] R. L. Bielawa. *Rotary wing structural dynamics and aeroelasticity*. AIAA education series. Washington, DC: American Institute of Aeronautics and Astronautics, 1992. ISBN: 978-1-56347-031-8.

[60] R. Gori, J. Serafini, M. Molica Colella, and M. Gennaretti. “Assessment of a state-space aeroelastic rotor model for rotorcraft flight dynamics”. In: *CEAS Aeronautical Journal* 7.3 (Sept. 2016), pp. 405–418. DOI: 10.1007/s13272-016-0196-1.

[61] M. Gennaretti and D. Muro. “Multiblade Reduced-Order Aerodynamics for State-Space Aeroelastic Modeling of Rotors”. In: *Journal of Aircraft* 49.2 (Mar. 2012), pp. 495–502. DOI: 10.2514/1.C031422.

[62] J. Schwochow. *Die aeroelastische Stabilitätsanalyse - ein praxisnaher Ansatz zur intervalltheoretischen Betrachtung von Modellierungsunsicherheiten am Flugzeug*. DLR Forschungsbericht DLR-FB-2012-21. Göttingen: DLR Institut für Aeroelastik, 2013. URL: https://elib.dlr.de/81176/.

[63] H. J. Cunningham and R. N. Desmarais. *Generalization of the Subsonic Kernel Function in the s-Plan with Applications to Flutter Analysis*. NASA Technical Paper NASA TP 2292. Langley Station, Hampton, Va.: NASA, Mar. 1984.

[64] H. J. Hassig. “An approximate true damping solution of the flutter equation by determinant iteration.” In: *Journal of Aircraft* 8.11 (Nov. 1971), pp. 885–889. DOI: 10.2514/3.44311.

[65] E. Albano and W. P. Rodden. "A doublet-lattice method for calculating lift distributions on oscillating surfaces in subsonic flows." In: *AIAA Journal* 7.2 (Feb. 1969), pp. 279–285. DOI: 10.2514/3.5086.

[66] L. H. van Zyl. "Use of eigenvectors in the solution of the flutter equation". In: *Journal of Aircraft* 30.4 (July 1993), pp. 553–554. DOI: 10.2514/3.46380.

[67] P. C. Chen. "Damping Perturbation Method for Flutter Solution: The g-Method". In: *AIAA Journal* 38.9 (Sept. 2000), pp. 1519–1524. DOI: 10.2514/2.1171.

[68] B. Gustavsen and A. Semlyen. "Rational approximation of frequency domain responses by vector fitting". In: *IEEE Transactions on Power Delivery* 14.3 (July 1999), pp. 1052–1061. DOI: 10.1109/61.772353.

[69] B. Gustavsen. "Improving the Pole Relocating Properties of Vector Fitting". In: *IEEE Transactions on Power Delivery* 21.3 (July 2006), pp. 1587–1592. DOI: 10.1109/TPWRD.2005.860281.

[70] D. Deschrijver, M. Mrozowski, T. Dhaene, and D. De Zutter. "Macromodeling of Multiport Systems Using a Fast Implementation of the Vector Fitting Method". In: *IEEE Microwave and Wireless Components Letters* 18.6 (June 2008), pp. 383–385. DOI: 10.1109/LMWC.2008.922585.

[71] C. Koch. "Whirl flutter stability assessment using rotor transfer matrices". In: *Proceedings of the International Forum on Aeroelasticity and Structural Dynamics (IFASD) 2022*. Madrid, Spain, June 2022.

[72] S. Waitz and H. Hennings. "The aeroelastic impact of engine thrust and gyroscopics on aircraft flutter instabilities". In: *Proceedings of International Forum on Aeroelasticity and Structural Dynamics (IFASD)*. IFASD-2015-192. Saint Petersburg, June 2015.

[73] C. Koch and B. Koert. "Influence of blade elasticity on propeller whirl flutter stability". In: *AIAA SCITECH 2023 Forum*. National Harbor, MD & Online: American Institute of Aeronautics and Astronautics, Jan. 2023. DOI: 10.2514/6.2023-1307.

[74] C. Koch and B. Koert. "Including Blade Elasticity into Frequency-Domain Propeller Whirl Flutter Analysis". In: *Journal of Aircraft* (Oct. 2023). DOI: 10.2514/1.C037501.

[75] C. Koch, N. Böhnisch, H. Verdonck, O. Hach, and C. Braun. "Comparison of Unsteady Low- and Mid-Fidelity Propeller Aerodynamic Methods for Whirl Flutter Applications". In: *Applied Sciences* 14.2 (Jan. 2024). DOI: 10.3390/app14020850.

[76] J. Noël, C. Koch, B. Stickan, H. Bleecke, and J. Arnold. "Influence of blade elasticity on the whirl flutter stability of a propeller-driven aircraft". In: *Proceedings of the International Forum on Aeroelasticity and Structural Dynamics (IFASD) 2024*. unpublished. Den Haag, NL, June 2024.

[77] C. Koch. "Whirl flutter analysis using linearized propeller transfer matrices". In: *Proceedings of the International Forum on Aeroelasticity and Structural Dynamics (IFASD) 2024*. unpublished. Den Haag, NL, June 2024.

[78] Y. C. Fung. *An introduction to the theory of aeroelasticity*. Dover ed. Mineola, N. Y: Dover Publications, 2008. ISBN: 978-0-486-46936-2.

[79] J. Arnold and S. Waitz. "Using Multibody Dynamics for the Stability Assessment of a New Double-Swept Rotor Blade Setup". In: *ERF 2018 - 44th European Rotorcraft Forum*. Delft, The Netherlands: The Netherlands Association of Aeronautical Engineers, Sept. 2018.

[80] W. Johnson. *Helicopter theory*. New York: Dover Publications, 1994. ISBN: 978-0-486-68230-3.

[81] T. Burton, N. Jenkins, D. Sharpe, and E. Bossanyi. *Wind energy handbook*. Second Edition. Chichester , West Sussex: Wiley, 2011. ISBN: 978-0-470-69975-1.

[82] P. Kunze. "Evaluation of an unsteady panel method for the prediction of rotor-rotor and rotor-bodyinteractions in preliminary design". In: *41st European Rotorcraft Forum 2015, ERF 2015*. Vol. 1. Deutsche Gesellschaft fuer Luft und Raumfahrt (DGLR), 2015, pp. 473–485.

[83] J. Yin and S. Ahmed. "Helicopter main-rotor/tail-rotor interaction". In: *Journal of the American Helicopter Society* 45.4 (2000), pp. 293–302. DOI: 10.4050/jahs.45.293.

[84] J. Yin, B. Van Der Wall, and G. Wilke. "Rotor aerodynamic and noise under influence of elastic blade motion and different fuselage modeling". In: *40th European Rotorcraft Forum 2014*. Vol. 1. Royal Aeronautical Society, 2014, pp. 475–495.

[85] Dassault Systemes. *Simpack*. Version 2019x.2. 2019. URL: https://www.3ds.com/de/produkte-und-services/simulia/produkte/simpack/.

[86] O. Wallrapp. "Linearized Flexible Multibody Dynamics Including Geometric Stiffening Effects". In: *Mechanics of Structures and Machines* 19.3 (Jan. 1991), pp. 385–409. DOI: 10.1080/08905459108905149.

[87] O. Wallrapp. "Standardization of Flexible Body Modeling in Multibody System Codes, Part I: Definition of Standard Input Data". In: *Mechanics of Structures and Machines* 22.3 (Jan. 1994), pp. 283–304. DOI: 10.1080/08905459408905214.

[88] O. Wallrapp. "Flexible Bodies in Multibody System Codes". In: *Vehicle System Dynamics* 30.3-4 (Sept. 1998), pp. 237–256. DOI: 10.1080/00423119808969450.

[89] K. E. Brenan, S. L. Campbell, and L. R. Petzold. *Numerical solution of initial value problems in differential algebraic equations*. New York, NY: North Holland, 1989. ISBN: 978-0-444-01511-2.

[90] D. A. Peters and K. H. Hohenemser. "Application of the Floquet transition matrix to problems of lifting rotor stability". In: *Journal of the American Helicopter Society* 16.2 (1971), pp. 25–33. DOI: https://doi.org/10.4050/JAHS.16.25.

[91] P. Fisker Skjoldan. *Aeroelastic modal dynamics of wind turbines including anisotropic effects*. Roskilde: Risø National Laboratory, 2011. ISBN: 978-87-550-3848-6. URL: https://backend.orbit.dtu.dk/ws/files/5509069/ris-phd-66.pdf.

[92] D. Peters and S. Lieb. "Significance of floquet eigenvalues and eigenvectors for the dynamics of time-varying systems". In: *Annual Forum Proceedings - AHS International*. Vol. 3. American Helicopter Society, 2009, pp. 2529–2558.

[93] R. Mohan and G. H. Gaonkar. "A Unified Assessment of Fast Floquet, Generalized Floquet, and Periodic Eigenvector Methods for Rotorcraft Stability Predictions". In: *Journal of the American Helicopter Society* 58.4 (Oct. 2013), pp. 1–12. DOI: 10.4050/JAHS.58.042002.

[94] K. H. Hohenemser and S.-K. Yin. "Some applications of the method of multiblade coordinates". In: *Journal of the American Helicopter Society* 17.3 (1972), pp. 3–12.

[95] D. A. Peters and A. Su. "Effect of hidden dynamic states on floquet eigenvalues". In: *Journal of the American Helicopter Society* 35.4 (1990), pp. 72–75.

[96] R. E. Donham and D. J. Osterholt. "Utilizing test results to show adding flexibility of propeller blades is more representative than the classical rigid blade propeller whirl flutter analysis". In: *Proceedings of International Forum on Aeroelasticity and Structural Dynamics (IFASD)*. Stockholm, Sweden, 2007.

[97] F. Hitchens. *Propeller Aerodynamics: The History, Aerodynamics & Operation of Aircraft Propellers*. Andrews UK Ltd, 2015. ISBN: 978-1-78538-125-6.

[98] ZONA Technology. *ZAERO*. Version 9.3. 2019. URL: https://www.zonatech.com/zaero.html.

[99] Hexagon. *MSC Nastran*. Version 2023.1. 2023. URL: https://hexagon.com/products/product-groups/computer-aided-engineering-software/msc-nastran.

[100] N. Troldborg, F. Zahle, P. Réthoré, and N. N. Sørensen. "Comparison of wind turbine wake properties in non-sheared inflow predicted by different computational fluid dynamics rotor models". In: *Wind Energy* 18.7 (July 2015), pp. 1239–1250. DOI: 10.1002/we.1757.

[101] M. Gröhlich, A. Lang, M. Böswald, and J. Meier. "Viscoelastic damping design – Thermal impact on a constrained layer damping treatment". In: *Materials & Design* 207 (Sept. 2021). DOI: 10.1016/j.matdes.2021.109885.

[102] C. Koch. "Aeroelastische Untersuchung eines V-Leitwerks mit integrierten Antriebseinheiten". MA thesis. Aachen: RWTH Aachen University, Apr. 2019.

[103] C. Koch, J. Arnold, and H. Schmidt. "Aeroelastische Untersuchung eines V-Leitwerks mit integrierten Antriebseinheiten". In: *Deutscher Luft- und Raumfahrtkongress 2019*. Darmstadt: Deutsche Gesellschaft fuer Luft und Raumfahrt (DGLR), Nov. 2019. DOI: 10.25967/490238.

[104] C. Koch and J. Arnold. "Aeroelastic stability assessment of a V-Tail with integrated propulsion units". In: *Proceedings of the Second International Symposium on Flutter and its Applications*. Paris, May 2020.

[105] T. Moxter, W. Enders, B. Kelm, M. Scholjegerdes, C. Koch, and P. Dahmann. "Untersuchung alternativer Antriebe von Kleinflugzeugen anhand des hybrid-elektrischen Motorseglers FVA 30". In: *Deutscher Luft- und Raumfahrtkongress 2020*. Aachen (virtuell): Deutsche Gesellschaft fuer Luft und Raumfahrt (DGLR), 2020.

[106] C. Koch. "Relevance of whirl flutter for electric aircraft configurations". In: *Deutscher Luft- und Raumfahrtkongress 2020*. Aachen (virtuell): Deutsche Gesellschaft fuer Luft und Raumfahrt (DGLR), Sept. 2020.

[107] A. Voß, C. Koch, S. Niemann, M. Mantei, V. Handojo, and C. Weiser. "Transition From Preliminary to Detailed Design of a Highly Elastic Solar Electric Aircraft". In: *Proceedings of the International Forum on Aeroelasticity and Structural Dynamics (IFASD) 2022*. Madrid, Spain, June 2022.

A

Appendix

A.1. Definition of propeller derivatives

This section includes the full list of definitions for the sixteen aerodynamic propeller derivatives derived by Houbolt and Reed [8, 14]. For the definition of the correction factors and variables, refer to section 2.2.2.

$$C_{y\theta} = -\left(\frac{N_b}{2}\right)\left(\frac{1}{\pi R}\right)\int_{\eta_{hub}}^{1} \frac{\mu}{\sqrt{\mu^2+\eta^2}}\, C_{Ar}\; c(\eta)\; C_{l\alpha}(\eta)\; \mathrm{Im}(\gamma(k))d\eta \quad \text{(A.1)}$$

$$C_{z\theta} = -\left(\frac{N_b}{2}\right)\left(\frac{1}{\pi R}\right)\int_{\eta_{hub}}^{1} \frac{\mu}{\sqrt{\mu^2+\eta^2}}\, C_{Ar}\; c(\eta)\; C_{l\alpha}(\eta)\; \mathrm{Re}(\gamma(k))d\eta \quad \text{(A.2)}$$

$$C_{m\theta} = -\left(\frac{N_b}{4}\right)\left(\frac{1}{\pi R}\right)\int_{\eta_{hub}}^{1} \frac{\eta^2}{\sqrt{\mu^2+\eta^2}}\, C_{Ar}\; c(\eta)\; C_{l\alpha}(\eta)\; \mathrm{Im}(\gamma(k))d\eta \quad \text{(A.3)}$$

$$C_{n\theta} = -\left(\frac{N_b}{4}\right)\left(\frac{1}{\pi R}\right)\int_{\eta_{hub}}^{1} \frac{\eta^2}{\sqrt{\mu^2+\eta^2}}\, C_{Ar}\; c(\eta)\; C_{l\alpha}(\eta)\; \mathrm{Re}(\gamma(k))d\eta \quad \text{(A.4)}$$

$$C_{yq} = -\left(\frac{N_b}{2}\right)\left(\frac{1}{\pi R}\right)\int_{\eta_{hub}}^{1} \frac{\eta^2}{\sqrt{\mu^2+\eta^2}}\, C_{Ar}\; c(\eta)\; C_{l\alpha}(\eta)\; \mathrm{Im}(\gamma(k))d\eta \quad \text{(A.5)}$$

$$C_{zq} = \left(\frac{N_b}{2}\right)\left(\frac{1}{\pi R}\right)\int_{\eta_{hub}}^{1} \frac{\eta^2}{\sqrt{\mu^2+\eta^2}}\, C_{Ar}\; c(\eta)\; C_{l\alpha}(\eta)\; \mathrm{Re}(\gamma(k))d\eta \quad \text{(A.6)}$$

$$C_{mq} = -\left(\frac{N_b}{4}\right)\left(\frac{1}{\pi R}\right)\int_{\eta_{hub}}^{1} \frac{\eta^4}{\mu\sqrt{\mu^2+\eta^2}}\, C_{Ar}\; c(\eta)\; C_{l\alpha}(\eta)\; \mathrm{Im}(\gamma(k))d\eta \quad \text{(A.7)}$$

$$C_{nq} = \left(\frac{N_b}{4}\right)\left(\frac{1}{\pi R}\right)\int_{\eta_{hub}}^{1} \frac{\eta^4}{\mu\sqrt{\mu^2+\eta^2}}\, C_{Ar}\; c(\eta)\; C_{l\alpha}(\eta)\; \mathrm{Re}(\gamma(k))d\eta \quad \text{(A.8)}$$

$$\begin{aligned} C_{z\psi} = C_{y\theta}\ ;\ C_{y\psi} = -C_{z\theta} \\ C_{m\psi} = -C_{n\theta}\ ;\ C_{n\psi} = C_{m\theta} \\ C_{zr} = C_{yq}\ ;\ C_{yr} = -C_{zq} \\ C_{mr} = -C_{nq}\ ;\ C_{nr} = -C_{mq} \end{aligned} \quad \text{(A.9)}$$

A.2. Higher modes of the generic aircraft model

The following three figures include the higher modes 15 to 26 of the generic aircraft, in addition to the modes shown in Fig. 3.8 and 3.9. Modes higher than number 26 are not shown.

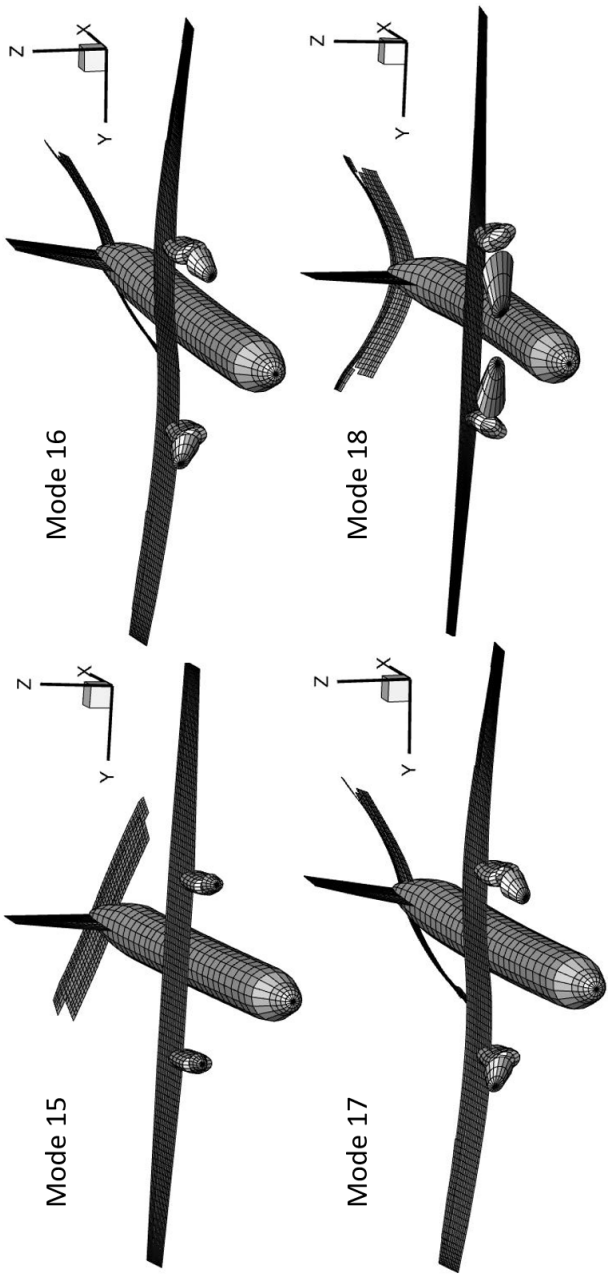

Figure A.1.: The elastic modes 15 - 18 of the full aircraft, visualized on the aerodynamic panel grid

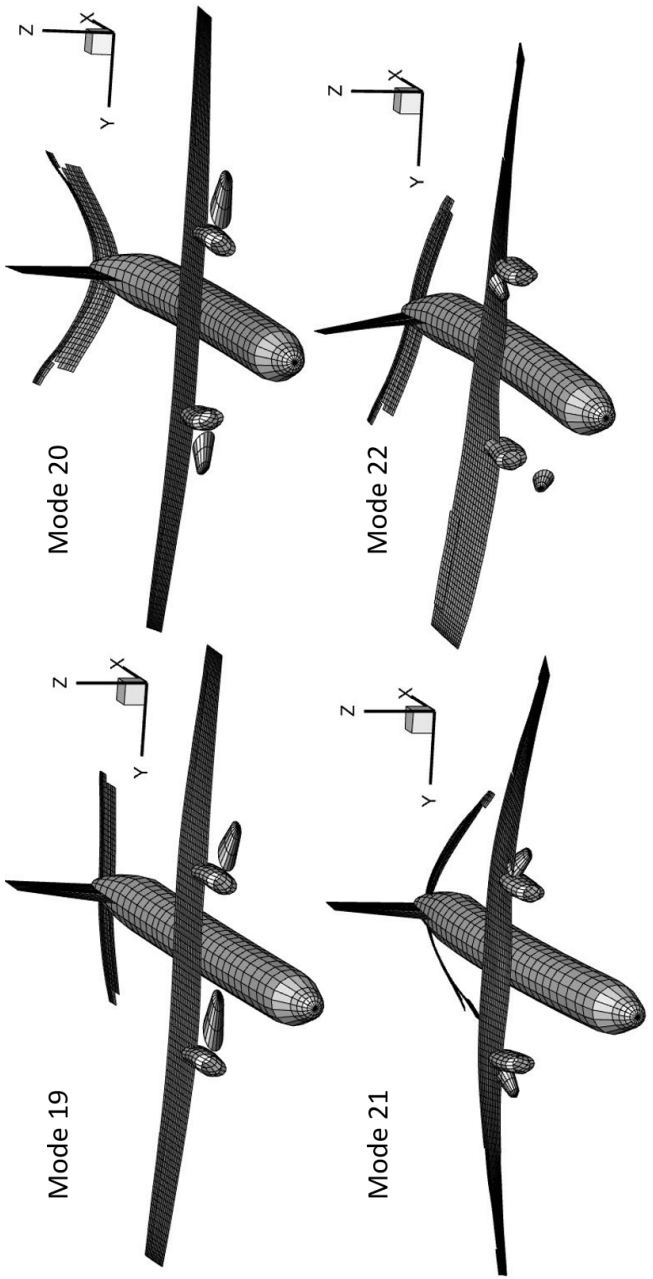

Figure A.2.: The elastic modes 19 - 22 of the full aircraft, visualized on the aerodynamic panel grid

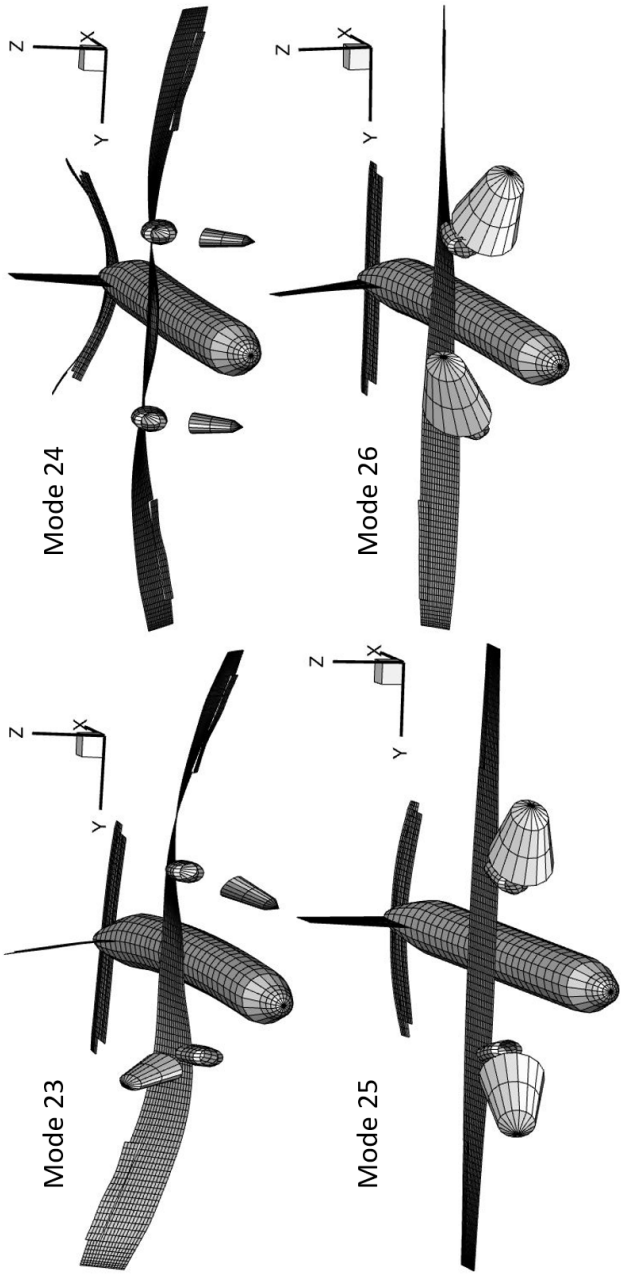

Figure A.3.: The elastic modes 23 - 26 of the full aircraft, visualized on the aerodynamic panel grid

A.3. Flutter results for flexible blades and quasi-steady aerodynamics

Fig. A.4 compares flutter results for the simplified pylon system with quasi-steady aerodynamics and flexible blades between Floquet and TM-analysis. The equivalent results with unsteady aerodynamics are shown in Fig. 4.5. In Fig. A.4, the frequency and dampings of the whirl and first-order cyclic propeller modes match exactly, verifying the TM-method. This indicates that the differences observed in Fig. 4.5 are caused by the omission of the aerodynamic states from the Floquet-analysis, not by the different analysis methods or problems in the TM-method.

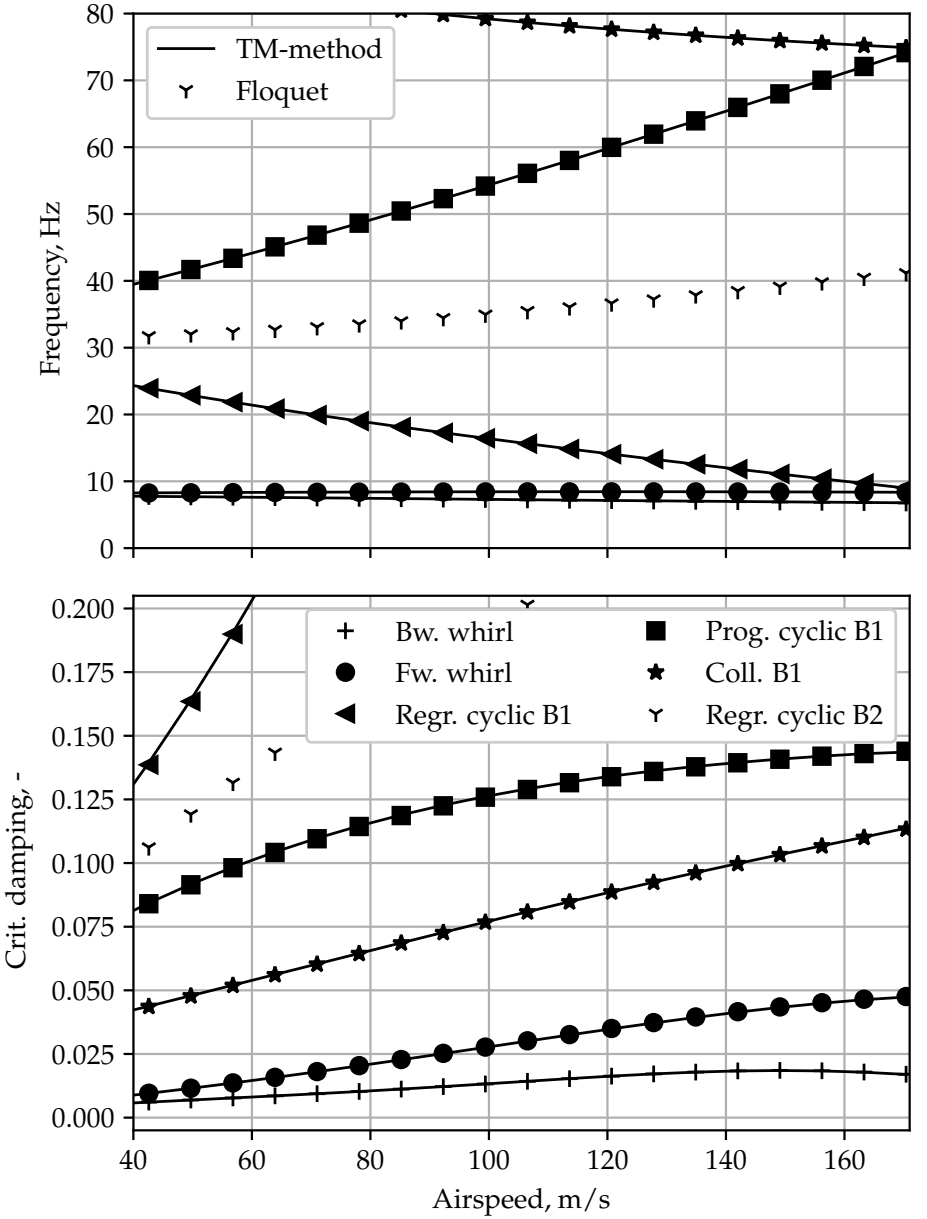

Figure A.4.: Comparison of flutter results for the simplified pylon system with elastic blades with quasi-steady aerodynamics

A.4. List of publications

This appendix comprises the list of publications of the author of this thesis (denoted "writer" in the following) at the time of writing. The content of the publications is summarized. In case of co-authorship, the contribution of the writer is explained. The publications that contain work reproduced in this thesis are marked with "*".

1. **Master thesis on the aeroelastic stability of the FVA30 motor glider**
   Master thesis of the writer and its dissemination in several conference papers. The first is the actual master thesis, the second the dissemination in a conference paper on a national scientific conference with the two supervisors of the thesis as co-authors. The second is an extension of the first paper published in the proceedings of an international conference (the presentation itself was canceled due to the COVID-19 pandemic). The last paper describes the aircraft configuration of the motor glider studied in the thesis.

   a) [102]: C. Koch. "Aeroelastische Untersuchung eines V-Leitwerks mit integrierten Antriebseinheiten". MA thesis. Aachen: RWTH Aachen University, Apr. 2019

   b) [103]: C. Koch, J. Arnold, and H. Schmidt. "Aeroelastische Untersuchung eines V-Leitwerks mit integrierten Antriebseinheiten". In: *Deutscher Luft- und Raumfahrtkongress 2019*. Darmstadt: Deutsche Gesellschaft fuer Luft und Raumfahrt (DGLR), Nov. 2019. DOI: 10.25967/490238

   c) [104]: C. Koch and J. Arnold. "Aeroelastic stability assessment of a V-Tail with integrated propulsion units". In: *Proceedings of the Second International Symposium on Flutter and its Applications*. Paris, May 2020

   d) [105]: T. Moxter, W. Enders, B. Kelm, M. Scholjegerdes, C. Koch, and P. Dahmann. "Untersuchung alternativer Antriebe von Kleinflugzeugen anhand des hybrid-elektrischen Motorseglers FVA 30". In: *Deutscher Luft- und Raumfahrtkongress 2020*. Aachen (virtuell): Deutsche Gesellschaft fuer Luft und Raumfahrt (DGLR), 2020

2. **Study on airframe modeling depth on whirl flutter stability**
   These publications comprise a parametric study on the modeling depth of the aeroelastic airframe model on its whirl flutter stability using the

Houbolt/Reed method. The first paper is a preliminary version presented at a national scientific conference, while the second is the final journal article version.

a) [106]: C. Koch. "Relevance of whirl flutter for electric aircraft configurations". In: *Deutscher Luft- und Raumfahrtkongress 2020*. Aachen (virtuell): Deutsche Gesellschaft fuer Luft und Raumfahrt (DGLR), Sept. 2020

b) [19]: C. Koch. "Parametric whirl flutter study using different modelling approaches". In: *CEAS Aeronautical Journal* 13 (Oct. 2021), pp. 57–67. DOI: 10.1007/s13272-021-00548-0

3. **Application of Houbolt/Reed-theory to High-Altitude platform**
A conference paper describing the aeroelastic design and analysis during the preliminary design of a high-altitude platform. The flutter analysis included some preliminary whirl flutter results obtained with the Houbolt/Reed method. The contribution of the writer was the aeroelastic stability analysis of the configuration.

a) [107]: A. Voß, C. Koch, S. Niemann, M. Mantei, V. Handojo, and C. Weiser. "Transition From Preliminary to Detailed Design of a Highly Elastic Solar Electric Aircraft". In: *Proceedings of the International Forum on Aeroelasticity and Structural Dynamics (IFASD) 2022*. Madrid, Spain, June 2022

4. **Transfer-Matrix method development***
This paper and presentation on an international conference describes the main theory of the method developed in this thesis and some example applications on a simplified propeller model.

a) [71]: C. Koch. "Whirl flutter stability assessment using rotor transfer matrices". In: *Proceedings of the International Forum on Aeroelasticity and Structural Dynamics (IFASD) 2022*. Madrid, Spain, June 2022

5. **Influence of blade elasticity on whirl flutter stability***
These papers are based on the master thesis of the second author and supervised by the writer. The first paper includes the results of the thesis, presented on an international conference. The second paper was extend with further analysis by the author and published as a journal article.

a) [73]: C. Koch and B. Koert. "Influence of blade elasticity on propeller whirl flutter stability". In: *AIAA SCITECH 2023 Forum*. National Harbor, MD & Online: American Institute of Aeronautics and Astronautics, Jan. 2023. DOI: 10.2514/6.2023-1307

b) [74]: C. Koch and B. Koert. "Including Blade Elasticity into Frequency-Domain Propeller Whirl Flutter Analysis". In: *Journal of Aircraft* (Oct. 2023). DOI: 10.2514/1.C037501

6. **Influence of blade aerodynamics***
This journal article comprises the results of a joint study of the writer together with the second author on the influence of aerodynamic modeling on the whirl flutter stability of a simplified pylon system. The second author contributed all aerodynamic calculations using DUST, while the writer post-processed the results and contributed the low-fidelity and UPM results. The other co-authors contributed to parts of the software used and revised the manuscript.

a) [75]: C. Koch, N. Böhnisch, H. Verdonck, O. Hach, and C. Braun. "Comparison of Unsteady Low- and Mid-Fidelity Propeller Aerodynamic Methods for Whirl Flutter Applications". In: *Applied Sciences* 14.2 (Jan. 2024). DOI: 10.3390/app14020850

7. **Studies on full-aircraft level***
The first paper is based on the master thesis of the first author, which was supervised by the writer. It describes the generic aircraft configuration and the extension of the studies from Koch and Koert [74] to this more complex airframe model. The other co-authors supported in supervising the thesis. The second paper by the writer extends the work of Koch, Böhnisch et al. [75] to the generic turboprop model.

a) [76]: J. Noël, C. Koch, B. Stickan, H. Bleecke, and J. Arnold. "Influence of blade elasticity on the whirl flutter stability of a propeller-driven aircraft". In: *Proceedings of the International Forum on Aeroelasticity and Structural Dynamics (IFASD) 2024*. unpublished. Den Haag, NL, June 2024

b) [77]: C. Koch. "Whirl flutter analysis using linearized propeller transfer matrices". In: *Proceedings of the International Forum on Aeroelasticity and Structural Dynamics (IFASD) 2024*. unpublished. Den Haag, NL, June 2024